

ABSTRACT

TJAYADI, LEONARDI. Innovative Approach to SCC Inspection and Evaluation of Canister in Dry Storage (Under the direction of Dr. K. L. Murty).

The spent nuclear fuels (SNFs) in the U.S. after removal from nuclear reactors and submersion in spent fuel pools are transported to Independent Spent Fuel Storage Installations (ISFSI) for storage in dry storage canisters usually made of austenitic stainless steels (SS) type 304, 304L, 316 or 316L for several decades. The dry storage canisters are then enclosed in a dry storage cask (DSC) equipped with a ventilation for natural cooling. Since the locations of the ISFSIs in the U.S. are generally near the ocean, the dry storage canisters can be exposed to ambient site conditions through the ventilation. The high level of chloride salts found in the ISFSI location can be deposited on the dry storage canister through the ventilation on the DSC leading to possible chloride-induced stress corrosion cracking (CISCC). Electric Power Research Institute (EPRI) conducted a study regarding the materials degradation mode in ISFSI and listed CISCC as the number one potential degradation mode for dry storage canisters. With the uncertainty of the projects on permanent storage facilities for the SNFs, dry storage facilities for the SNFs are in high demand and need to be given top priority. As the SNFs are stored in dry storage canisters for decades until a permanent storage facility is ready, the safety and long-term integrity of dry storage canisters are important. Understanding the SCC mechanism is key to the long-term integrity of the dry storage canisters and the mechanism can be investigated by performing crack growth experiments at different environmental conditions with fracture mechanics approach using a wedge opening loading (WOL) specimen and direct-current potential drop (DCPD) technique.

Prior to the crack growth experiments, calibration of the DCPD with crack length was established using a fatigue pre-cracked WOL specimen in air as well as in marine environments. This calibration chart was used later in the data analysis of the crack growth experiments.

Crack growth experiments were conducted using sensitized SS304H and sensitized SS304L at 22, 37 and 60 °C with substitute ocean water producing $0.975 \times 10^{-10} \pm 9.528 \times 10^{-12}$, $3.258 \times 10^{-10} \pm 9.551 \times 10^{-11}$ and $1.580 \times 10^{-9} \pm 2.593 \times 10^{-10}$ m/s for sensitized SS304H and $3.064 \times 10^{-11} \pm 4.009 \times 10^{-12}$, $1.945 \times 10^{-10} \pm 1.315 \times 10^{-11}$ and $8.830 \times 10^{-10} \pm 9.863 \times 10^{-11}$ m/s for sensitized SS304L. The obtained average crack growth rates as a function of temperature yielded activation energies of 60.9 ± 0.62 and 69.1 ± 8.96 kJ/mol for sensitized SS304H and sensitized SS304L, respectively which are associated with hydrogen diffusion in iron and steel. An experiment conducted with sensitized SS304L at 3x higher concentration produced an average crack growth rate of $1.985 \times 10^{-10} \pm 2.603 \times 10^{-11}$ m/s which is similar to that of sensitized SS304L at a regular concentration suggesting that increasing salt concentration does not significantly increase the average crack growth rate in sensitized SS304L. Further data analysis shows that crack initiation time is also primarily dependent upon temperature. Therefore, hydrogen embrittlement is considered to be responsible for stress corrosion cracking as the main driving force since it dictates the hydrogen transport to the crack tip for crack initiation and hydrogen propagation for crack growth. In addition, microstructural characterization post experiments indicated that cracks propagate intergranularly due to the chromium depletion along the grain boundaries by forming carbides ($M_{23}C_6$).

© Copyright 2020 by Leonardi Tjayadi

All Rights Reserved

Innovative Approach to SCC Inspection and Evaluation of Canister in Dry Storage

by
Leonardi Tjayadi

A dissertation submitted to the Graduate Faculty of
North Carolina State University
in partial fulfillment of the
requirements for the degree of
Doctor of Philosophy

Nuclear Engineering

Raleigh, North Carolina
2020

APPROVED BY:

Dr. K. L. Murty
Committee Chair

Dr. Mohamed Bourham

Dr. Jacob Eapen

Dr. Ronald Scattergood

DEDICATION

To the only savior Lord Jesus Christ, my beloved family, Prisca Tjahjadi and her family.

BIOGRAPHY

Leonardi Tjayadi was born in Jakarta, Indonesia. He moved to the United States of America to continue his post-secondary education after receiving his high-school diploma from Jakarta, Indonesia. He earned his bachelor's degree in December 2011 and master's degree in December 2012 from the University of Michigan in Nuclear Engineering and Radiological Sciences with Magna Cum Laude distinction. During his study at the University of Michigan, he was a recipient of University Honors designation and twice named to the Dean's Honor List. He performed research activities as an undergraduate student in cadmium zinc telluride (CZT) detectors, high-purity germanium (HPGe) radiation detectors and half-life measurement in the Neutron Science Laboratory at the University of Michigan. After receiving his master's degree, he was involved in a project funded by Department of Defense (DoD)/ Defense Threat Reduction Agency (DTRA) in manufacturing radiation detectors at the University of Michigan between 2013 - 2015 and joined an internship program with the department of reactor core design at a sister's company of Westinghouse Nuclear, Shanghai Nuclear Engineering Research and Design Institute (SNERDI) in Shanghai, China. He then continued his doctoral study in nuclear engineering at North Carolina State University in 2016 working on Innovative Approach to SCC Inspection and Evaluation of Canister in Dry Storage under the direction of Prof. K. L. Murty. In addition, he conducted nuclear materials research during an internship program at Oak Ridge National Laboratory in summer 2018 where he was featured in the internship participant spotlight.

ACKNOWLEDGMENTS

Gratitude and praise are first and foremost to Lord Jesus Christ who persistently advised me to continue my education, guided every step of the way from the start to completion of doctoral program through his unconditional love and power.

Special thanks to my PhD advisor, Prof. K. L. Murty for his trust in me in the project in the first place, unwavering support, persistent encouragement, experienced supervision and priceless advice throughout the project. In addition to the project, it was an honor and pleasure to have enrolled in his last ever Nuclear Materials course in fall 2016 where he added to the course materials his decades of expertise, knowledges and experiences in nuclear materials.

Tributes and regards are handed to the committee members; Prof. Ronald Scattergood, Prof. Mohamed Bourham and Prof. Jacob Eapen for their insightful inputs and discussions throughout the project. A special honor as well to have registered in Prof. Ronald Scattergood's last ever Mechanical Behavior of Materials course in Spring 2019 where he taught the material with an easily understandable explanation reflecting his expertise, knowledges and experiences in the field.

A distinctive recognition is passed to Dr. Nilesh Kumar who provided me with his knowledge, background and expertise at the beginning of the project that helped my transition to Prof. K. L. Murty's group smoother, guidance and discussions on the experiments and data analysis, work plans throughout the PhD program as well as aid in publications and presentations.

A particular tribute is dedicated to Prisca Tjahjadi, her family, Pastor Jo, Tante Hana, Mas Wit, Ci Sandra, Father Justin, Father Ed, Father Kane who flourished me with love, patience, advice and prayers throughout those difficult times when I was lost that I have returned to the correct path which has made this PhD journey possible and with encouragement to pursue my

education. A specific gratitude for my parents and brother who showered me with advice, support, love and motivation for this program. Please accept my apology that we could not spend time together as much as we wanted.

I would like to extend my appreciation to those who assisted me throughout along the way of this PhD journey; Dr. Harvey West, Ervin Miller, Dr. Stephen Liu, Dr. Scott Gordon, Chris Sanford, Emad Tawardrous, Dr. Charles Bryan, Prof. Zeev Shayer, Stefanie Keto, Mario Milev, Abdullah Alomari, Zeinab Alsmadi, Pratik Joshi, Micah Tillman, Daisuke Tezuka, Kevin Godeaux, Jamison Harris, Jonny Klemes, Dr. Zhang Guanheng and those whose names I forgot to mention.

TABLE OF CONTENTS

LIST OF TABLES	x
LIST OF FIGURES	xi
DISSERTATION OUTLINE.....	1
CHAPTER 1: INTRODUCTION.....	3
1.1. Fission reaction	3
1.2. Spent nuclear fuel	4
1.3. Project objectives	8
1.4. References.....	9
CHAPTER 2: LITERATURE REVIEW	11
2.1. Physical metallurgy of stainless steels.....	11
2.2. Stress corrosion cracking	15
2.3. SCC important factors.....	19
2.3.1. Microstructure/martensite	19
2.3.2. Sensitization.....	22
2.3.3. Composition.....	25
2.3.4. Stress	27
2.3.5. Environment.....	28
2.3.5.1. Temperature	28
2.3.5.2. Solution composition	29
2.3.5.3. pH.....	31
2.4. Mechanisms of SCC	33
2.4.1. Chromium depletion	33

2.4.2. Slip dissolution.....	34
2.4.3. Hydrogen embrittlement	36
2.4.4. Strain-induced martensite formation.....	38
2.5. Intergranular crack propagation.....	39
2.6. Fracture mechanics	40
2.7. References.....	44
CHAPTER 3: MATERIAL AND EXPERIMENTAL METHODS.....	62
3.1. Corrosion chamber.....	62
3.2. Wedge opening loading specimen	64
3.3. Instrumented bolt for loading WOL specimen	66
3.4. Fatigue pre-cracking	67
3.5. Direct-current potential drop technique	70
3.6. References.....	76
CHAPTER 4: RESULTS AND DISCUSSIONS	79
4.1. Microstructural characterization of as-received samples.....	79
4.2. Mechanical properties	80
4.3. Calibration chart.....	81
4.4. Crack growth experiments	82
4.4.1. Crack growth tests with non-sensitized SS304 specimens	82
4.4.2. Crack growth experiments with sensitized SS304H specimens in substitute ocean water.....	85
4.4.3. Crack growth experiments with sensitized SS304L specimens in substitute ocean water.....	92

4.4.4. Effect of temperature on crack growth of sensitized SS304 specimens in substitute ocean water	96
4.4.5. Effect of temperature on crack initiation in substitute ocean water.....	98
4.4.6. Crack growth experiments on sensitized SS304L in NaCl solution.....	100
4.4.7. Crack growth experiments on sensitized SS304H specimens in MgCl ₂ solution	102
4.4.8. Crack growth experiments with sensitized SS304H specimens in NaCl + HCl solution.....	104
4.5. Microstructural characterization following crack growth experiments	106
4.5.1. Microstructural characterization of non-sensitized SS304 specimens.....	106
4.5.2. Microstructural characterization of sensitized SS304H.....	107
4.5.3. Microstructural characterization of sensitized SS304L	112
4.5.4. Microstructural characterization of sensitized SS304L in 126 g/L NaCl.....	115
4.5.5. Microstructural characterization of sensitized SS304H in MgCl ₂ brine.....	116
4.5.6. Microstructural characterization of sensitized SS304H in NaCl + HCl solution.....	117
4.6. References	118
CHAPTER 5: CONCLUSIONS AND FUTURE WORK	122
5.1. Conclusions.....	122
5.2. Future work	126
ACKNOWLEDGMENTS	127
APPENDICES	128
Appendix A: Publications and presentations	129
Appendix B: Fracture Mechanics-Based Study of Stress Corrosion Cracking of SS304	

Dry Storage Canister for Spent Nuclear Fuel	130
Appendix C: Understanding stress corrosion cracking behavior of austenitic stainless steel SS304 for dry storage canisters in simulated sea-water	139

LIST OF TABLES

Table 2.1	Chemical Composition of Austenitic Stainless Steel 304, 304L and 316L in wt% [5,6].....	13
Table 3.1	Strainsert Calibration Chart.....	66
Table 4.1	Tensile test results of sensitized (at 600 °C for 215 hrs) SS304H/L with the errors indicated inside the brackets	80
Table 4.2	Chemical composition of the substitute ocean water [1]	83
Table 4.3	Load calculation versus K_I values for a specimen with two different crack lengths	84
Table 5.1	Summary of crack growth experiments.....	123
Table 5.2	Comparison of crack growth values from DCPD technique and optical microscopy from crack growth experiments.	124

LIST OF FIGURES

Figure 1.1. A representation of pressurized water reactor nuclear power plant [3]	4
Figure 1.2. Spent nuclear fuels submerged in spent fuel pools [5].....	5
Figure 1.3. A dry storage canister encapsulated in a dry storage cask [6].....	6
Figure 1.4. Vertical dry storage canister of spent nuclear fuels [6].....	6
Figure 1.5. Independent spent fuel storage installations locations throughout the U.S. [6].....	7
Figure 1.6. Potential degradation modes of dry storage canister [10].	7
Figure 2.1. Body-centered cubic crystal structure [4].	11
Figure 2.2. Face-centered cubic crystal structure [4].....	13
Figure 2.3. Stainless Steel Phase Diagram at 900 °C [3].	14
Figure 2.4. Schaffler constitution diagram for stainless steels [1,7,8].....	14
Figure 2.5. Necessary conditions for SCC to occur [14-16].....	16
Figure 2.6. Fracture toughness as a function of specimen thickness in plane stress and plane strain behavior [23].	18
Figure 2.7. Plane stress and plane strain condition [24].	19
Figure 2.8. Body-centered tetragonal crystal structure [25].	20
Figure 2.9. Hexagonal close packed (hcp) crystal structure [30].	21
Figure 2.10. Precipitation of chromium carbides at grain boundaries due to slow cooling [46].	24
Figure 2.11. The depleted zone of chromium below 12% [46].	24
Figure 2.12. Sensitization temperature range of austenitic stainless steels [46].....	24
Figure 2.13. Quench anneal heat treatment of austenitic stainless steels [46].....	25
Figure 2.14. A schematic depiction of crack growth rate with stress intensity factor [75].	28

Figure 2.15. A model of crack propagation as a function of temperature for IGSCC in 304 by ASM International [83].	29
Figure 2.16. Pourbaix diagram for iron [111].....	32
Figure 2.17. A schematic diagram of slip dissolution model consisting of film rupture, anodic dissolution and film repassivation [124].	35
Figure 2.18. A depiction of hydrogen embrittlement model for SCC mechanism [140].	37
Figure 2.19. Dislocation-obstacle interaction in hydrogen enhanced plasticity model [151].	38
Figure 2.20. Intergranular cracking in sensitized SS304.	40
Figure 2.21. Three modes of fracture [157].....	41
Figure 2.22. Plane stress and plane strain condition [24].	41
Figure 2.23. Fracture toughness as a function of specimen thickness in plane stress and plane strain behavior [23].	42
Figure 2.24. Outcomes from determining stress intensity factor in SCC environment [158].	43
Figure 3.1. (a) A CAD model showing the design of the corrosion chamber and (b) a photograph of the corrosion chamber built.	63
Figure 3.2. 2-D and 3-D drawing showing WOL specimen geometry and dimensions	64
Figure 3.3. Pin made of SS 304H for assisting in loading of WOL specimen using instrumented bolt.	65
Figure 3.4. (a) Different views of WOL samples prepared from SS 304-H alloy supplied by Colorado School of Mines, Golden, (b) Optical macrograph showing tip region of the WOL specimen, and (c) A magnified view of the notch tip depicting the shape of the tip for measuring the radius of the tip (radius = ~193 μm).....	65
Figure 3.5. A drawing of instrumented bolt designed by Strainsert company.	66

Figure 3.6. Instrumented bolt straight-line signal as a function of test load.....	67
Figure 3.7. (a) Dimensions of WOL specimen in inches and (b) a WOL specimen.	68
Figure 3.8. Fatigue pre-crack experimental setup.....	68
Figure 3.9. A fatigue pre-cracked WOL specimen.....	69
Figure 3.10. Optical microscope to measure the fatigue pre-crack length.	70
Figure 3.11. DCPD measurement in air for calibration chart.	72
Figure 3.12. DCPD experiment setup in marine environment for calibration chart.....	73
Figure 3.13. (a) Crack growth experimental setup and (b) WOL specimen submerged in marine environment.....	74
Figure 4.1. (a) Optical micrograph, (b) Elements identified from EDS and (c) Intensities of the identified elements through EDS of SS304H.....	79
Figure 4.2. (a) Optical micrograph, (b) Elements identified from EDS and (c) Intensities of the identified elements through EDS of SS304L.	80
Figure 4.3. Engineering stress-engineering strain curve of SS304H/L in rolling and transverse directions.....	81
Figure 4.4. Calibration curve of potential drop of WOL specimen as a function of fatigue pre-crack length in air (solid) and marine environments (open).....	81
Figure 4.5. (a) A non-sensitized SS304 specimen with a fatigue pre-crack length of 2,475 μm under load and (b) The deformed specimen after 1,000 lbf.....	82
Figure 4.6. (a) Non-sensitized SS304 specimen fatigue pre-cracked to 3,200 μm and (b) The plastically-deformed specimen after 1,000 lbf.....	83
Figure 4.7. (a) Bolt load variation with time, (b) Crack length versus time, (c) Stress intensity factor with time, (d) Crack growth versus time, (e) Stress intensity factor versus	

crack extension and (f) Crack growth rate with stress intensity factor for SS304H under substitute ocean water at 22 °C.	86
Figure 4.8. (a) Bolt load versus time, (b) crack length versus time, (c) stress intensity factor versus logarithmic time, (d) threshold stress intensity factor, (e) crack growth versus time, (f) stress intensity factor versus crack growth and (g) crack growth rate with stress intensity factor for SS304H under substitute ocean water at 37 °C.....	88
Figure 4.9. (a) Bolt load versus time, (b) Crack length versus time, (c) Stress intensity factor with time, (d) Crack growth versus time, (e) Stress intensity factor with crack extension and (f) Crack growth rate versus stress intensity factor for SS304H at 60 °C.....	91
Figure 4.10. (a) Bolt load versus time, (b) Crack length versus time, (c) Stress intensity factor with time, (d) Crack growth versus time, (e) Stress intensity factor with crack extension and (f) Crack growth rate versus stress intensity factor for SS304L at 21 °C.....	93
Figure 4.11. (a) Bolt load versus time, (b) Crack length versus time, (c) Stress intensity factor with time, (d) Crack growth versus time, (e) Stress intensity factor with crack extension and (f) Crack growth rate versus stress intensity factor for SS304L at 38 °C.....	94
Figure 4.12. (a) Bolt load versus time, (b) Crack length versus time, (c) Stress intensity factor with time, (d) Crack growth versus time and (e) Crack growth rate versus stress intensity factor for SS304L at 60 °C.	95
Figure 4.13. Arrhenius plot of crack growth rates for sensitized SS304H and sensitized	

SS304L	96
Figure 4.14. Comparison of average crack growth rates between the experimental values and those from Speidel at 22, 40 and 60 °C [3].....	98
Figure 4.15. (a) Crack initiation time versus temperature and (b) Arrhenius plot of crack initiation time for sensitized SS304H and sensitized SS304L under substitute ocean water.....	99
Figure 4.16. (a) Bolt load versus time, (b) Crack length versus time, (c) Stress intensity factor with time, (d) Crack growth versus time and (e) Crack growth rate versus time for SS304L in 126 g/L NaCl solution at 39 °C.....	101
Figure 4.17. (a) Bolt load versus time, (b) Crack length versus time, (c) Stress intensity factor with time, (d) Crack growth versus time and (e) Crack growth rate versus stress intensity factor for SS304H at 60 °C in MgCl ₂	103
Figure 4.18. (a) Bolt load versus time, (b) Crack length versus time, (c) Stress intensity factor with time, (d) Crack growth versus time and (e) Crack growth rate versus stress intensity factor for SS304H at 60 °C in NaCl + 3mL/L HCl solution.	105
Figure 4.19. A non-sensitized SS304 specimen with pitting corrosion after submersion in marine environment.....	106
Figure 4.20. (a) Cracked sensitized SS304H and branching at the crack tip and (b)-(e) intergranular crack propagation of sensitized SS304H after submersion in marine environment at 22 °C.....	108
Figure 4.21. (a) A WOL specimen of sensitized SS304H after nine weeks under substitute ocean water at 37 °C, (b) crack length measurement of 2775 μm under a metallurgical microscope and (c)-(f) intergranular crack propagation of	

sensitized SS304H after submersion in marine environment for nine weeks at 37 °C.....	110
Figure 4.22. (a) Conditions of sensitized SS304H WOL specimen after the experiment under substitute ocean water at 60 °C, (b) a total crack length of 1377 µm, (c) and (d) cracked open sensitized SS304H and branching of the crack and (e) and (f) intergranular crack propagation of sensitized SS304H after submersion in substitute ocean water at 60 °C.	111
Figure 4.23. (a) A measurement of total crack length of 1535 µm and (b) intergranular crack propagation of sensitized SS304L after submersion in substitute ocean water at 21 °C.....	112
Figure 4.24. (a) Condition of WOL specimen after the experiment, (b) crack growth measurement of 277 µm using optical microscopy and (c)-(f) intergranular crack propagation of sensitized SS304L after submersion in substitute ocean water at 38 °C.....	113
Figure 4.25. (a) Condition of sensitized SS304L WOL specimen after the experiment, (b) total crack length and (c) and (d) intergranular crack propagation of sensitized SS304L after submersion in substitute ocean water at 60 °C.....	114
Figure 4.26. (a) Condition of sensitized SS304L WOL specimen after the experiment, (b) crack growth of 444 µm using optical microscopy and (c) and (d) intergranular crack propagation of sensitized SS304L after submersion in 126 g/L NaCl solution at 39 °C.....	115
Figure 4.27. (a) A crack growth of 390 µm and (b)-(e) intergranular crack propagation of sensitized SS304H after submersion in MgCl ₂ solution at 60 °C.	116

Figure 4.28. (a) Condition of sensitized SS304H WOL specimen after the experiment and (b) total crack length using optical microscopy and (c)-(f) intergranular crack propagation of sensitized SS304H after submersion in 42 g/L NaCl + 3 mL/L HCl solution at 60 °C.	117
Figure 5.1. Crack growth rate versus inverse temperature for sensitized SS304H and sensitized SS304L under different environments.....	125
Figure 5.2. (a) Crack initiation time with temperature and (b) Arrhenius plot of crack initiation time for sensitized SS304H and sensitized SS304L under different environments.	125

DISSERTATION OUTLINE

This thesis consists of five chapters. Chapter 1 provides an introduction of spent nuclear fuels after being used inside a nuclear reactor for fission reactions, their removal to spent fuel pools and storing at dry storage facilities as there are currently no permanent storage facilities for spent nuclear fuels. Project objectives conclude this introductory chapter.

Chapter 2 consists of the literature review performed for the project starting with physical metallurgy of stainless steels, followed by stress corrosion cracking including its important factors (e.g microstructure, sensitization, composition, stress, environmental effects) and mechanisms. Intergranular crack propagation and fracture mechanics end this literature review chapter.

Chapter 3 describes the materials utilized for the crack growth experiments such as the chamber, specimen and bolt to apply stress to the specimen and the experimental methods employed for monitoring the crack growth and stress behavior throughout the experiment. Optical microscopy technique is also used to measure the length of the fatigue pre-crack before the crack growth experiments.

Chapter 4 starts with the microstructural characterization of as-received samples to detect the distribution of different elements in the alloy followed by tensile tests to determine the mechanical properties. Calibration chart is displayed to be used later during data analysis of crack growth experiments. Results from the crack growth experiments with different parameters are the main topic of this chapter. Outcomes from optical microscopy technique in assessing the accuracy of the technique employed for monitoring crack growth and the nature of crack propagation complete this chapter.

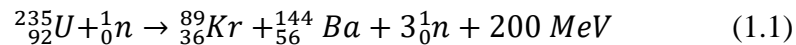
Chapter 5 presents the important points about SCC from the conducted experiments, summarizes the results of the crack growth experiments in tabular and graphical forms and suggests future work that can be conducted to give a better understanding of SCC.

This thesis is concluded with several appendices. Appendix A lists the publications and presentations during the author's PhD study. Appendix B shows a paper entitled "Fracture Mechanics-Based Study of Stress Corrosion Cracking of SS304 Dry Storage Canister for Spent Nuclear Fuel" published during TMS 2019 conference and Appendix C displays another paper "Understanding stress corrosion cracking behavior of austenitic stainless steel SS304 for dry storage canisters in simulated sea-water" published during TMS 2020.

CHAPTER 1: INTRODUCTION

1.1. Fission reaction

A typical nuclear reactor uses water to generate steam that converts thermal energy to mechanical and electrical energy. The heat required to increase the temperature of the water comes from the nuclear fuel that undergoes fission reactions to create energy. A material that can sustain fission reactions is a fissile material in reaction with a neutron and the only naturally occurring fissile isotope is ^{235}U which makes up 0.7 % of natural uranium [1]. The energy of a neutron is important for the capture event and thus, for the fission event. There is a greater probability for a capture event to occur if the neutrons have lower or thermal energies and are achieved through collisions by a moderator, for example water. The fissile isotope with high neutron fission cross sections will capture a thermal or slowed down neutron to become a metastable isotope and split into two more energetically stable isotopes as shown in Eq. 1.1 [1,2].



The occurred fission event produces a mass difference that is equivalent to a thermal energy of about 200 MeV per fission event. As the released neutrons will cause another fission event and produce more neutrons in the subsequent fission events, a fission chain reaction will occur in the reactor core and therefore, generates a lot of heat which is then transferred to a heat exchanger to generate steam. The steam that is now of high temperature and pressure will propel the turbines to produce electricity. A representation of a pressurized water reactor is displayed in Fig. 1.1 [3].

The Pressurized-Water Reactor (PWR)

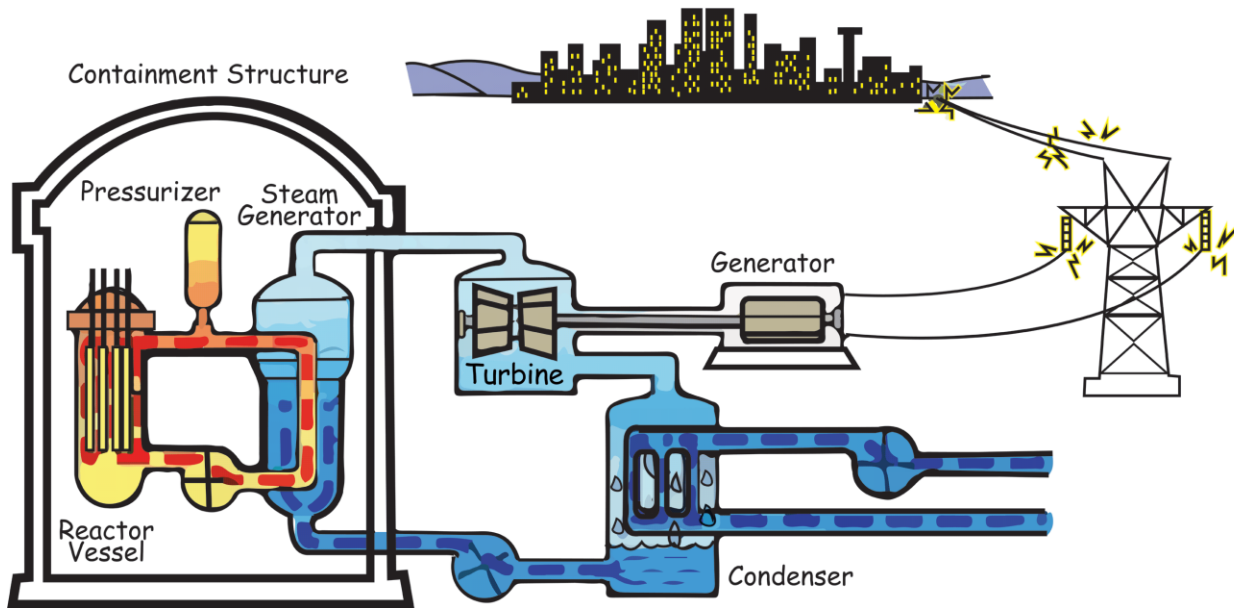


Figure 1.1. A representation of pressurized water reactor nuclear power plant [3].

1.2. Spent nuclear fuel

After being used in the reactor for 18 – 36 months, about a third of the nuclear fuels are removed from the reactor to be replaced with fresh fuels. The removed fuels will still emit radiation and heat, so they are stored in a spent fuel pool next to the reactor to reduce the radiation levels of the used nuclear fuels. The water in the spent fuel pool shields the radiation and absorbs the heat that is then removed by water circulation to external heat exchangers [4].

After submersion of at least five years in spent fuel pools (Fig. 1.2 [5]), the spent nuclear fuels (SNFs) in the U.S. are transferred to Independent Spent Fuel Storage Installations (ISFSI) for storage for more than several decades (with discussion currently underway to extend the life beyond 100 years) in horizontal and/or vertical dry storage canisters typically made of austenitic stainless steels (SS) type 304, 304L, 316 or 316L. As seen in Figs. 1.3 and 1.4, the dry storage

canisters are then encapsulated in a dry storage cask (DSC) equipped with air ventilation for cooling [6]. The spent fuel storage facilities in the U.S. as shown in Fig. 1.5 are usually located next to the ocean which then can cause the dry storage canisters to be exposed to ambient site conditions through the air ventilation [7]. National Atmospheric Deposition Program reported that the majority of ISFSI locations in the U.S. contain high levels of chloride salts [8]. The combination of the DSC equipped with air ventilation for natural cooling and the high level of chloride salts may cause the salts to be deposited on the dry storage canister leading to possible chloride-induced stress corrosion cracking (CISCC) [9]. In fact, in a recent study regarding the degradation mode of materials used in ISFSI, Electric Power Research Institute (EPRI) recommended several potential degradation mechanisms and CISCC topped the list as displayed in Fig. 1.6 [10]. Recent canister inspections have shown that chloride salts were present on the surface of the in-service canisters in near-marine settings which can cause canister penetration and radioactive gas releases that pose a threat to fuel rod integrity [11-13].

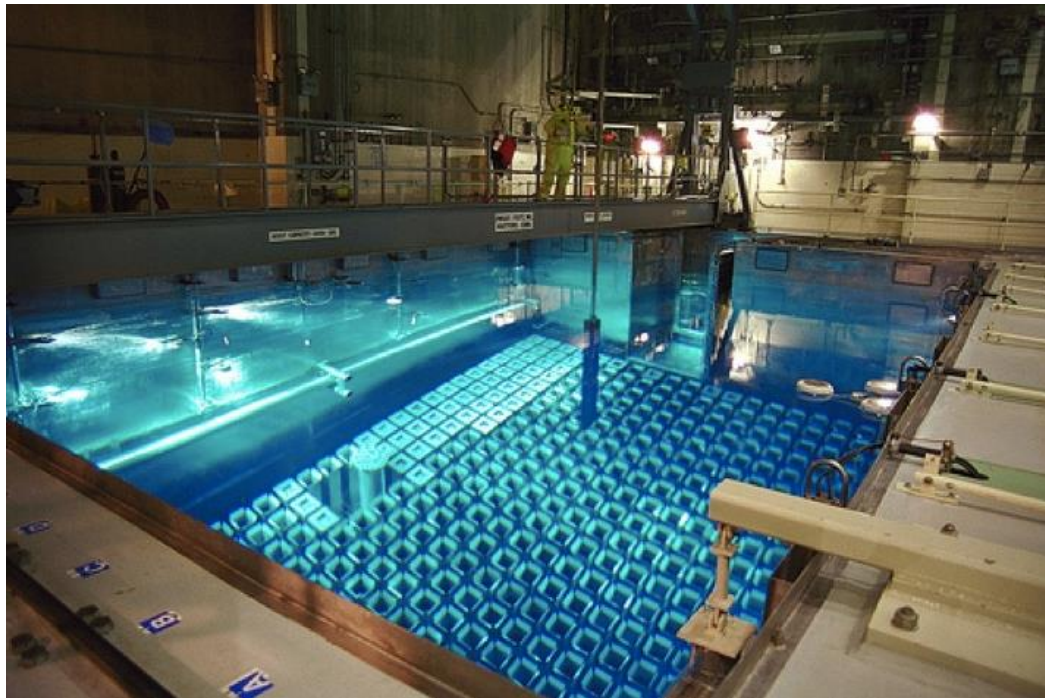


Figure 1.2. Spent nuclear fuels submerged in spent fuel pools [5].

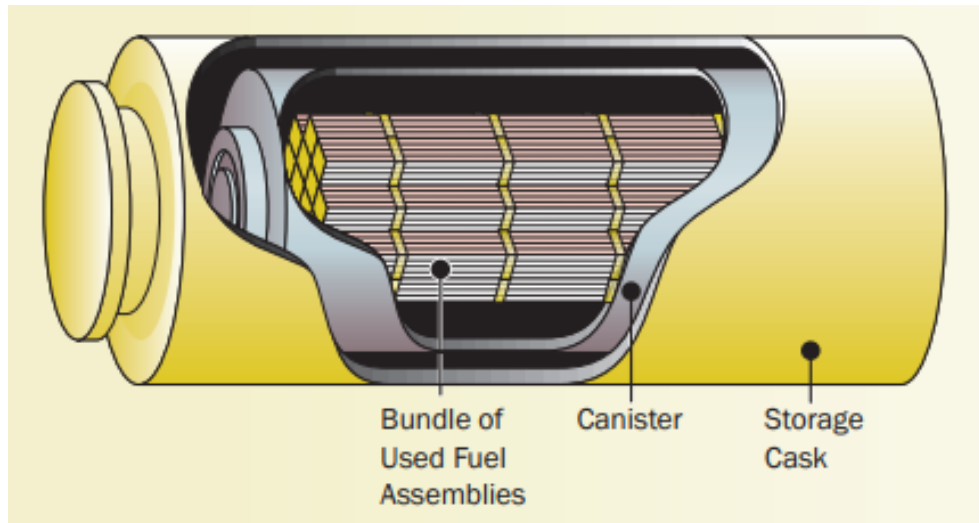


Figure 1.3. A dry storage canister encapsulated in a dry storage cask [6].

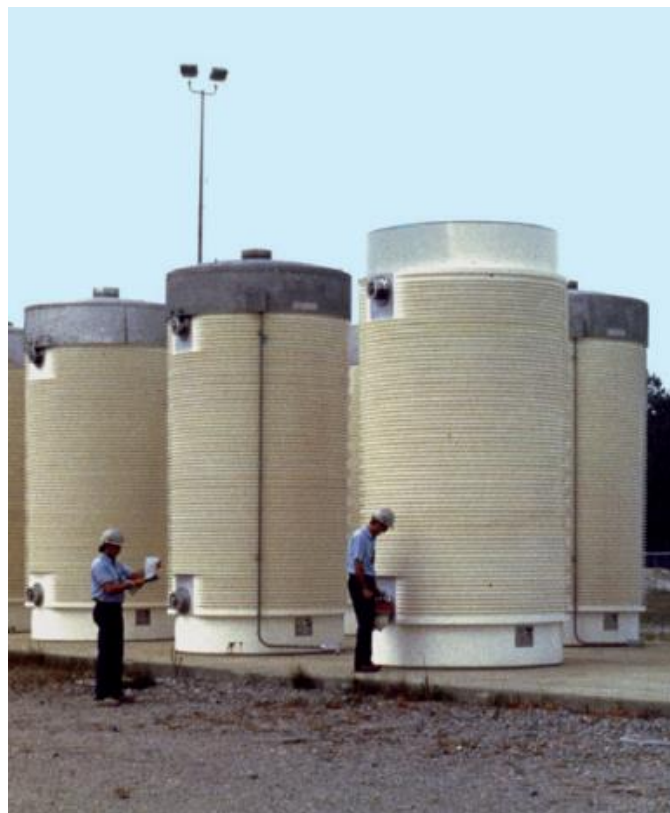


Figure 1.4. Vertical dry storage canister of spent nuclear fuels [6].

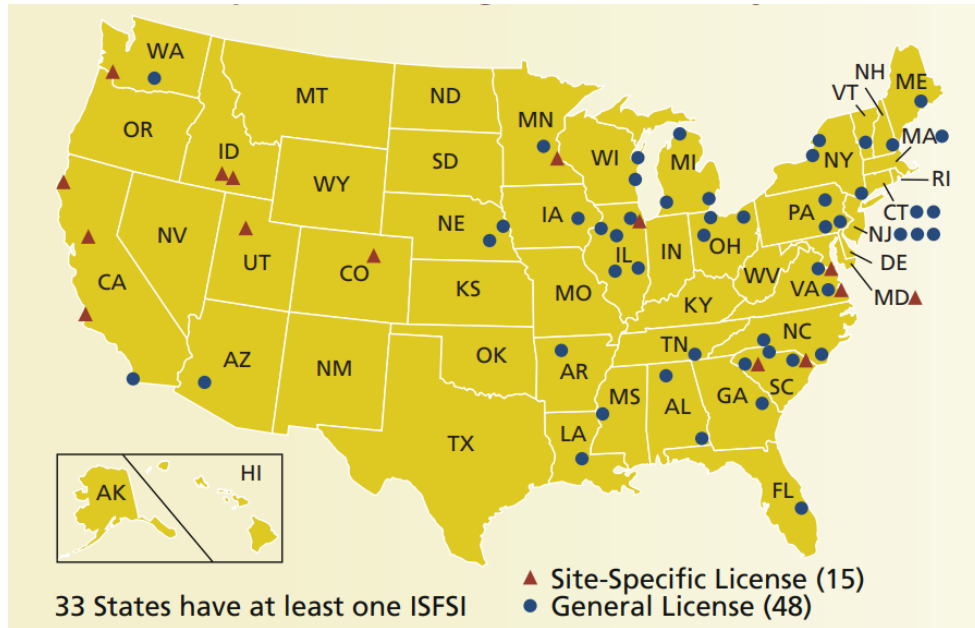


Figure 1.5. Independent spent fuel storage installations locations throughout the U.S. [6].

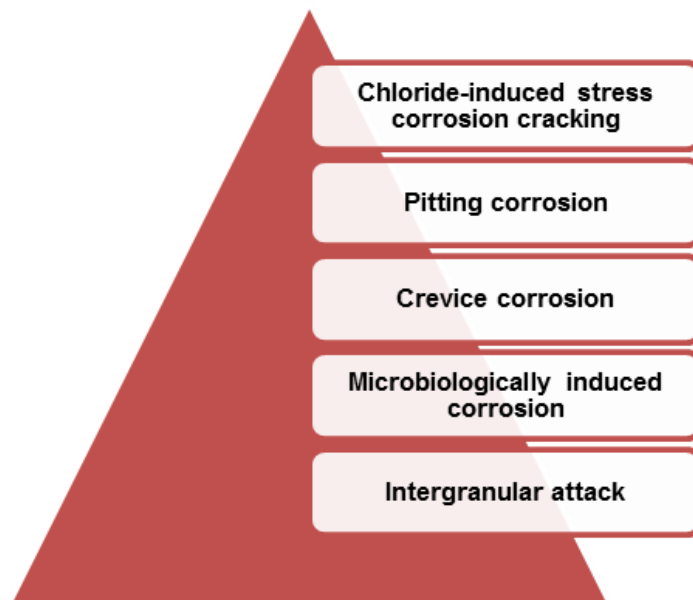


Figure 1.6. Potential degradation modes of dry storage canister [10].

With the uncertainty of Yucca Mountain Nuclear Waste Repository [14] and nuclear waste reprocessing facility projects for non-proliferation issues, there is currently no permanent storage facilities for the SNF. With a total commercial SNF of 60,000 metric tons as of the end of 2009 (78 % in the spent fuel pools and 22 % already in DSCs) and an increasing number of SNFs

annually (2,000 to 2,400 metric tons) [15], there exists a high need of dry storage facilities for storing SNFs [16]. The DSCs will then have to remain in the dry storage facilities for many decades [17] putting the robustness, safety and long-term integrity of the DSCs of utmost importance.

1.3. Project objectives

The objective of this project is to investigate the potential degradation mechanism(s) of austenitic SS canisters used in dry storage systems for SNF by [18]:

1. Investigating SCC of SS with emphasis on fracture mechanics using wedge opening loading (WOL) specimens.
2. Performing crack growth experiments using direct-current potential drop (DCPD) technique at various environmental conditions.
3. Identifying and understanding environmental conditions and metallurgical factors conducive to SCC such as salt concentrations, temperature, pH and stresses.

The obtained results from the project will be used to predict and monitor canister corrosion process (CISCC) that will provide possible solutions for aging management of dry storage facilities.

1.4. References

- [1] S. A. Glasstone Samuel, Nuclear Reactor Engineering, Chapman & Hall, New Delhi, India, 1998.
- [2] J. R. Lamarsh, A. J. Baratta, Introduction to Nuclear Engineering, 3rd ed, Pearson Education, New Jersey, USA, 2001.
- [3] U. S. NRC, Animated Images of Plants PWR and BWR. <https://www.nrc.gov/reading-rm/basic-ref/students/multimedia/animated-images-plants-pwr-bwr.html>, 2017 (accessed August 29, 2019).
- [4] World Nuclear Association, The Nuclear Fuel Cycle. <https://www.world-nuclear.org/information-library/nuclear-fuel-cycle/introduction/nuclear-fuel-cycle-overview.aspx>, 2017 (Accessed August 29, 2019).
- [5] R. Adams, Spent Fuel Pool Fire Risk Goes to Zero A Few Months After Reactor Shutdown, ANS Nuclear Café, ANS, 2014.
- [6] U.S. NRC, Information Digest, NUREG-1350, Vol. 23, Washington D.C., USA, 2011.
- [7] G. Oberson, D. Dunn, T. Mintz, X. He, R. Pabalan, L. Miller, US NRC-Sponsored Research on Stress Corrosion Cracking Susceptibility of Dry Storage Canister Materials in Marine Environments, WM2013 Conference, Phoenix, AZ, February 24-28, 2013, Paper Number 13344, 2013.
- [8] National Atmospheric Deposition Program/National Trends Network. <http://nadp.sws.uiuc.edu> (accessed August 29, 2019).
- [9] A. Sjong, L. Edelstein, Marine Atmospheric SCC of Unsensitized Stainless Steel Rock Climbing Protection, J.Fail. Anal. and Preven. 8 (2008) 410-418. <https://doi.org/10.1007/s11668-008-9158-1>.

- [10] EPRI, Modes and Effects Analysis (FMEA) of Welded Stainless Steel Canisters for Dry Cask Storage Systems. EPRI, Palo Alto, CA, 3002000815, 2013.
- [11] EPRI, Calvert Cliffs Stainless Steel Dry Storage Canister Inspection, EPRI, Palo Alto, CA. 460, 2014.
- [12] EPRI, EPRI Flaw Growth and Flaw Tolerance Assessment for Dry Cask Storage Canisters, Presentation to the NRC, August 5, 2014.
- [13] C. Bryan, D. Enos, Analysis of Dust Samples Collected from Spent Nuclear Fuel Interim Storage Containers at Hope Creek, Delaware, and Diablo Canyon, California, SAND2014-16383, Sandia National Laboratories, Albuquerque, NM. (2014) 281.
- [14] NEI, Used Nuclear Fuel. <https://www.nei.org/advocacy/make-regulations-smarter/used-nuclear-fuel>, 2019 (accessed September 22, 2016).
- [15] U. S. NRC, Spent Fuel Storage in Pools and Dry Casks. <https://www.nrc.gov/waste/spent-fuel-storage/faqs.html#1http://www.nrc.gov/images/waste/spent-fuel-storage/generation-storage.gif>, 2019 (accessed September 22, 2016).
- [16] P. McConnell, B. Hanson, M. Lee, K. Sorenson, Extended dry storage of used nuclear fuel: Technical issues: a USA perspective, Nucl. Eng. Technol. 43 (2011) 405-412. <https://doi.org/10.5516/NET.2011.43.5.405>.
- [17] T. Saegusa, G. Yagawa, M. Aritomi, Topics of research and development on concrete cask storage of spent nuclear fuel, Nucl. Eng. Des. 238 (2008) 1168-1174. <https://doi.org/10.1016/j.nucengdes.2007.03.031>.
- [18] Innovative Approach to SCC Inspection and Evaluation of Canister in Dry Storage, In Response to Call for Proposal CFDA Number 81.121, DE-FOA-0001129, IRP-15-9318: Canister Corrosion Evaluation, FY15, Colorado School of Mines, Lead.

CHAPTER 2: LITERATURE REVIEW

2.1. Physical metallurgy of stainless steels

The presence of chromium (Cr) in steels causes the formation of a protective passive layer that makes them neither to discolor in a normal atmospheric condition nor to stain and hence, they are called stainless steels. Beddoes and Parr mention that a minimum chromium content of 11% is required to maintain the passivity of stainless steels in normal atmospheric conditions. The main classifications of stainless steels are ferritic stainless steels, martensitic stainless steels, austenitic stainless steels, precipitation hardening stainless steels and duplex stainless steels [1,2].

Ferritic stainless steels (α) receive their name due to the similarity of its crystal structure to that of iron (Fe) at room temperature that is body-centered cubic (bcc) as illustrated in Fig. 2.1. They exhibit magnetic behavior when heated to 750 °C and the corrosion resistance in ferritic stainless steels comes from its chromium content of at least 11.5 %. Chromium also serves as a ferrite stabilizer that preserves the alloy in BCC crystal structure [2,3]. The most popular type of first-generation ferritic stainless steels is SS430 that contains 16-18 % Cr and 0.12 % carbon (C). The second generation of ferritic stainless steels have low carbon and nitrogen (N) content with SS409 being the most popular of second generation that contains titanium (Ti) as a carbide stabilizer. Meanwhile, superferritic stainless steels are the third-generation stainless steels recognized for the high chromium content between 18-30 % [1].

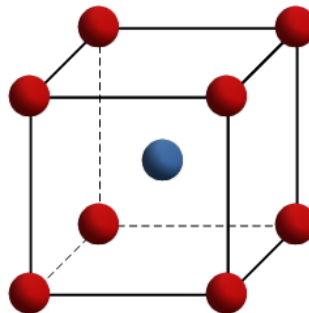


Figure 2.1. Body-centered cubic crystal structure [4].

While the ferritic stainless steels keep the carbon content low, martensitic stainless steels must have a high carbon content to achieve the desired hardness value. In fact, in martensitic stainless steels, the hardness comes primarily from carbon whereas the other existing elements enhance the hardening capacity or hardenability. Martensitic stainless steels have several classes. The low-carbon martensitic stainless steels with SS410 being the most popular contains 11.5-13.5 % Cr and 0.15 % C. The nickel (Ni) in Ni-containing low-carbon martensitic stainless steels enhances toughness and corrosion resistance in chlorides (Cl) and oxidizing acids. Meanwhile, SS440 is the most popular type of high-C martensitic stainless steels with different carbon content (0.6-0.75 %, 0.75-0.95 % and 0.95-1.20 %) and it also contains molybdenum (Mo). The last type of martensitic stainless steels is cutlery stainless steels with 12-14 % Cr and 0.15 % C found in SS420 [1-3].

Austenitic stainless steels (γ) exhibit nonmagnetic behavior and have a face-centered cubic (fcc) crystal structure as shown in Fig. 2.2. The presence of Ni retains the shape of austenitic stainless steels at room temperature and improves corrosion resistance. Chromium in the form of a thin chromium-rich (Cr_2O_3) passive surface layer also increases the corrosion resistance of austenitic stainless steels [1-3]. The high toughness, corrosion and oxidation resistance and easy fabrication make SS304 the most popular type of austenitic stainless steels. Since SS304 contains 18 % Cr and 8 % Ni, austenitic stainless steels are also called 18-8. Table 2.1 lists the chemical composition of SS304, 304L and 316L [5,6]. SS316 is recognized for its greater Mo content (2-4 %) compared to SS304 that improves high-temperature strength and corrosion resistance especially in chloride solutions. Although SS304 is popular due to its features, it is highly susceptible to CISCC [1]. Figure 2.3 shows the ternary phase diagram for stainless steel [3] and the chromium- and nickel-equivalent content of ferritic, martensitic and austenitic stainless steels

can be found in the Schaeffler diagram in Fig. 2.4 [1,7,8]. The Schaeffler diagram plots the composition of ferrite, martensite and austenite at room temperature as a function of the nickel and chromium equivalents to indicate the effects of addition of other elements in the basic structure of stainless steels. The three phases of ferrite, martensite and austenite can be achieved when the desired amount of nickel and chromium equivalents is met [3]. The nickel- and chromium-equivalent can be expressed by [1]

$$Ni_{eq} = Ni + 30 \times C + 0.5 \times Mn \quad (2.1)$$

$$Cr_{eq} = Cr + Mo + 1.5 \times Si + 0.5 \times Nb \quad (2.2)$$

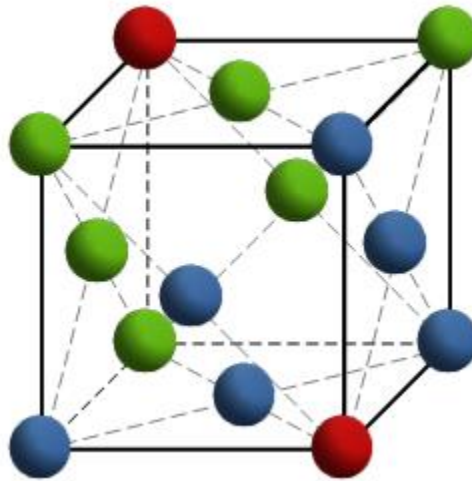


Figure 2.2. Face-centered cubic crystal structure [4].

Table 2.1. Chemical Composition of Austenitic Stainless Steels (304, 304L and 316L) in wt% [5,6].

Material	Fe	Cr	Ni	Mo	Mn	C	S	P	N	Si	Cu
SS304	Bal	18.19	8.07	0.1	1.21	0.039	0.002	0.026	0.042	0.55	N/A
SS304L	Bal	18.14	8.07	0.18	1.29	0.025	0.001	0.025	0.032	0.34	0.27
SS316L	Bal	16.43	10.13	2.06	1.35	0.019	0.0006	0.027	0.022	0.51	0.32

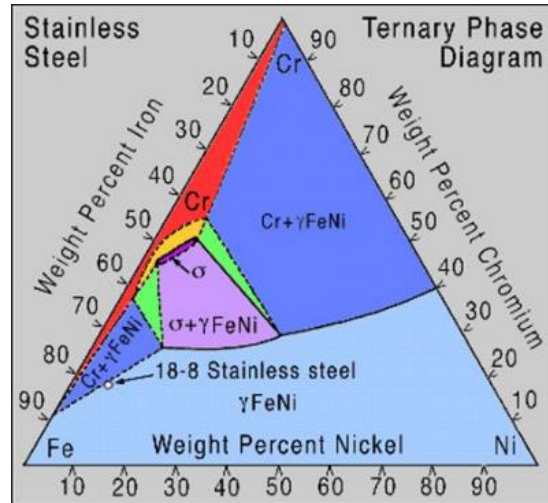


Figure 2.3. Stainless Steel Phase Diagram at 900 °C [3].

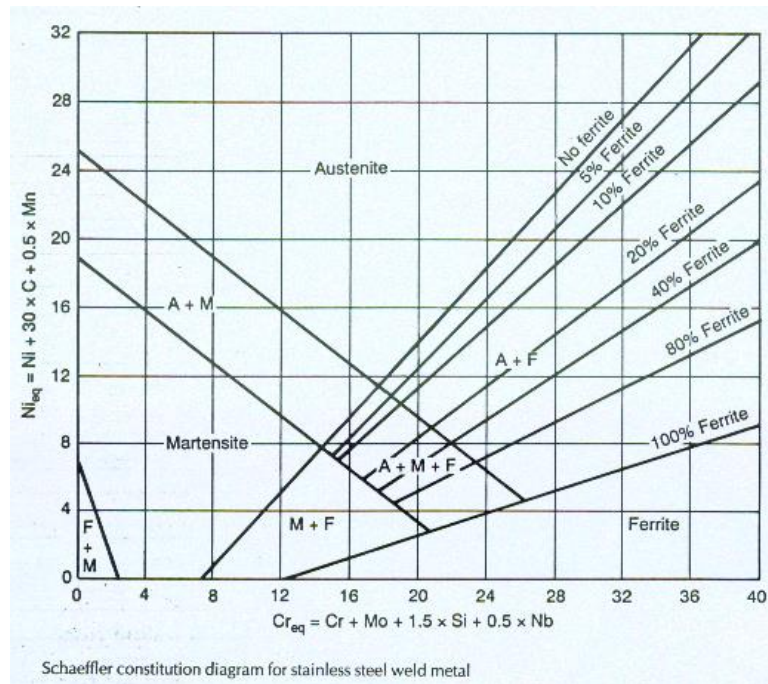


Figure 2.4. Schaeffler constitution diagram for stainless steels [1,7,8].

Precipitation hardening steels comprise of Cr > 16 %, Ni > 7 % and aluminum (Al) of about 1%. The Cr and Ni are to provide an optimum combination of good strength through martensitic steels properties and good corrosion resistance from the austenitic steels properties whereas the inclusion of Al is to form Ni-Al precipitates. They possess austenitic crystal structure in the

annealed condition and martensitic structure following cold deformation. Between 450 – 600 °C, they undergo age hardening where a single, low-temperature heat treatment is applied after machining without distortion to improve the strength. The commonly encountered precipitation hardening steel is 17-4 PH or SS630 which contains 17% Cr, 4 % Ni, 4 % copper (Cu) and 0.3 % niobium (Nb) [9].

Duplex stainless steels (DSS) are steels whose grade is between that of ferritic and austenitic stainless steels. They possess better toughness than ferritic steels and better corrosion resistance and strength than austenitic stainless steels. Molybdenum is included to improve the pitting and crevice corrosion resistance. The amount of ferrite and austenite depends on temperature, and ferritic structure is more pronounced at high temperatures. The DSSs have higher yield strength compared to austenitic stainless steels, better strength than ferritic and austenitic stainless steels in the annealed condition and cannot be hardened via heat treatment. The standard 22 % Cr type is the most popular type of DSS with a composition of 22 % Cr, 5 % Ni, 3 % Mo and 0.17 % N that provides better corrosion resistance than SS316 [2,3,10-13].

2.2. Stress corrosion cracking

The chloride salts from the atmospheric seacoast deposited on the dry canister through the ventilation of DSC can lead to possible CISCC where SCC is defined as the cracking of a material under static load by a combination of tensile stress, corrosive environment and material susceptibility as depicted by the diagram shown in Fig. 2.5 [14-16]. The susceptible material in this project is austenitic stainless steel 304 with variables of composition, heat treatment and microstructure, the corrosive environment is the atmospheric seacoast with high concentration of chloride salts with variables of temperature and pH whereas the tensile stresses required to induce

SCC originate from fabrication or welding residual stresses of SS304 [5]. All these three factors must be present for SCC to occur; if any of these three factors does not exist, SCC will not occur.

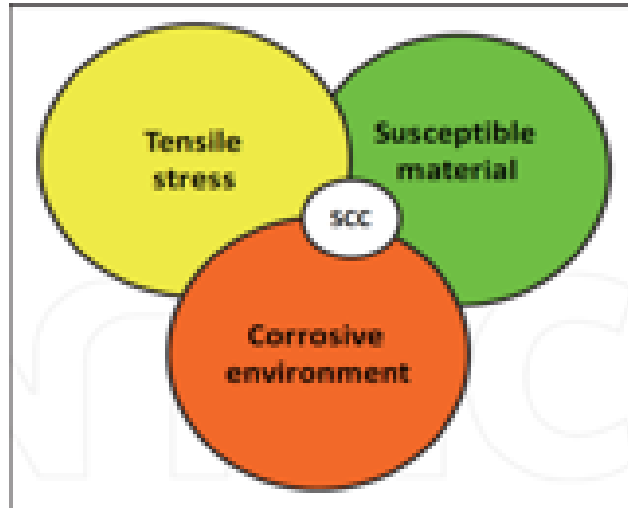


Figure 2.5. Necessary conditions for SCC to occur [14-16].

Cracking starts with crack initiation that serves to form a defect that will later result in a crack where the defect can derive from machining or scratches. An appropriate local environmental condition must be met for crack initiation to occur which is a vital stage for active-passive materials for example austenitic stainless steels as the local environmental condition at the crack tip is different from the bulk environmental condition. Crack initiation can be determined using crack initiation time and threshold stress intensity factor, K_{ISCC} , where pre-existing cracks or fatigue pre-cracks exist [17].

Crack propagation then follows crack initiation with environment and stress being the important factors in this stage. Several proposed rate-controlling processes in crack propagation are (a) surface reactions at the crack tip through oxidation, water reduction and hydrogen adsorption, (b) mass transportation along the crack in liquid phase through chemical diffusion and

(c) local modification at the crack tip from hydrogen diffusion and plastic strain as a result of stress concentration [18]. Crack growth can be determined using for example optical means where the crack growth rate can then be obtained. Microstructural characterizations then give information about the nature of the crack propagation of SCC. SCC causes a material to lose its strength considerably which then leads to brittle failure with no preliminary signs and thus, ends in catastrophic failure.

A lot of factors contribute to SCC which makes it a complicated phenomenon to understand despite SCC has occurred for many decades. All these contributing factors must be included if one tries to quantify this phenomenon in a mathematical expression, such as the one shown in the following expression [19-21]

$$\frac{dx_{\text{crack}}}{dt} = \dot{x}_{\text{crack}} = \alpha_{\text{crack}} f(T) f(K) f(R_a) f([\text{Cl}^-]) f(m_{\text{Cl}}) f(\text{pH}) f(\sigma_{\text{ys}}) \quad (2.3)$$

where the crack growth rate (\dot{x}_{crack}) is dependent upon the crack growth rate at a fixed reference set of conditions (α_{crack}), temperature (T), stress intensity factor (K), degree of sensitization (R_a), chloride concentration (Cl^-), chloride mass per unit area (m_{Cl}), pH of solution and yield stress (σ_{ys}). Another version from Sandia National Laboratory has considered the effects of stress intensity factor and temperature by using the power-law dependence and Arrhenius relationship, respectively [21]

$$\frac{dx_{\text{crack}}}{dt} = \alpha_{\text{crack}} \cdot \exp\left[-\frac{Q}{R}\left(\frac{1}{T} - \frac{1}{T_{\text{ref}}}\right)\right] \cdot (K - K_{\text{th}})^{\beta_{\text{crack}}} \quad (2.4)$$

where Q is the activation energy for crack growth, R is the universal gas constant ($8.314 \text{ J mol}^{-1} \text{ K}^{-1}$ or $1.987 \text{ cal mol}^{-1} \text{ K}^{-1}$), T is the absolute temperature in K , $T_{\text{ref}} = 60 \text{ }^\circ\text{F} = 15.6 \text{ }^\circ\text{C}$, K_{th} is the threshold stress intensity factor for SCC and β_{crack} is the stress intensity factor exponent. Evidently, the use of mathematical model of crack-growth expressed by Eq. (2.4) would require, among many parameters, knowledge of threshold stress intensity factor. In non-corrosive media, K_{th} corresponds to plane strain fracture toughness denoted by K_{IC} when the specimen thickness, $B > 2.5 \left(\frac{K_{\text{IC}}}{\sigma_y} \right)^2$ as shown in Figs. 2.6 and 2.7 whereas in corrosive media, K_{th} becomes K_{ISCC} , the stress intensity factor in SCC environment [21,22]. Thus, K_{ISCC} is one of the important parameters to be evaluated in the project along with the crack growth rate, \dot{x}_{crack} .

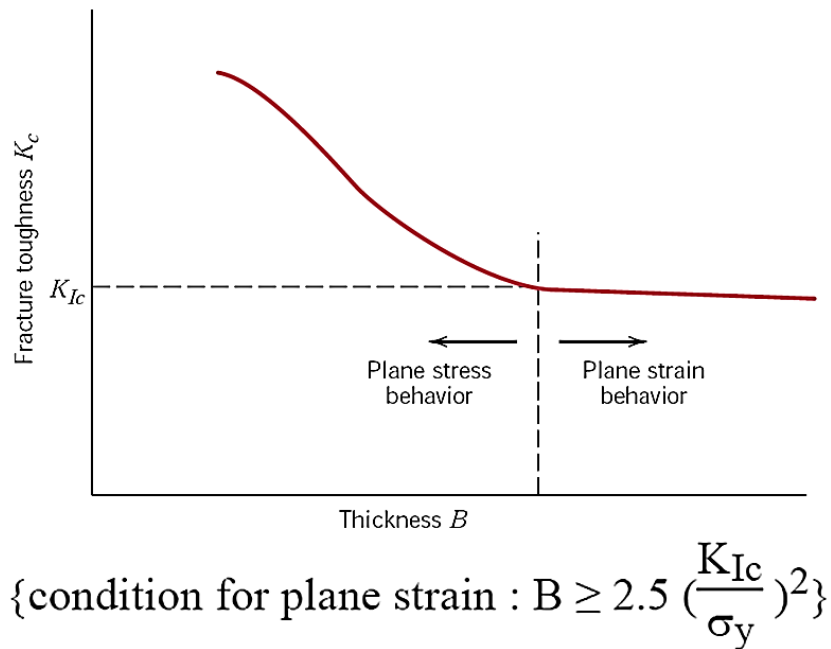


Figure 2.6. Fracture toughness as a function of specimen thickness in plane stress and plane strain behavior [23].

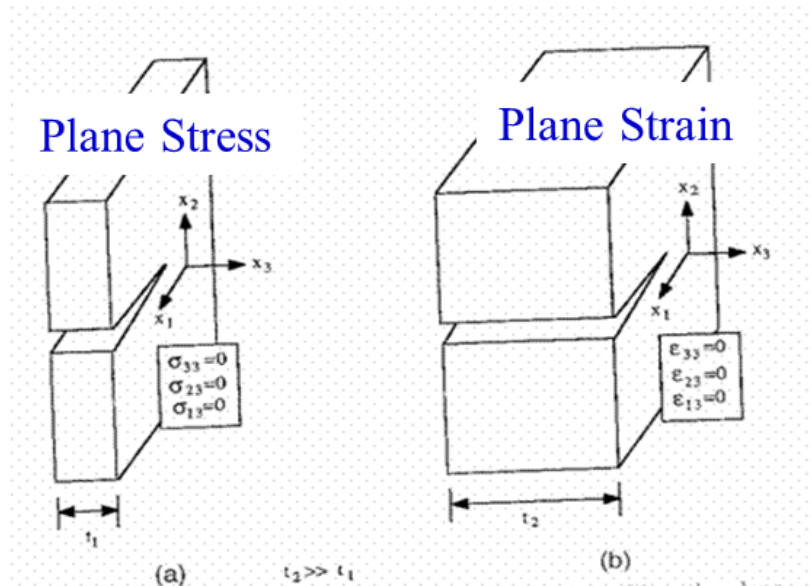


Figure 2.7. Plane stress and plane strain condition [24].

2.3. SCC important factors

2.3.1. Microstructure/martensite

Microstructure plays an important role in austenitic stainless steel corrosion behavior since microstructures susceptible to SCC such as intergranular cracking and other phases can be developed from thermomechanical processes that may affect the material performance. One of those is martensitic transformation.

The austenitic structure of the basic stainless steels 304 is metastable which can alter to a body-centered tetragonal (bct) (shown in Fig. 2.8 [25]) martensitic phase. The temperature at which austenitic stainless steels 304 transform to martensite start at around the freezing temperature of water. ASM International quantifies this temperature in terms of elemental composition as [3]

$$M_s(^{\circ}F) = 75 (75 (14.6 - Cr) + 110 (8.9 - Ni) + 60(1.33 - Mn) + 5(0.47 - Si) + 3000(0.068 - (C + N))) \quad (2.5)$$

which suggests an inverse relationship between the carbon content and the temperature raise; the higher the carbon content, the lower the temperature raise and vice versa. Martensite can also be formed in austenitic stainless steels through deformation-induced transformation at a higher temperature compared to M_s where the temperature at which 50% of volume is transformed into martensite via a plastic deformation of 30% is defined as [3]

$$M_{D30}(^{\circ}C) = 413 - 462(C + N) - 9.2 Si - Mn - 13.7 Cr - 9.5 Ni - 18.5 Mo \quad (2.6)$$

Equations 2.5 and 2.6 indicate that the martensitic transformation in austenitic stainless steels is more pronounced in 304L due to its lower carbon content as compared to 304H.

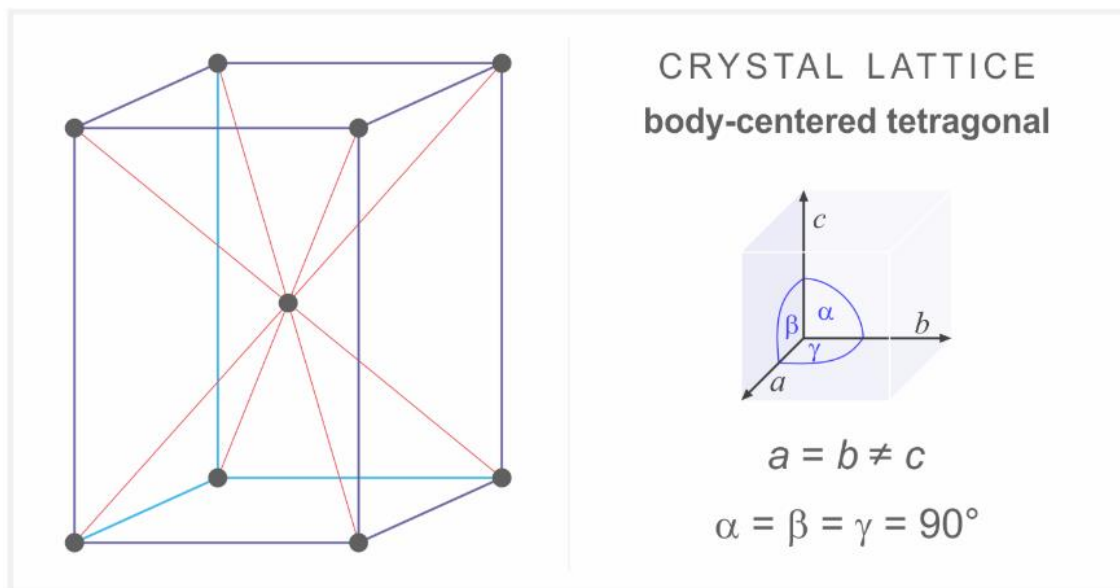


Figure 2.8. Body-centered tetragonal crystal structure [25].

Following transformation, two different types of martensite are formed, α' martensite and ϵ martensite. α' martensite has a bct crystal structure and consists of four types; lath, plate, surface and massive [26]. Lath martensite is found in low carbon stainless steels with 10-16 % Cr [27] with a habit plane of $\{2\ 2\ 5\}$ [28] whereas plate martensite has a high carbon content with $<7\%$ Cr and 22-35 % Ni. Nutting suggested that the surface and massive α' martensite are derivatives of lath martensite [29]. On the other hand, ϵ martensite has a hexagonal close-packed (hcp) crystal structure illustrated in Fig. 2.9 [30]. As the formation of ϵ martensite is inversely related to the stacking fault energy, it is also well known as faulted austenite with pure shear in $(1\ 1\ 1)$ plane [31]. In materials with low stacking fault energy, the deformation process is followed by the formation of deformation-induced martensite, ϵ martensite then α' martensite [32,33].

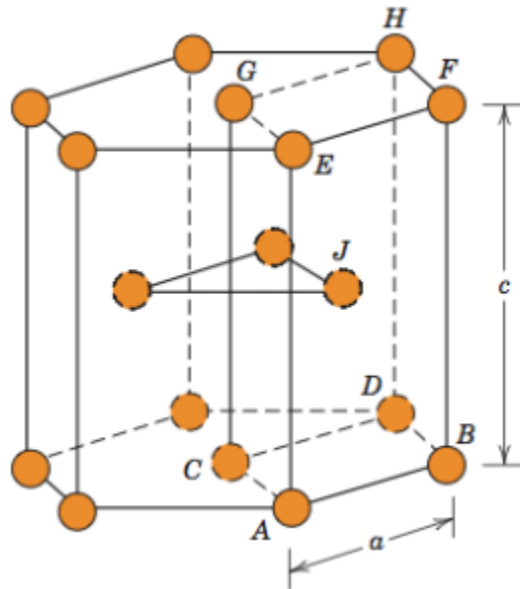


Figure 2.9. Hexagonal close packed (hcp) crystal structure [30].

Strain-induced martensite transformation has been related to pitting corrosion as studied by Peguet et al. who not only established a relation between martensite volume and pitting

initiation, but also a relation between dislocation pile-up and pitting as well as the relation of low stacking fault energy in stabilizing the dislocation pile-ups [34]. They also found the effect of different plastic strain on maximum pitting where they postulated an inverse relation between plastic strain and re-passivity [35]. The relation between pitting and strain was also investigated by Lu et al. where they found a maximum pitting of less than 10% and a saturation level of martensite above 10% where no considerable pitting was observed [36].

Some investigators suggested that plastic deformation causes austenitic stainless steels to transform into martensite [37,38]. As an hcp ϵ martensite usually precedes the α' martensite, the stacking fault is similar to a thin hcp region which causes the formation of an ϵ martensite linked to twinning [6]. The α' martensite transformation occurs at slip bands interactions where ϵ martensite is formed indicating that α' martensite is developed on a site that previously formed ϵ martensite [39]. Various suggestions have been made for α' martensite; Butler and Burke mentioned that exposed Cr can support martensitic transformation in sensitized austenitic stainless steels [38], Lai et al. and Kain et al. proposed that deformation-induced martensite may enhance sensitization due to faster diffusion through martensite [39,40], Hanninen believes that SCC resistance can be improved with high level of martensite via cathodic protection [32], Andresen and Morra concluded that SCC is not affected by martensite but by slip planes and dislocation density [37] whereas others proposed martensite as a trapping site for hydrogen which increases resistance to hydrogen embrittlement [41].

2.3.2. Sensitization

Related to cracking in austenitic stainless steel is sensitization that occurs upon arc welding in fabrication of austenitic stainless steels and it was first observed in a region of heat affected

zone (HAZ) next to the weld that becomes susceptible to corrosion, thus it is also known as weld-decay. Within a critical temperature range of 425-870 °C, carbon can precipitate out as carbides and combine with chromium at grain boundaries to form $(Cr_{0.7-0.8}Fe_{0.2-0.3})_{23}C_6$ [42]. Carbon as a small interstitial atom moves swiftly whereas the chromium as substitutional atoms move slower. The formation of chromium carbide precipitates at grain boundaries as shown in Fig. 2.10 attract carbon from the grains whereas chromium is pulled from the local regions to grain boundaries. Chromium depletion occurs when the chromium content decreases below 12% as shown in Fig. 2.11, a level insufficient to retain a passive oxide film which causes the microstructure to be susceptible to corrosion and can lead to intergranular cracking [1].

Many investigators observed intergranular fracture of sensitized austenitic stainless steels in their study such as by Berry et al. on the effect of oxygen on SCC where the intergranular fracture occurs independent of sensitization type [43], by Theus and Cels in fluoride solutions [44] and by Hishida and Nakada on the effect of chloride in high-temperature water [45] confirming the correlation between intergranular cracking and sensitized stainless steels.

Although sensitization in austenitic stainless steels leads to intergranular cracking, there are several ways to prevent sensitization of stainless steel and thus, intergranular cracking [46]:

1. Decreasing carbon to less than 0.03% to avoid the formation of chromium carbide
2. Increasing chromium content to avoid decrease to below 12%
3. Adding titanium (Ti) and/or niobium (Nb) to form titanium carbide (TiC) and niobium carbide (NbC) which stabilize stainless steel
4. Avoiding the sensitization temperature regime between 425-870 °C as shown in Fig. 2.12
5. Performing quench annealing heat treatment by heating to more than 870 °C and then quench below 425 °C as shown in Fig. 2.13.

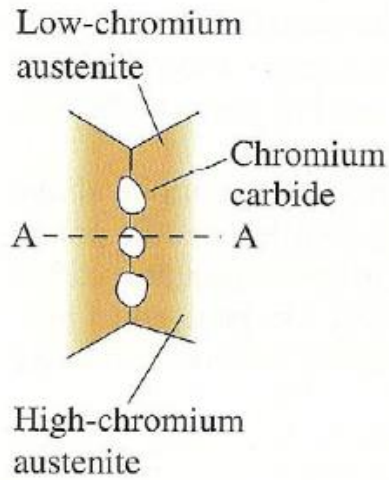


Figure 2.10. Precipitation of chromium carbides at grain boundaries due to slow cooling [46].

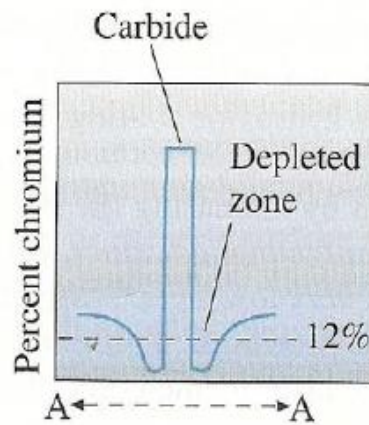


Figure 2.11. The depleted zone of chromium below 12% [46].

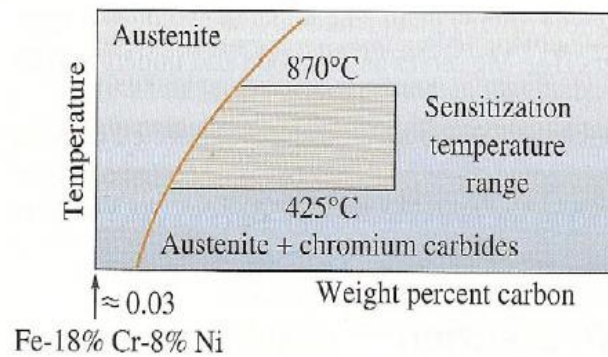


Figure 2.12. Sensitization temperature range of austenitic stainless steels [46].

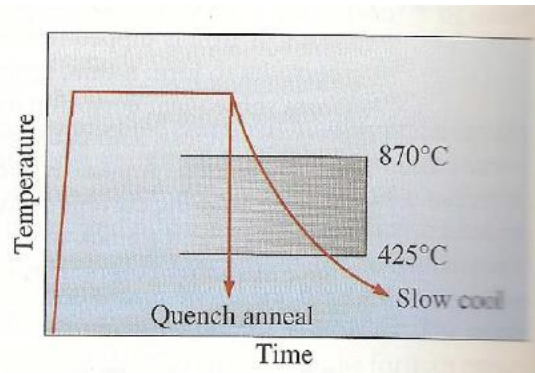


Figure 2.13. Quench anneal heat treatment of austenitic stainless steels [46].

2.3.3. Composition

Resistance to SCC of austenitic stainless steels can be improved through compositions. Addition of Ni has been reported to improve SCC resistance of austenitic stainless steels in chloride environments [47, 48]. Additions of Mo less than 5% as well as Cr contents of less than 15% and more than 25% also enhance SCC resistance of austenitic stainless steels [49]. There are also other elements that reduce SCC resistance of austenitic stainless steels such as phosphorus (P) that promotes hydrogen entry to the metal thus increasing the rate of hydrogen evolution on the surface of steels [50,51]. Additionally, increasing manganese (Mn) reduces the volume fraction of austenite, and changes the shape and size of the austenite which affects the pitting resistance and reduces the SCC susceptibility of steels [52].

Pitting corrosion is a localized corrosion which generates pits on the metal surface that can take place in neutral environments and the severity of localized corrosion (passive film breakdown and pit initiation) is enhanced in chloride environment [53]. Stainless steels are susceptible to this localized corrosion since corrosion will occur at a higher rate at one surface area than the rest of the surface. The pits sometimes undercut the surface that the real cross-section of the pit is larger than the observed pit cross-section on the metal surface [54,55]. During pitting corrosion, a passive

film is damaged to form an anode and the undamaged film forms a cathode. From the anode, the localized corrosion will speed up and pits will be created where the corrosion then propagates even faster due to the electrolyte inside the expanding pit [56,57]. It has been investigated that high chloride concentration, low pH, high temperature and dissolved oxygen are the suitable conditions for pitting initiation and propagation of stainless steels. As temperature is one of the important factors in pitting corrosion, it is imperative to introduce critical pitting temperature (CPT) which is the temperature at which pitting starts [54]. Temperature strongly influences the rate of any chemical reactions including corrosion where the higher the temperature, the faster the corrosion process and therefore, the worse the corrosion resistance [58].

The effect of composition on pitting and corrosion resistance of stainless steels can be quantified by a pitting resistance equivalent (PRE) number [59-62]. It gives a number that indicates the pitting resistance where the higher the number, the better the pitting resistance. As N has been found to improve the pitting resistance of stainless steels, PRE_N is often specified instead of PRE to quantify the pitting resistance equivalent of a composition containing nitrogen, expressed as [63-66]

$$PRE_N = \%Cr + 3.3 \times \%Mo + 30 \times \%N \quad (2.7)$$

The biggest contributing factor in the PRE equation is Cr as there is at least a hundred times more Cr than N by weight. For stainless steels consisting of tungsten, the PRE equation is modified slightly as [63-66]

$$PRE = \%Cr + 3.3 \times (\%Mo + 0.5\%W) + 30 \times \%N \quad (2.8)$$

2.3.4. Stress

Tensile stress is one of the three conditions needed for SCC to occur and so, it is important to understand the effect of stress in SCC. It is reported that increasing applied tensile stress decreases the time to failure in SCC [67] although it does not increase rate of crack propagation [68-71]. At stress levels lower than those suitable to fracture materials, the cracks form and propagate perpendicularly to the axis of the applied tensile stress [72,73]. Effect of applied tensile stress on time to failure was examined by Jiang and Staehle with several different austenitic stainless steels [74] whereas the effect of stress intensity factor on crack growth rate was investigated Andresen and Ford [70].

A typical schematic of crack growth rate as a function of stress intensity factor is illustrated in Fig. 2.14 [75] where there are three different stages. In the first stage, crack propagates in a way that its plane is perpendicular to the axis of the applied tensile stress. In the second stage, the crack growth rate is independent of the stress intensity factor and this region is used to obtain the average crack growth rate value. In the third stage, crack growth rate increases with stress intensity factor until K_{IC} is reached where then the specimen fractures [76-79].

It is reported that crack tip stress intensity, not the applied tensile stress, dictates the crack growth rates in SCC. The crack tip stress intensity alters the local stress field, thereby decreasing the stress on the sides of the crack which suggests that the stress will increase again to initiate a crack. Hence, increasing applied tensile stress does not increase crack propagation rate [80]. Jivkov and Marrow believe that SCC can occur regardless of the level of stress intensity factor [81].

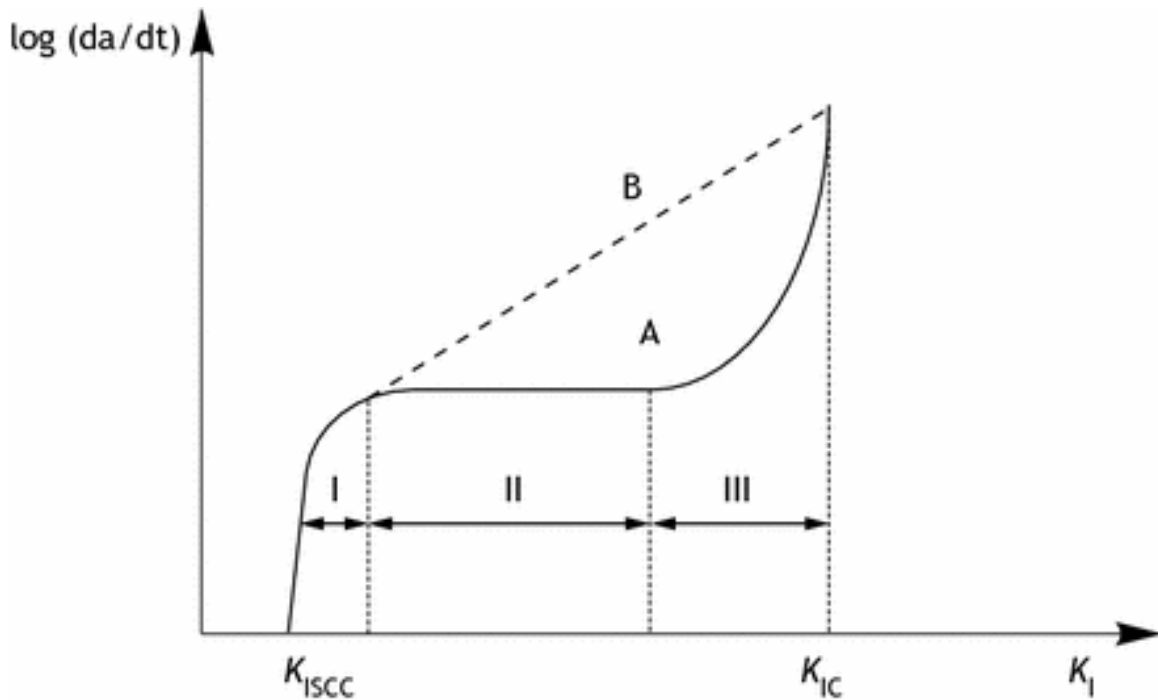


Figure 2.14. A schematic depiction of crack growth rate with stress intensity factor [75].

2.3.5. Environment

There are many factors affecting SCC such as temperature, solution composition and pH. Each of these factors will be described in the following sections.

2.3.5.1. Temperature

It has been reported that SCC can occur at temperatures starting at 25 °C and mostly between 50 – 200 °C for atmospheric SCC [81]. ASM International proposed a predictive model between crack propagation rate and temperature for intergranular stress corrosion cracking (IGSCC) as shown in Fig. 2.15 [83].

Temperature dictates the speed of the particles' movement and their collision frequency. Particles that collide with enough minimum energy (activation energy) will result in a reaction. Increasing temperature increases the number of high energetic particles and their collision

frequency resulting in an increase of reaction rate. As in any chemical reaction, corrosion rate is also strongly dependent on temperature where the higher the temperature, the faster the corrosion process and therefore, the worse the corrosion resistance [58, 84]. Van Gelder et al. reported that temperature may have the biggest contribution among other environmental conditions to SCC [85]. From the perspective of stress and temperature, SCC is a corrosion process involving mechanical and chemical processes resulting in cracking of a material that later loses its mechanical strength from fracture and catastrophic failure without preliminary indications of metal loss and damage.

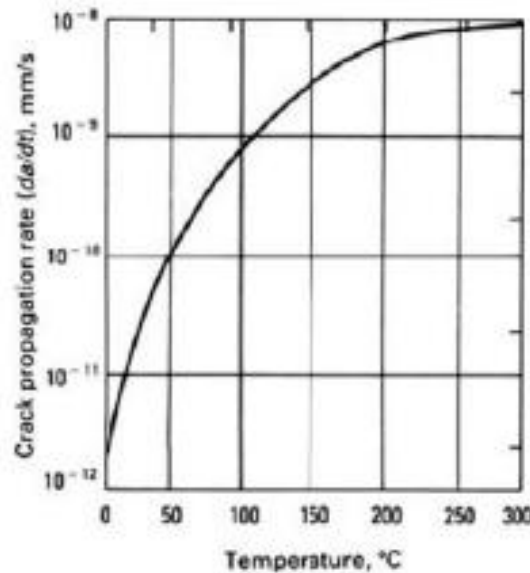


Figure 2.15. A model of crack propagation as a function of temperature for IGSCC in 304 by ASM International [83].

2.3.5.2. Solution composition

Chloride environment is the most popular environment encountered in SCC of stainless steels with many SCC studies conducted in sodium chloride (NaCl), magnesium chloride (MgCl₂), calcium chloride (CaCl₂) and lithium chloride (LiCl) [86-95]. It is interesting to note that SCC was not observed in anhydrous aluminum chloride (AlCl₃), potassium chloride (KCl) and iron III chloride (FeCl₃) melts [96]. Dean suggested that chloride ions play a role in the destruction and

hindrance of formation of passive surface films where chloride ions tend to accumulate at regions of high stress [97]. Mallinson shared the same observation on the role of chloride ions that they remove the antioxidant or passive surface film from the surface of a material and initiate the oxidation process [98]. A small amount of chlorine in a solution is sufficient to initiate SCC, the location of where the chlorine is present in the material such as the crack tip is more important. With sufficient chlorine, crack will grow from the crack tip [61]. Theus and Staehle reported that SCC susceptibility is enhanced in sensitized steels with increasing chloride ions or oxygen concentration [48]. Similar observations were also made by Berry et al. [43] and Clark and Gordon [99] indicating that in SCC of austenitic stainless steels, water produces readily reducible species in the form of H^+ or O_2 .

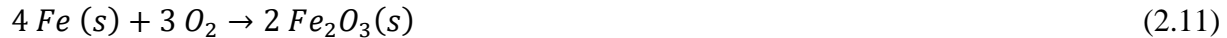
SCC of austenitic stainless steels was also observed in magnesium bromide ($MgBr_2$) solutions [96], fluoride environments less than 10 parts per million (ppm) at room temperature [100,101] and caustic solutions for example sodium hydroxide ($NaOH$) and potassium hydroxide (KOH) above boiling temperatures [102,103]. The SCC susceptibility of SS304L in caustic solutions occurs above 100 °C but it can take place at 50 °C with the addition of sulfide ions as they enhance the susceptibility of austenitic stainless steels to caustic solutions [104,105]. Sulfide ions can be present in the form of HS^- , S^{2-} and polysulfides [106]. In the pulp industry, sulfur anions such as thiosulfate ($S_2O_3^{2-}$), sulfite (SO_3^{2-}) and sulfate (SO_4^{2-}) may exist [107]. Polysulfides and thiosulfates are reported to enhance the corrosion of mild steel [108]. Enhanced corrosion of steel or mild steel passivation with reduced corrosion rate can occur by increasing the amount of polysulfides [109]. On the other hand, no SCC was observed in sulfite, sulfate and iodide environments [109, 110].

2.3.5.3. pH

Besides temperature and solution composition, SCC is also affected by the pH of the environment as it affects the electromigration process. Information on the stability of metals in different pH conditions is illustrated in Pourbaix diagram developed by Marcel Pourbaix [111] where it summarizes the corrosion thermodynamic information for a given metal by indicating its potential as a function of pH. Figure 2.16 displays the Pourbaix diagram for Fe where it indicates certain regions of potential and pH where a metal undergoes corrosion and where a metal is protected from corrosion [111]. In the Pourbaix diagram, liquid water is stable in the region between the two dotted lines indicating that water is unstable relative to hydrogen gas (H₂) below the H₂ line (lower dotted line) and water is unstable relative to oxygen (O₂) above the O₂ line (upper dotted line). With Fe stable below the H₂ line, Fe is unstable in water [112] in acid and base, respectively.



Closer to the O₂ line, Fe₂O₃ is formed based on the reaction



where the oxide forms a protective coating on the metal passivating the surface and reduces the corrosion reaction of iron in solutions containing oxygen [112].

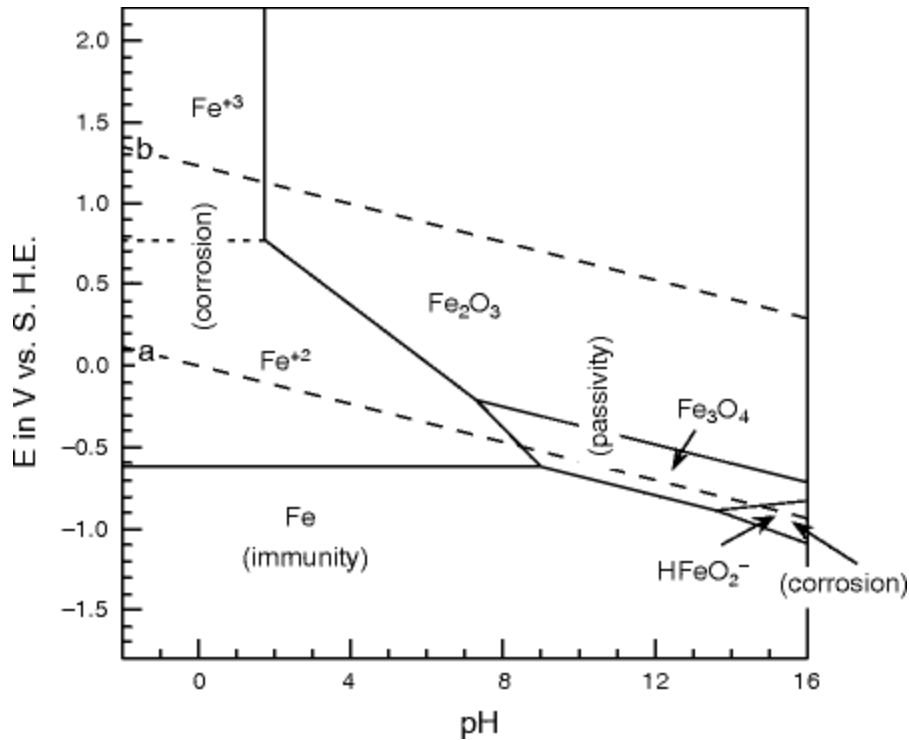
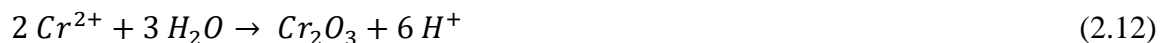


Figure 2.16. Pourbaix diagram for iron [111].

It has been reported that the crack tip environment is not necessarily the same with the bulk solution environment which makes the pH at the crack tip and the bulk solution to be different as well. Investigations were made on the conditions of the two locations by Suzuki et al. [113], Baker et al. [114] with austenitic stainless steels 304L and 316L and Sandoz et al. [115] with different steels all in NaCl solution where they all observed lower pH at the crack tip compared to that in the bulk solution. They suggested that the combination of high chloride concentration and hydroxychloro complexes of dissolved metal ions produces the low pH values at the crack tip [113-115]. Baker et al. further proposed a metal ion-oxide hydrolysis reaction [114], Eq. 2.12 that may produce an oxide film on the internal crack surfaces.



This proposed reaction is confirmed by Wilde where he noted a lower Cr content after his SCC experiments using $MgCl_2$ solution as compared to that from the alloy corrosion [116]. The low pH at the crack tip can be preserved where the hydrogen ions will undergo reduction away from the crack tip.

2.4. Mechanisms of SCC

Mechanisms of SCC are divided into those based on active path models that rest on anodic dissolution at crack tip region for crack propagation such as stress-assisted localized corrosion and slip dissolution and based on mechanical models such as hydrogen embrittlement and strain-induced transformation.

2.4.1. Chromium depletion

Chromium depletion model is proposed for SCC mechanism based on stress-assisted localized corrosion where tensile stress acts to speed up the mechanical failure of the material. This model was initially developed by Bain et. al., to find out what causes the corrosion of sensitized stainless steels [117]. They observed that a chromium depleted zone nearby the region of chromium carbides prompted the susceptibility of sensitized austenitic stainless steels to IGSCC. The formation of chromium carbide precipitates at grain boundaries as depicted in Fig. 2.10 attract carbon from the grains whereas chromium is pulled from the local regions to grain boundaries. Chromium depletion occurs as the chromium content decreases below 12%, a level insufficient to retain a passive oxide film which causes the microstructure to be susceptible to corrosion and leads to IGSCC [1].

This model was also confirmed by several other investigators. A diffusion-controlled model was derived by Stawstrom and Hillert where they included chromium carbide precipitates with uniform chromium concentration at grain boundaries and chromium depleted zone [118]. They proposed that the local equilibrium of chromium carbide $(\text{Cr}_{0.7-0.8}\text{Fe}_{0.2-0.3})_{23}\text{C}_6$ precipitates thermodynamically governs the content of Cr whereas the annealing temperature and carbon content dictate the minimum Cr content. In addition, they also speculated that the elimination of chromium depleted zone can take place with carbide precipitation.

An identical model was also developed by Tedmon et al. in which they considered non-uniform Cr concentration between the carbides at the grain boundary [119]. They determined the Cr concentration with respect to distance from the carbides using a thermodynamic analysis. Experimental observations indicated that non-uniform Cr concentration occurred between the carbides at a grain boundary which led to a conclusion that a non-uniform attack occurred at the grain boundaries and a non-uniformly sensitized grain boundary could exist.

2.4.2. Slip dissolution

The slip dissolution model also known as the film rupture model was suggested by Champion that hinges on the passive film rupture due to plastic deformation at the crack tip and anodic dissolution of the metal which sharpens the crack tip, increases stress concentration at the crack tip, promotes successive deformation and film rupture [120]. The strain at the crack tip promotes a surface offset or step where the metal surface and the slip plane intersect causing rupture of protective film. Crack continues to propagate since repassivation of the crack tip is not considered in Champion's model. A similar model that incorporated repassivation of the crack tip was proposed by Staehle and Vermilyea [121-123] where Staehle accused slip events to be the

root of the film rupture [121] and Vermilyea suggested that the strain in the film causes the film rupture without including slip events [122,123]. Crack propagates as a result of repeating mechanism of film rupture, anodic dissolution and film repassivation as illustrated in Fig. 2.17 [124].

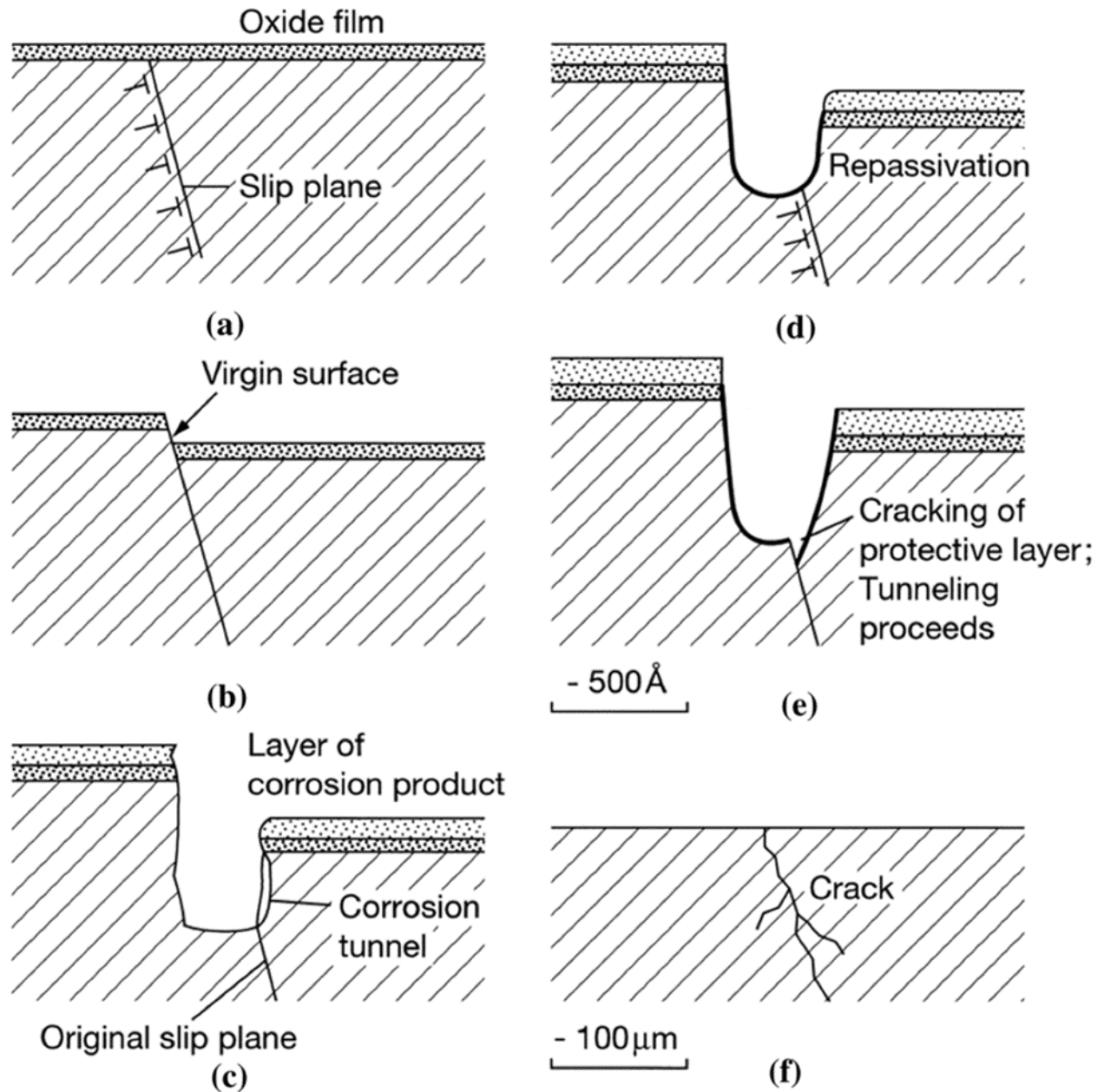


Figure 2.17. A schematic diagram of slip dissolution model consisting of film rupture, anodic dissolution and film repassivation [124].

Scully believes that slip mode, crack tip potential drop, repassivation rate and strain rate are the vital parameters [125]. The role of slip mode in determining the height of the slip step was observed by Silcock and Swann in their studies with SS316 where the slip step height must be greater than the passive film thickness for the slip dissolution model to be active [126, 127]. On the other hand, the role of potential drop was verified by Doig and Flewitt in their SCC experiment using NaOH [128, 129]. Ford and Povich in their study using SS304 in H₂O and SO₄²⁻ concluded that the dissolution rate of the metal surface dictates the crack propagation rate [130-132].

Passive film on the metal surface may be ruptured as a result of strain which then initiates cracks [133]. Pit initiation has been detected by other investigators that becomes tunnels as a result of different dissolution rates between different crystallographic directions and different dissolution rates between different elements [134,135]. This tunnel formation then promotes SCC along with the observed fractures on the metal surface. The crack propagation is dictated by the oxidation process, system thermodynamics, system kinetics and film repassivation. The features of IGSCC can be observed using this model due to the slower repassivation rate at grain boundaries as compared to that in the grains.

2.4.3. Hydrogen embrittlement

Hydrogen embrittlement is another SCC mechanism that occurs as a result of hydrogen evolution on the surface of a metal, causing hydrogen penetration to the metals (hydrogen adsorption) which later leads to crack growth, SCC and brittle fracture of the metals [136,137]. Hydrogen atoms can be created by electrochemical reaction in solution (hydrogen production at cathode) or hydrogen dissociation in hydrogen gases. The correlation between hydrogen and SCC was confirmed by Barth and Troiano where they concluded that electrochemical conditions are

vital in governing the hydrogen evolution rate and they noted that acidic crack tip enhances proton reduction [138]. Brittle intergranular fracture was noticed by Briant in static tests in hydrogen environments with stainless steels [139]. Hydrogen embrittlement in metals causes reductions in area, K_{IC} and fracture stress at failure. An illustration of hydrogen embrittlement model for SCC mechanism is shown in Fig. 2.18 [140].

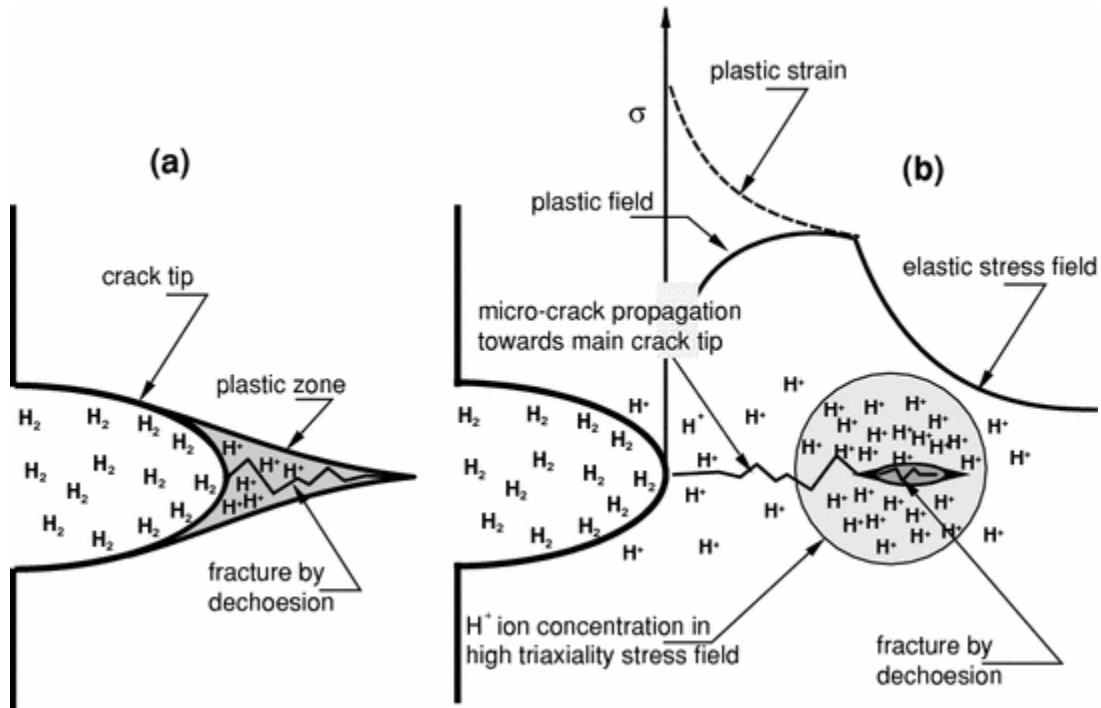


Figure 2.18. A depiction of hydrogen embrittlement model for SCC mechanism [140].

Some investigators believe that hydrides formed in SCC of austenitic stainless steels [141,142] present paths for brittle fracture via the formation of hydride phase or serve as obstacles to dislocation motion, stimulating brittle fracture of the matrix. However, an investigation of hydrogenated surface layers in SS304L, 310 and 316L indicated that hydride does not form in austenitic stainless steels [143] and they are apparently ϵ -martensite [144-146].

Hydrogen can also link with dislocation pile-ups to promote brittle fracture. Hydrogen production decreases the number of cross-slip by forming dislocations and enhances vacancy diffusion in front of the crack tip leading to a decrease in K_{IC} so cracks can be formed at lower stress intensity. More dislocations are formed during plastic deformation at the crack tip which increases the dislocation-obstacle interaction shifting the stress concentration along with the crack tip. Cracks can then propagate and dislocations glide through the next slip plane. This mechanism repeats to create a zigzag pattern [147-150]. The dislocation-obstacle interaction is displayed in Fig. 2.19 [151].

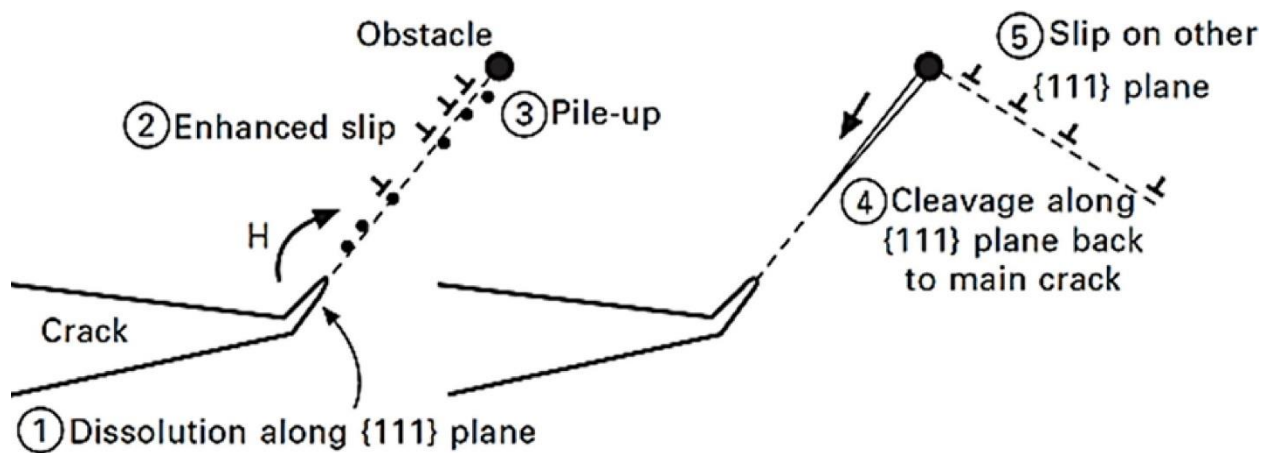


Figure 2.19. Dislocation-obstacle interaction in hydrogen enhanced plasticity model [151].

2.4.4. Strain-induced martensite formation

Martensite plays a role in SCC as strain contributes to the formation of martensite in austenitic stainless steels where the martensite serves as the pre-existing route for crack propagation [152]. Thin foils made of SS304 were immersed in a solution of $H_2SO_4 + NaCl$ to investigate the strain-induced martensite formation where pits were detected along the martensite

bands, and α' and ϵ martensites were responsible for crack initiation and propagation, respectively [153,154].

Some investigators believe that hydrides form in SCC of austenitic stainless steels [141,142] although an investigation of hydrogenated surface layers in SS304L, 310 and 316L indicated that hydride does not form in austenitic stainless steels [143] where they were identified as ϵ -martensite [144-146]. It is suggested that the martensite forms due to lattice expansion as hydrogen atoms at the crack tip penetrate the γ lattice [96]. Another investigation showed that hydrogen segregates at α' interface, ϵ/γ interface or grain boundaries [155,156]. Many researchers did not consider ϵ -martensite in SCC although it plays a role in SCC.

2.5. Intergranular crack propagation

IGSCC occurs in sensitized austenitic stainless steels due to precipitation of chromium rich carbide at the grain boundary. Carbon can precipitate out as carbides in the sensitization temperature range and combine with chromium at grain boundaries to form $(Cr_{0.7-0.8}Fe_{0.2-0.3})_{23}C_6$ [42]. Carbon as a small interstitial atom moves swiftly whereas the chromium as substitutional atoms move slower. The chromium carbide precipitates at grain boundaries attracts carbon from the grains whereas chromium is pulled from the local regions to grain boundaries. Chromium depletion occurs in the regions close to grain boundaries, and when the chromium content decreases below 12% the region becomes sensitive to corrosion. This causes the bare microstructures in the grain boundary to be susceptible to aggressive chemical species and thus, cracks propagate through the grain boundary, known as intergranular cracking [1]. An intergranular cracking in sensitized SS304 specimen obtained from one of the crack growth experiments in the project is shown in Fig. 2.20.

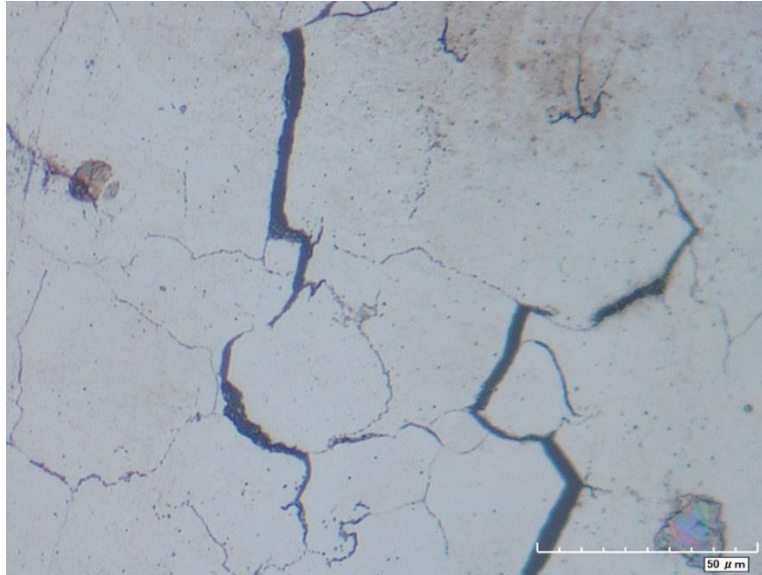


Figure 2.20. Intergranular cracking in sensitized SS304.

2.6. Fracture mechanics

SCC can be characterized by measuring the fracture toughness of a material. In materials that exhibit linear elastic condition, the fracture toughness is denoted by the parameter, K , the stress intensity factor. The stress intensity factor is usually given a subscript to denote the loading mode, K_I , K_{II} or K_{III} . There are three modes of loading that can be applied to a crack as shown in Fig. 2.21 [157].

Mode I loading occurs when the load is applied normal to the crack plane and as a result, it opens the crack. Mode II loading corresponds to in-plane shear loading resulting in sliding one crack face with respect to the other and thus called the sliding mode. Mode III loading corresponds to out-of-plane shear loading, resulting in tearing mode. Mode I loading is the most common mode of fracture and is expressed by [157]

$$K_I = Y\sigma\sqrt{\pi a} \quad (2.13)$$

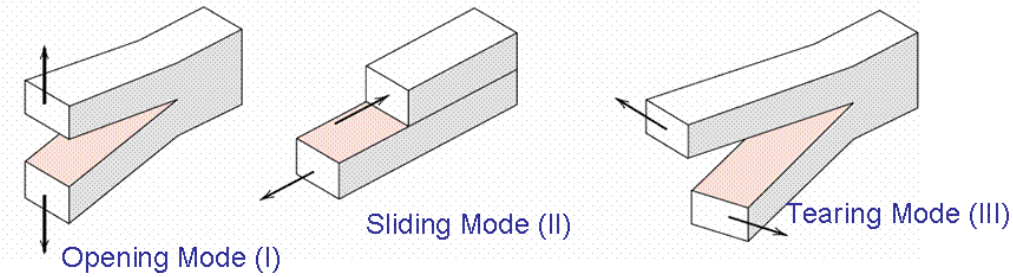


Figure 2.21. Three modes of fracture [157].

where K_I is the stress intensity factor for mode I loading, Y is a geometry factor which is a function of specimen's thickness and crack length, σ is the applied stress and a is the edge crack length or half internal crack length. Given the applied stress and measured crack length, the stress intensity factor can then be determined.

The stress intensity factor K_I becomes plane strain fracture toughness K_{IC} when plane strain condition exists where the specimen thickness, $B > 2.5 \left(\frac{K_{IC}}{\sigma_y} \right)^2$ [23]. If $K_I < K_{IC}$, fracture will not occur in non-corrosive environment but it will in a corrosive environment. To avoid fracture of a component in a corrosive medium, $K_I < K_{ISCC}$, the threshold stress intensity factor in SCC environment. The difference between plane stress and plane strain conditions are shown in Fig. 2.22 [24] and 2.23 [23].

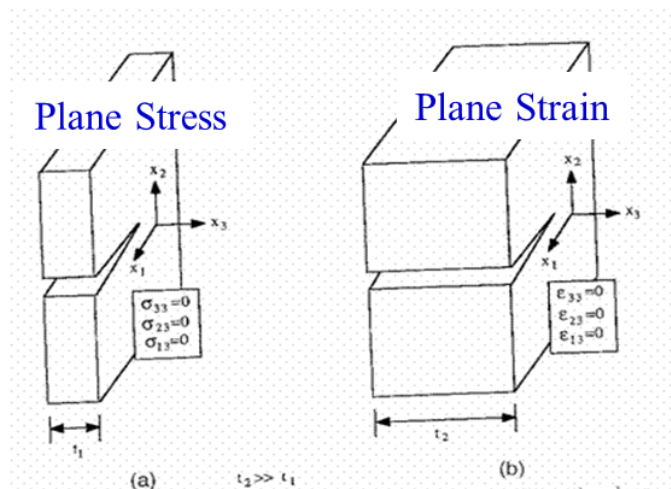


Figure 2.22. Plane stress and plane strain condition [24].

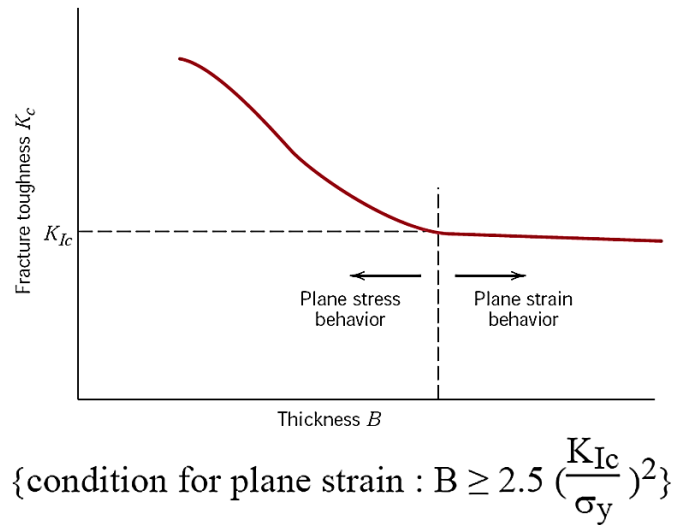


Figure 2.23. Fracture toughness as a function of specimen thickness in plane stress and plane strain behavior [23].

One way to determine the stress intensity factor in SCC environment, K_{ISCC} , is as follows. The load can be applied by an instrumented bolt such that K_I is below K_{IC} . In the case of constant displacement test, the load will drop as crack propagates. The crack will continue to propagate as long as K_I is greater than K_{ISCC} . As a result, useful information for the prediction of the SCC behavior of a material such as crack length as a function of time (a vs t), stress intensity factor as a function of time and crack length (K_I vs t and K_I vs a), and crack growth-rate as a function of stress intensity factor ($\log \frac{da}{dt}$ vs K_I) can be obtained [158]. There are three important stages in the behavior of crack growth rate as a function of stress intensity factor. In the first stage, crack propagates in a way that its plane is perpendicular to the axis of the applied tensile stress. In the second stage, the crack growth rate is independent of the stress intensity factor and this region is used to obtain the average crack growth rate value. In the third stage, crack growth rate increases with stress intensity factor until K_{IC} is reached where then the specimen fractures [76-79].

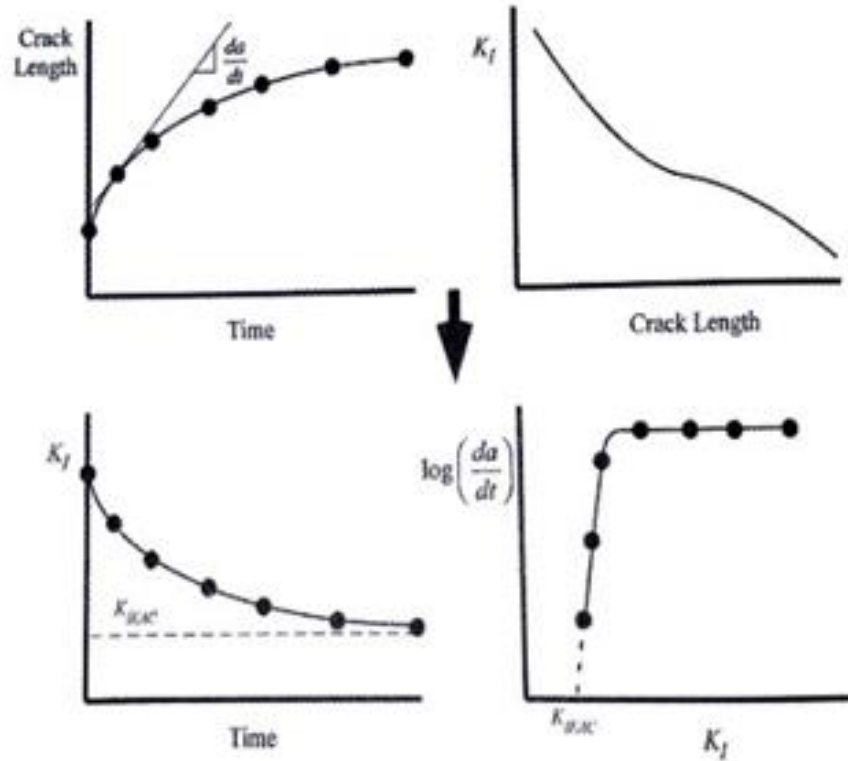


Figure 2.24. Outcomes from determining stress intensity factor in SCC environment [158].

The determination of K_{ISCC} and average crack growth rates by fracture mechanics will be useful in predicting the integrity of a structure under a certain loading condition which in turn will help in assessing its useful life in a marine environment.

2.7. References

- [1] J. Beddoes, J.G. Parr, Introduction to Stainless Steels, 3rd ed., ASM International, Ohio, 1999.
- [2] R. A. Lula, Stainless Steels, A.S.f. Metals, Metals Park, Ohio, 1986.
- [3] J. R. Davis, A. S. M. I. H. Committee, Stainless Steels, ASM Specialty Handbook, ASM International, Materials Park, Ohio, 1994.
- [4] Tec-science, Important Types of Lattice Structures. <https://www.tec-science.com/material-science/structure-of-metals/important-types-of-lattice-structures/>, 2019 (accessed September 2, 2019).
- [5] F. W. Brust, P.M. Scott, Weld Residual Stresses and Primary Water Stress Corrosion Cracking Bimetal Nuclear Pipe Welds, PVP 2007, San Antonio, TX, July 22-26, 2007, Paper Number PVP2007-26297, 883, 2007.
- [6] T. Mintz, L. Caseres, D. Dunn, M. Bayssie, Atmospheric Salt Fog Testing to Evaluate Chloride Induced Stress Corrosion Cracking of Type 304, 304L, and 316L Stainless Steel, San Antonio, TX, March 14-18, 2010.
- [7] G. E. Dieter, Mechanical Metallurgy, 3rd ed, McGraw-Hill Book Company, Singapore, 1989.
- [8] A. S. M. Handbook, N. Ed, Vol. 12: Fractography, 1987.
- [9] Aalco, Ferrous and Non-Ferrous Metals Stockist. Precipitation Hardening Stainless Steels – Alloys, Properties, Fabrication Processes. AZoM. <https://www.azom.com/article.aspx?ArticleID=2819>, 2019 (accessed September 02, 2019).
- [10] A. J. Sedriks, Corrosion of Stainless Steels, Corrosion monographs series, Electrochemical Society, Wiley, New York, 1996.
- [11] R. N. Gunn, Duplex Stainless Steels: Microstructure, Properties and Applications, Cambridge, England: Abington Pub, 1997.

- [12] I. Alvarez-Armas, Duplex Stainless Steels: Brief History and Some Recent Alloys, Recent Patents on Mechanical Engineering 1 (2008) 51-57.
<https://doi.org/10.2174/2212797610801010051>.
- [13] J. Olsson, M. Snis, Duplex – A New Generation of Stainless Steels for Desalination Plants, Desalination 205 (2007) 104-113.
- [14] K. L. Murty, Properties of Materials: Corrosion, Raleigh, NC, Chapter 5, NE/MSE 509 (2016).
- [15] M. Elmahdy, What Causes Stress Corrosion Cracking in Pipelines? Corrosionpedia.
<https://www.corrosionpedia.com/what-causes-stress-corrosion-cracking-in-pipelines/2/1404>, 2017 (accessed May 25, 2017).
- [16] A. Turnbull, Stress Corrosion Cracking: Mechanisms, Encyclopedia of Materials: Science and Technology (2001) 8886-8892.
- [17] R. H. Jones, Stress Corrosion Cracking, ASM International, Materials Park, Ohio, 1992.
- [18] P. Combrade, Stainless Steels, 1993.
- [19] EPRI, EPRI Flaw Growth and Flaw Tolerance Assessment for Dry Cask Storage Canisters, Presentation to the NRC, August 5, 2014.
- [20] C. Bryan, D. Enos, Analysis of Dust Samples Collected from Spent Nuclear Fuel Interim Storage Containers at Hope Creek, Delaware, and Diablo Canyon, California, SAND2014-16383, Sandia National Laboratories, Albuquerque, NM. 281 p., 2014.
- [21] G. Wu, M. Modarres, A Probabilistic-Mechanistic Approach to Modeling Stress Corrosion Cracking in Alloy 600 Components with Applications, Presentation, PSAM 2011, 2012.
- [22] N. Kumar, K.L. Murty, Overview of Fracture Mechanics K_{ISCC} - J_{ISCC} and Experimental Setup, NCSU, Raleigh, NC, 2015.

- [23] D. D. Johnson, Mechanical Failure.
https://nanohub.org/resources/6186/download/ch09_fracture.pdf, 2008 (accessed 16 November 2015).
- [24] N. Perez, Linear-Elastic Fracture Mechanics, in: Fracture Mechanics, Springer, Switzerland, 2017, pp. 79-130.
- [25] E. Generalic, Body-centered tetragonal lattice. Croatian-English Chemistry Dictionary & Glossary. 20 Oct. 2018. KTF-Split. <https://glossary.periodni.com/glossary.php?en=body-centered+tetragonal+lattice>, 2018 (accessed Sep 4, 2019).
- [26] R. L. Cowan II, G. M. Gordon, Stress Corrosion Cracking and Hydrogen Embrittlement of Iron Base Alloys, INACE (1977) 893.
- [27] S. Floreen, The Physical Metallurgy of Maraging Steels, Met. Rev. 13 (1968) 115-128.
<https://doi.org/10.1179/mtlr.1968.13.1.115>.
- [28] R. P. Reed, The Spontaneous Martensitic Transformations in 18% Cr, 8% Ni Steels, Acta Met. 10 (1962) 865-877. [https://doi.org/10.1016/0001-6160\(62\)90101-3](https://doi.org/10.1016/0001-6160(62)90101-3).
- [29] J. Nutting, JISI 207 (1969) 872-893.
- [30] W. D. Callister, D. G. Rethwisch, Hexagonal Close Packed Crystal Structure (HCP), Fundamentals of Materials Science and Engineering: An Integrated Approach, 5th ed, Wiley, 2016.
- [31] P. L. Mangonon, G. Thomas, Structure and Properties of Thermal-Mechanically Treated 304 Stainless Steel, Met. Trans. 1 (1970) 1587-1594. <https://doi.org/10.1007/BF02642004>.
- [32] H. E. Hanninen, Influence of Metallurgical Variables on Environment-Sensitive Cracking of Austenitic Alloys, Int. Met. Rev. 24 (1979) 85-136.
<https://doi.org/10.1179/imtr.1979.24.1.85>.

- [33] I. Shakhova, V. Dudko, A. Belyakov, K. Tsuzaki, R. Kaibyshev, Effect of Large Strain Cold Rolling and Subsequent Annealing on Microstructure and Mechanical Properties of An Austenitic Stainless Steel, *Mater. Sci. Eng. A.* 545 (2012) 176-186.
<https://doi.org/10.1016/j.msea.2012.02.101>.
- [34] L. Peguet, B. Malki, B. Baroux, Effect of Austenite Stability on the Pitting Corrosion Resistance of Cold Worked Stainless Steels, *Corros. Sci.* 51 (2009) 493-498.
- [35] L. Peguet, B. Malki, B. Baroux, Influence of Cold Working on the Pitting Corrosion Resistance of Stainless Steels, *Corros. Sci.*, 49 (2007) 1933-1948.
<https://doi.org/10.1016/j.corsci.2006.08.021>.
- [36] G. Lu, H. Cheng, C. Xu, Z. He, Effect of Strain and Chloride Concentration on Pitting Susceptibility for Type 304 Austenitic Stainless Steel, *Chinese J. Chem. Eng.* 16 (2008) 314-319. [https://doi.org/10.1016/S1004-9541\(08\)60080-4](https://doi.org/10.1016/S1004-9541(08)60080-4).
- [37] P. L. Andresen, M. M. Morra, IGSCC of Non-sensitized Stainless Steels in High Temperature Water, *J. Nucl. Mater.* 383 (2008) 97-111.
<https://doi.org/10.1016/j.jnucmat.2008.08.005>.
- [38] E. P. Butler, M. G. Burke, Chromium Depletion and Martensite Formation at Grain Boundaries in Sensitized Austenitic Stainless Steel, *Acta Metall.* 34 (1986) 557-570.
[https://doi.org/10.1016/0001-6160\(86\)90091-X](https://doi.org/10.1016/0001-6160(86)90091-X).
- [39] C. L. Lai, L. W. Tsay, W. Kai, C. Chen, Notched Tensile Tests of Cold-Rolled 304L Stainless Steel in 40wt% 80 °C MgCl₂ Solution, *Corros. Sci.* 51 (2009) 380-386.
<https://doi.org/10.1016/j.corsci.2008.11.007>.

- [40] V. Kain, K. Chandra, K. N. Adhe, P. K. De, Effect of Cold Work on Low-Temperature Sensitization Behavior of Austenitic Stainless Steels, *J. Nucl. Mater.* 334 (2004) 115-132. <https://doi.org/10.1016/j.jnucmat.2004.05.008>.
- [41] S. M. Teus, V. N. Shyvanyuk, V. G. Gavriljuk, Hydrogen-induced $\gamma \rightarrow \epsilon$ Transformation and the Role of ϵ -martensite in Hydrogen Embrittlement of Austenitic Steels, *Mater. Sci. Eng. A.* 497 (2008) 290-294. <https://doi.org/10.1016/j.msea.2008.07.003>.
- [42] R. N. Younger, R. G. Baker, R. Littlewood, The Relationship Between Microstructure and Intercrystalline Corrosion in An 18Cr-12Ni-1Nb Austenitic Steel, *Corros. Sci.* 2 (1962) 157-160. [https://doi.org/10.1016/0010-938X\(62\)90007-0](https://doi.org/10.1016/0010-938X(62)90007-0).
- [43] W. E. Berry, E. L. White, W. K. Boyd, Stress Corrosion Cracking of Sensitized Stainless Steel in Oxygenated High Temperature Water, *Corrosion* 29 (1973) 451-469. <https://doi.org/10.5006/0010-9312-29.12.451>.
- [44] G. J. Theus, J. R. Cels, *Corrosion Problems in Energy Conversion and Generation*, The Electrochemical Society, New York, 1974.
- [45] M. Hishida, H. Nakada, Constant Strain Rate Testing of Type 304 Stainless Steel in High Temperature Water-Part II: An Investigation of the Chloride Effect on Stress Corrosion Cracking, *Corrosion* 33 (1977) 403-407. <https://doi.org/10.5006/0010-9312-33.11.403>.
- [46] D. Askeland, P. Fulay, W. Wright, D. K. Bhattacharya, *The Science and Engineering of Materials*, 6th ed. Cengage Learning, Canada, 2011.
- [47] H. R. Copson, *Physical Metallurgy of Stress Corrosion Fracture*, Interscience, New York, 1959.

- [48] G.J. Theus, R.W. Staehle, Stress Corrosion Cracking and Hydrogen Embrittlement of Iron Based Alloys, in: R.W. Staehle, J. Hockman, R.D. McCright, J.E. Slater (Eds.), NACE-5, Houston, TX, 1977, pp. 845–92.
- [49] R. M. Latanision, R.W. Staehle, Proc. Conf. on Fundamental Aspects of Stress Corrosion Cracking, in: R. W. Staehle, A. J. Forty, D. Van Rooyen (Eds.), NACE, Houston, TX, 1969, pp. 214–96.
- [50] T. Murata, E. Sato, H. Okada, Passivity and Its Breakdown on Iron and Iron Base Alloys, ed. H. Okada and R. W. Staehle, NACE (1976) 186-189.
- [51] R. W. Staehle, J. J. Royvela, T. L. Raredon, E. Serrate, C. R. Morin, R. V. Farrar, Corrosion, 26 (1970) 451.
- [52] Y. H. Jang, S. S. Kim, J. H. Lee, Effect of Different Mn Contents on Tensile and Corrosion Behavior of CD4MCU Cast Duplex Stainless Steels, Mater. Sci. Eng. A 396 (2005) 302-310. <https://doi.org/10.1016/j.msea.2005.01.046>.
- [53] D. Kopeliovich, Pitting Corrosion.
http://www.substech.com/dokuwiki/doku.php?id=pitting_corrosion, 2015 (accessed 6 September 2015).
- [54] R. W. Revie, H. H. Uhlig, Corrosion and Corrosion Control: An Introduction to Corrosion Science and Engineering, Wiley-Interscience, Hoboken, New Jersey, 2008.
- [55] G. S. Frankel, Pitting Corrosion, Corrosion: Fundamentals, Testing and Protection, ASM International, 13A, ASM Handbook: p.236-241, 2003.
- [56] D. A. Jones, Principles and Prevention of Corrosion, Prentice Hall, Upper Saddle River, New Jersey, 1996.

- [57] S. D. Cramer, B. S. Covino, ASM International, ASM Handbook, Corrosion, 13A, Materials Park, Ohio, 2003.
- [58] A. U. Malik, P. C. Mayan Kutty, N. A. Siddiqi, I. N. Andijani, S. Ahmed, The Influence of pH and Chloride Concentration on the Corrosion Behavior of AISI316L Steel in Aqueous Solutions, *Corros. Sci.* 33 (1992) 1809-1827. [https://doi.org/10.1016/0010-938X\(92\)90011-Q](https://doi.org/10.1016/0010-938X(92)90011-Q).
- [59] M. G. Fontana, *Corrosion Engineering*, 3rd ed., Tata McGraw-Hill Education, Singapore, 1986.
- [60] K. Sieradzki, R. C. C. Newman, Stress-Corrosion Cracking, *J. Phys. Chem. Solids.* 48 (1987) 1101-1113. [https://doi.org/10.1016/0022-3697\(87\)90120-X](https://doi.org/10.1016/0022-3697(87)90120-X).
- [61] B. F. Brown, *Stress Corrosion Cracking Control Measures*, First, U.S. Government Printing Office, Washington, 1977.
- [62] P. A. Schweitzer, *Fundamentals of Metallic Corrosion: Atmospheric and Media Corrosion of Metals*, CRC Press, 2006.
- [63] R. C. Newman, R. P. M. Procter, Stress Corrosion Cracking: 1965-1990, *Br. Corros.* 25 (1990) 259-270. <https://doi.org/10.1179/000705990799156373>.
- [64] R. Merello, F. J. Botana, J. Botella, M. V. Matres, M. Marcos, Influence of Chemical Composition on the Pitting Corrosion Resistance of Non-standard Low-Ni High-Mn-N Duplex Stainless Steels, *Corros. Sci.* 45 (2003) 909-921. [https://doi.org/10.1016/S0010-938X\(02\)00154-3](https://doi.org/10.1016/S0010-938X(02)00154-3).
- [65] M. E. Naess, R. Birkeland, M. Iannuzzi, R. Johnsen, Use of Electrochemical Techniques to Determine the Effect of Sigma (σ)-phase Precipitation on A 25 wt% Cr Super Duplex Stainless Steel, *Corrosion 2015*, NACE International, 2015.

- [66] A. G. Hartline, The Effect of Nitrogen Additions Upon the Pitting Resistance of 18 pct Cr, 18 pct Mn Stainless Steel, *Metall. Trans.* 5 (1974) 2271-2276.
<https://doi.org/10.1007/BF02644006>.
- [67] S. Lozano-Perez, J. Dohr, M. Meisnar, K. Kruska, SCC in PWRs: Learning from a Bottom-Up Approach, *Metall. Mater. Trans. E.* 1 (2014) 194-210. <https://doi.org/10.1007/s40553-014-0020-y>.
- [68] D. T. Spencer, M. R. Edwards, M. R. Wenman, C. Tsitsios, G. G. Scatigno, P. R. Chard-Tuckey, The Initiation and Propagation of Chloride-Induced Transgranular Stress-Corrosion Cracking (TGSCC) of 304L Austenitic Stainless Steel Under Atmospheric Conditions, *Corros. Sci.* 88 (2014) 76-88. <https://doi.org/10.1016/j.corsci.2014.07.017>.
- [69] G. G. Scatigno, M. P. Ryan, F. Giuliani, M. R. Wenman, The Effect of Prior Cold Work on the Chloride Stress Corrosion Cracking of 304L Austenitic Stainless Steel Under Atmospheric Conditions, *Mater. Sci. Eng. A* 668 (2016) 20-29.
<https://doi.org/10.1016/j.msea.2016.05.037>.
- [70] P. L. Andresen, F. Peter Ford, P. F. Ford, F. Peter Ford, P. F. Ford, Life Prediction by Mechanistic Modeling and System Monitoring of Environmental Cracking of Iron and Nickel Alloys in Aqueous Systems, *Work. Mech. Phys. Crack Growth Appl. to Life Predict.* 103 (1988) 167-184. [https://doi.org/10.1016/0025-5416\(88\)90564-2](https://doi.org/10.1016/0025-5416(88)90564-2).
- [71] T. Shoji, Z. Lu, H. Murakami, Formulating Stress Corrosion Cracking Growth Rates by Combination of Crack Tip Mechanics and Crack Tip Oxidation Kinetics, *Corros. Sci.* 52 (2010) 769-779. <https://doi.org/10.1016/j.corsci.2009.10.041>.
- [72] P. Marcus, *Corrosion Mechanisms in Theory and Practice*, 2nd ed., Marcel Dekker, New York, 2002.

- [73] A. J. Sedriks, Corrosion Testing Made Easy: Stress Corrosion Cracking Test Methods, NACE, Houston, TX, 1990, p.87.
- [74] X. C. Jiang, R. W. Staehle, Effects of Stress and Temperature on Stress Corrosion Cracking of Austenitic Stainless Steels in Concentrated Magnesium Chloride Solutions, Corrosion, 53 (1997) 448-466.
- [75] P. Pederferri, Stress Corrosion Cracking and Corrosion-Fatigue, Corrosion Science and Engineering, Engineering Materials, Springer, p243-273, 2018.
- [76] R. W. Hertzberg, Deformation and Fracture Mechanics of Engineering Materials, 4th ed., John Wiley & Sons Inc, Tallahassee, Florida, 1995.
- [77] D. T. Spencer, The Initiation and Propagation of Chloride-Induced Transgranular Stress Corrosion Cracking of Austenitic Stainless Steel PWR Pipework under Atmospheric Conditions, 184, 2012.
- [78] H. H. Uhlig, E. W. Cook Jr., Mechanism of Inhibiting Stress Corrosion Cracking of 18-8 Stainless Steel in MgCl₂ by Acetates and Nitrates, J. Electrochem. Soc. 116 (1969) 173-177.
<https://doi.org/10.1149/1.2411789>.
- [79] R. W. Staehle, Lifetime Prediction of Materials in Environments, in: R. W. Revie (Ed.), Uhlig's Corrosion Handbook, John Wiley & Sons Inc, 2011, pp.31-74.
- [80] M. Behzad, A. Meghdari, A. Ebrahimi, A Linear Theory for Bending Stress-Strain Analysis of A Beam with An Edge Crack, Eng. Frac. Mech. 75 (2008) 4695-4705.
<https://doi.org/10.1016/j.engfracmech.2008.06.028>.
- [81] A. P. Jivkov, T. J. Marrow, Rates of Intergranular Environment Assisted Cracking in Three-Dimensional Model Microstructures, Theor. Appl. Frac. Mech. 48 (2007) 187-202.
<https://doi.org/10.1016/j.tafmec.2007.08.007>.

- [82] J. Tani, M. Mayuzumi, N. Hara, Stress Corrosion Cracking of Stainless-Steel Canister for Concrete Cask Storage of Spent Fuel, *J. Nucl. Mater.* 379 (2008) 42-47.
<https://doi.org/10.1016/j.jnucmat.2008.06.005>.
- [83] S. D. Cramer, B. S. Covino, *Corrosion: Fundamentals, Testing and Protection*, ASM International, 2003.
- [84] J. Clark, The Effect of Temperature on Rate of Reaction.
[https://chem.libretexts.org/Bookshelves/Physical_and_Theoretical_Chemistry_Textbook_Maps/Supplemental_Modules_\(Physical_and_Theoretical_Chemistry\)/Kinetics/Rate_Laws/Reaction_Mechanisms/Reaction_Mechanisms/The_Effect_of_Temperature_on_Rate_of_Reaction](https://chem.libretexts.org/Bookshelves/Physical_and_Theoretical_Chemistry_Textbook_Maps/Supplemental_Modules_(Physical_and_Theoretical_Chemistry)/Kinetics/Rate_Laws/Reaction_Mechanisms/Reaction_Mechanisms/The_Effect_of_Temperature_on_Rate_of_Reaction), 2019 (accessed Sep 10, 2019).
- [85] K. van Gelder, J. G. Erlings, J. W. M. Damen, A. Visser, The Stress Corrosion Cracking of Duplex Stainless Steel in H₂S/CO₂/Cl⁻ Environments, *Corros. Sci.* 27 (1987) 1271-1279.
[https://doi.org/10.1016/0010-938X\(87\)90114-4](https://doi.org/10.1016/0010-938X(87)90114-4).
- [86] J. R. Saithala, J. D. Atkinson, Stress Corrosion Behavior of Super Duplex Stainless Steel in Dilute Chloride Solution at 130 °C. Material Engineering Research Institute Sheffield Hallam University. Duplex 2007 International Conference and Expo, Grado, Italy, 18-20 June 2007.
- [87] J. R. Saithala, S. McCoy, A. Houghton, J. D. Atkinson, H. S. Ubhi, Stress Corrosion Cracking of Super Duplex Stainless Steels Above and Below the Pitting Potential, *Corrosion* (2009), NACE International, Atlanta, GA.
- [88] O. M. Alyousif, R. Nishimura, The Stress Corrosion Cracking Behavior of Austenitic Stainless Steels in Boiling Magnesium Chloride Solution, *Corros. Sci.* 49 (2007) 3040-3051.
<https://doi.org/10.1016/j.corsci.2006.12.023>.

- [89] R.K.S. Raman, S. Pal, A Simple Approach to the Determination of Threshold Stress Intensity for Stress Corrosion Cracking (K_{ISCC}) and Crack Growth of Sensitized Austenitic Stainless Steel, *Metall. Mater. Trans.* 42A (2011) 2643-2651.
<https://doi.org/10.1007/s11661-011-0704-1>.
- [90] A. J. Russell, D. Tromans, A Fracture Mechanics Study of Stress Corrosion Cracking of Type-316 Austenitic Steel, *Metall. Trans.* 10A (1979) 1229-1238.
<https://doi.org/10.1007/BF02811978>.
- [91] H. Hawkes, F. Beck, M. Fontana, Effect of Applied Stress and Cold Work On Stress Corrosion Cracking of Austenitic Stainless Steel by Boiling 42 Percent Magnesium Chloride, *Corrosion* 19 (1963) 247-253. <https://doi.org/10.5006/0010-9312-19.7.247>.
- [92] T. Nakayama, M. Takano, Application of A Slip Dissolution-Repassivation Model for Stress Corrosion Cracking of AISI 304 Stainless Steel in Boiling 42% $MgCl_2$ Solution, *Corrosion* 42 (1986) 10-15. <https://doi.org/10.5006/1.3584873>.
- [93] H. Shaikh, H. Khatak, P. Rodriguez, Stress Corrosion Crack Growth Behavior of Austenitic Stainless Steels in Hot Concentrated Chloride Solution, *ICF* 10 (2001).
- [94] H.S. Khatak, J.B. Gnanamoorthy, P. Rodriguez, Studies on the Influence of Metallurgical Variables on the Stress Corrosion Behavior of AISI 304 Stainless Steel in Sodium Chloride Solution Using the Fracture Mechanics Approach, *Metall. Mater. Trans.* 27A (1996) 1313-1325. <https://doi.org/10.1007/BF02649868>.
- [95] M.O. Speidel, Stress Corrosion Cracking of Stainless Steels in NaCl Solutions, *Metall. Trans.* 12A (1981) 779-789. <https://doi.org/10.1007/BF02648342>.
- [96] P. R. Rhodes, Mechanism of Chloride Stress Corrosion Cracking of Austenitic Stainless Steels, *Corrosion* 25 (1969) 462-472. <https://doi.org/10.5006/0010-9312-25.11.462>.

- [97] S. W. Dean, Stress Corrosion – New Approaches, ASTM STP 610, ed. H. L. Craig, ASTM, (1976) 308.
- [98] L. G. Mallinson, Ageing Studies and Lifetime Extension of Materials, 1st ed., Springer Science + Business Media LLC, New York, 2001, pp. 560.
- [99] W. L. Clarke, G. M. Gordon, Investigation of Stress Corrosion Cracking Susceptibility of Fe-Ni-Cr Alloys in Nuclear Reactor Water Environments, Corrosion 29 (1973) 1-12.
<https://doi.org/10.5006/0010-9312-29.1.1>.
- [100] C. T. Ward, D. L. Mathis, R. W. Staehle, Intergranular Attack of Sensitized Austenitic Stainless Steel by Water Containing Fluoride Ions, Corrosion 25 (1969) 394-396.
<https://doi.org/10.5006/0010-9312-25.9.394>.
- [101] G. J. Theus, J. R. Cels, Babcock and Wilcox Report RDTPA – 74-16 (1974).
- [102] D. Talbot, J. Talbot, Corrosion Science and Technology, CRC Press, Boca Raton, 1998.
- [103] G. Rondelli, B. Vincentini, E. Sivieri, Stress Corrosion Cracking of Stainless Steel in High Temperature Caustic Solutions, Corros. Sci. 39 (1997) 1037-1049.
[https://doi.org/10.1016/S0010-938X\(97\)88507-1](https://doi.org/10.1016/S0010-938X(97)88507-1).
- [104] G. Rondelli, B. Vincentini, Susceptibility of Highly Alloyed Austenitic Stainless Steels to Caustic Stress Corrosion Cracking, Materials and Corrosion 53 (2002) 813-819.
[https://doi.org/10.1002/1521-4176\(200211\)53:113.0.CO;2-D](https://doi.org/10.1002/1521-4176(200211)53:113.0.CO;2-D).
- [105] P. M. Singh, O. Ige, J. Mahmood, Stress Corrosion Cracking of Type 304L Stainless Steel in Sodium Sulfide-Containing Caustic Solutions, Corrosion 59 (2003) 843-850.
<https://doi.org/10.5006/1.3287704>.

- [106] D. L. Singbeil, A. Garner, Electrochemical and Stress Corrosion Cracking Behavior of Digester Steels in Kraft White Liquors, NACE Corrosion 84, New Orleans, LA, USA, April 2-6, 1984.
- [107] M.O. Speidel, Draft Chapters: Stress Corrosion Cracking of Austenitic Stainless Steels, ARPA Handbook on Stress Corrosion Cracking (1977).
- [108] L. Peterman, R. A. Yeske, Thiosulfate Effects on Corrosion in Kraft White Liquor, IPC Technical Paper Series 205, Appleton, WI, Georgia Institute of Technology, (1986).
- [109] D. A. Wensley, R. S. Charlton, Corrosion Studies in Kraft White Liquor: Potentiostatic Polarization of Mild Steel in Caustic Solutions Containing Sulfur Species, Corrosion 36, (1980) 385-389. <https://doi.org/10.5006/0010-9312-36.8.385>.
- [110] M. R. Louthan, Initial Stages of Stress Corrosion Cracking In Austenitic Stainless Steels, Corrosion 21 (1965) 288-294. <https://doi.org/10.5006/0010-9312-21.9.288>.
- [111] E. McCafferty, Thermodynamics of Corrosion: Pourbaix Diagrams, in: Introduction to Corrosion Science, Springer, New York, 2010.
- [112] LibreTexts, Pourbaix Diagrams.
[https://chem.libretexts.org/Bookshelves/Inorganic_Chemistry/Book%3A_Inorganic_Chemistry_\(Wikibook\)/Chapter_04%3A_Redox_Stability_and_Redox_Reactions/4.5%3A_Pourbaix_diagrams](https://chem.libretexts.org/Bookshelves/Inorganic_Chemistry/Book%3A_Inorganic_Chemistry_(Wikibook)/Chapter_04%3A_Redox_Stability_and_Redox_Reactions/4.5%3A_Pourbaix_diagrams), 2019 (accessed Sep 12, 2019).
- [113] T. Suzuki, M. Yamaha, Y. Kitamura, Composition of Anolyte Within Pit Anode of Austenitic Stainless Steels in Chloride Solution, Corrosion 29 (1973) 18-22.
<https://doi.org/10.5006/0010-9312-29.1.18>.

- [114] H. R. Baker, M. C. Bloom, R. N. Bolster, C. R. Singleterry, Film and pH Effects in the Stress Corrosion Cracking of Type 304 Stainless Steel, *Corrosion* 26 (1970) 420-426. <https://doi.org/10.5006/0010-9312-26.10.420>.
- [115] G. Sandoz, C. T. Fujii, B. F. Brown, Solution Chemistry Within Stress-Corrosion Cracks in Alloy Steels, *Corros. Sci.* 10 (1970) 839-845. [https://doi.org/10.1016/S0010-938X\(70\)80102-0](https://doi.org/10.1016/S0010-938X(70)80102-0).
- [116] B. E. Wilde, The Role of Passivity in the Mechanism of Stress-Corrosion Cracking and Metal Dissolution of 18Cr-8Ni Stainless Steels in Boiling Magnesium and Lithium Chlorides, *J. Electrochem. Soc.* 118 (1971) 1717-1725. <https://doi.org/10.1149/1.2407824>.
- [117] E. C. Bain, R. H. Aborn, J. J. B. Rutherford, The Nature and Prevention of Intergranular Corrosion in Austenitic Stainless Steels, *Trans. Amer. Soc. Steel Treating* 21 (1933) 481-509.
- [118] C. Stawstrom, M. Hillert, An Improved Depleted-zone Theory of Intergranular Corrosion of 18-8 Stainless Steel, *JISI* 207 (1969) 77-85.
- [119] C. D. Tedmon, D. A. Vermilyea, J. H. Rosolowski, Intergranular Corrosion of Austenitic Stainless Steel, *J. Electrochem. Soc.* 118 (1971) 192-202. <https://doi.org/10.1149/1.2407966>.
- [120] F. A. Champion, Symposium on Internal Stresses in Metals and Alloys, Institute of Metals, London, 1948, p.468.
- [121] R. W. Staehle, The Theory of Stress Corrosion Cracking in Alloys, in: J. C. Scully (Ed.), NATO, Brussels, 1971, pp.493.
- [122] D. A. Vermilyea, A Theory for the Propagation of Stress Corrosion Cracks in Metals, *J. Electrochem. Soc.* 119 (1972) 405-407. <https://doi.org/10.1149/1.2404217>.

- [123] D. A. Vermilyea, Stress Corrosion Cracking of Iron and Nickel Base Alloys in Sulfate Solutions at 289 C, *Corrosion* 29 (1973) 442-450. <https://doi.org/10.5006/0010-9312-29.11.442>.
- [124] Z. Li, Y. Lu, X. Wang, Modeling of Stress Corrosion Cracking Growth Rates for Key Structural Materials of Nuclear Power Plant, *J. Mater. Sci.* 55 (2020) 439-463. <https://doi.org/10.1007/s10853-019-03968-w>.
- [125] J. C. Scully, Environment Sensitive Cracking of Materials, in: P. R. Swann, F. P. Ford, A. R. C. Westwood (Eds.), *The Metals Society, London*, 1977, pp. 7.
- [126] J. M. Silcock, P. R. Swann, Mechanisms of Environment Sensitive Cracking of Materials, in: P. R. Swann, F. P. Ford, A. R. C. Westwood (Eds.), *The Metals Society, London*, 1977, pp. 66.
- [127] J. M. Silcock, P. R. Swann, Environment-Sensitive Fracture of Engineering Materials, in: Z. A. Foroulis (Ed.), *Nucleation and Growth of Transgranular Stress Corrosion Cracks in Austenitic Stainless Steels*, AIME, Chicago, IL, 1979, pp. 133-152.
- [128] P. Doig, P. E. J. Flewitt, An Electrochemical Model for Intergranular Stress Corrosion Cracking in Iron-Nickel Alloys, CEGB Report SSD/SE/R38/77 (1977).
- [129] P. Doig, P. E. J. Flewitt, The Electrode Potential Within a Growing Stress Corrosion Crack, *Proc. Roy. Soc. A* 357 (1977) 439-452. <https://doi.org/10.1098/rspa.1977.0178>.
- [130] F. P. Ford, M. Silverman, Mechanisms of Environmentally Enhanced Cracking in Alloy/Environment Systems Peculiar to Power Generation Industries, Contract No. RP 1332-1, First Semi-Annual Report, General Electric Research Center (1979).

- [131] F. P. Ford, M. J. Povich, The Effect of Oxygen/Temperature Combinations on the Stress Corrosion Susceptibility of Sensitised 304 Stainless Steel in High-Purity Water, NACE Corrosion 79, Atlanta, GA 12-16 March 1979, 94.
- [132] F. P. Ford, M. J. Povich, The Effect of Oxygen Temperature Combinations on the Stress Corrosion Susceptibility of Sensitized Type 304 Stainless Steel in High Purity Water, Corrosion 35 (1979) 569-574. <https://doi.org/10.5006/0010-9312-35.12.569>.
- [133] F. P. Ford, The Crack-Tip System and Its Relevance to the Prediction of Cracking in Aqueous Environments, NACE 10, EICM Proceedings, pp. 139-165.
- [134] N. A. Nielsen, J. Materials 5 (1970) 749.
- [135] P. R. Swann, J. D. Embury, High Strength Materials, in: V. Zackay (Ed.), John Wiley and Sons, 1965, pp. 327.
- [136] E. N. Pugh, A Post Conference Evaluation of Our Understanding of the Failure Mechanisms, in: R. W. Staehle et al. (Eds.), Stress Corrosion Cracking and Hydrogen Embrittlement of Iron Base Alloys, NACE 5, Houston, TX (1977) pp. 37-51.
- [137] Z. Szklarska-Smialowska, Various Forms of Localized Corrosion Common Features and Differences, NACE 5 (1977) 30-36.
- [138] C. F. Barth, A. R. Troiano, Cathodic Protection and Hydrogen in Stress Corrosion Cracking, Corrosion 28 (1972) 259-263. <https://doi.org/10.5006/0010-9312-28.7.259>.
- [139] C. L. Briant, Hydrogen Assisted Cracking of Sensitized 304 Stainless Steel, Met. Trans. 9A (1978) 731-733. <https://doi.org/10.1007/BF02659931>.
- [140] P. P. Milella, Hydrogen Embrittlement and Sensitization Cracking, in: Fatigue and Corrosion in Metals, Springer, Milan, 2013, pp. 689-730.

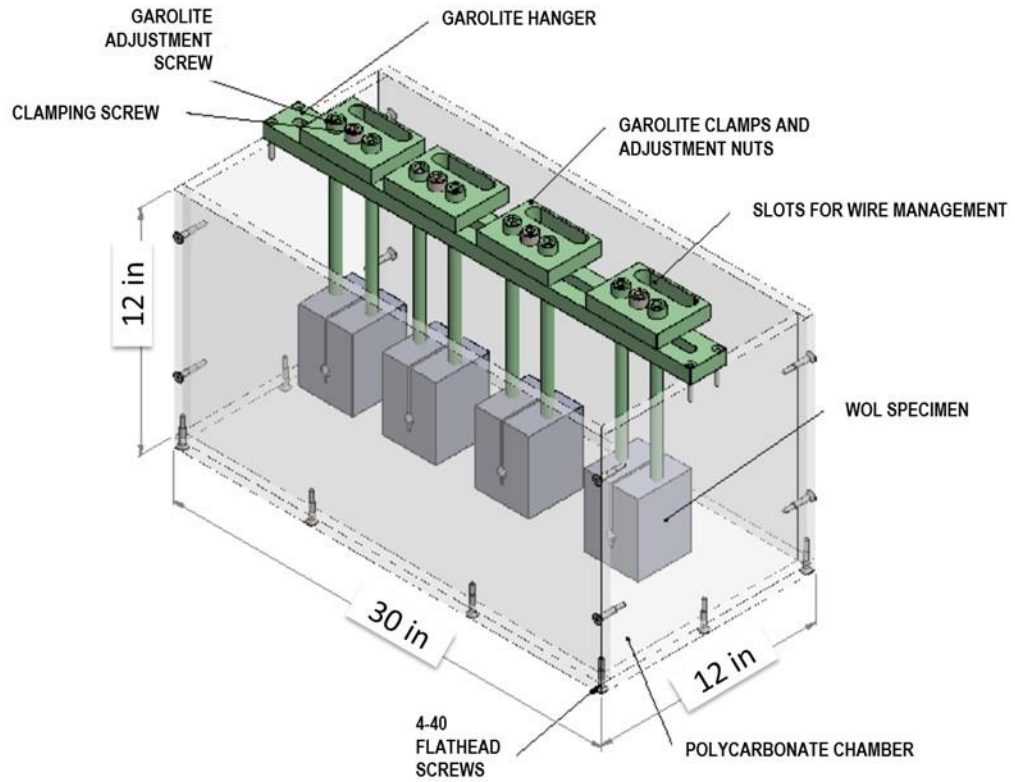
- [141] A. Szummer, A. Janko, Hydride Phases in Austenitic Stainless Steels, *Corrosion* 35 (1979) 461-464. <https://doi.org/10.5006/0010-9312-35.10.461>.
- [142] K. Kamachi, M. Oka, M. Touge, Proc, 1st Int'l Symp. on New Aspects of Martensitic Transformation: *Trans JIM* 17 (1976) 309.
- [143] H. Mathias, Y. Katz, S. Nativ, 3rd Int'l Conf. on Effects of Hydrogen on the Behavior of Materials: Jackson Lake Lodge (1980).
- [144] S. S. Birley, D. Tromans, Stress Corrosion Cracking of 304L Austenitic Steel and the Martensite Transformation, *Corrosion* 27 (1971) 63-71. <https://doi.org/10.5006/0010-9312-27.2.63>.
- [145] D. A. Vaughan, D. I. Phalen, C. L. Peterson, W. K. Boyd, Relationship Between Hydrogen Pickup And Susceptible Paths in Stress Corrosion Cracking Of Type 304 Stainless Steel, *Corrosion* 19 (1963) 315t-326t. <https://doi.org/10.5006/0010-9312-19.9.315>.
- [146] L. H. Keys, A. J. Bursle, H. R. Kemp, K. R. L. Thompson, 2nd Int'l Congr. On Hydrogen in Metals, Int'l. Assoc. for Hydrogen Energy (1977) 3f6.
- [147] T. Magnin, A. Chambreuil, B. Bayle, The Corrosion-Enhanced Plasticity Model for Stress Corrosion Cracking in Ductile FCC Alloys, *Acta Mater.* 44 (1996) 1457-1470. [https://doi.org/10.1016/1359-6454\(95\)00301-0](https://doi.org/10.1016/1359-6454(95)00301-0).
- [148] J. P. Chateau-Cornu, D. Delafosse, T. Magnin, Numerical Simulations of Hydrogen-Dislocation Interactions in FCC Stainless Steels. Part I: Hydrogen-Dislocation Interactions in Bulk Crystals, *Acta Mater.* 50 (2002) 1507-1522. [https://doi.org/10.1016/S1359-6454\(02\)00008-3](https://doi.org/10.1016/S1359-6454(02)00008-3).
- [149] A. N. Stroh, Dislocations and Cracks in Anisotropic Elasticity, *Philos. Mag.* 3 (1958) 625-646. <https://doi.org/10.1080/14786435808565804>.

- [150] A. N. Stroh, A Theory of the Fracture of Metals, *Adv. Phys.* 6 (1957) 418-465.
<https://doi.org/10.1080/00018735700101406>.
- [151] H. B. Pereira, Z. Panossian, I. P. Baptista, C. R. de Farias Azevedo, Investigation of Stress Corrosion Cracking of Austenitic, Duplex and Super Duplex Stainless Steels under Drop Evaporation Test using Synthetic Seawater, *Mat. Res.* 22 (2019).
<https://doi.org/10.1590/1980-5373-mr-2018-0211>.
- [152] C. Edeleanu, *JISI* 173 (1953) 140.
- [153] H. Kamide, H. Sugawara, Effect of Prestrain on Stress Corrosion Cracking of Type 304 Stainless Steel by Means of the Stress Relaxation Method, *Corrosion* 35 (1979) 456-460.
<https://doi.org/10.5006/0010-9312-35.10.456>.
- [154] H. E. Hanninen, *Proc. 7th Int'l. Congr. On Metallic Corrosion – Oct. 1978, Rio de Janeiro (ABRACO, 1979)* 751.
- [155] H. Hanninen, T. Hakkarainen, P. Nenonen, 3rd Int'l Conf. on Effects of Hydrogen on the Behavior of Materials: Jackson Lake Lodge (1980).
- [156] C. Paes de Oliveira, M. Aucouturier, P. Lacombe, Hydrogen Trapping in BCC Fe-Cr Alloys (7 ~ 9.4 Wt% Cr) as Studied by Microautoradiography—Contribution of Carbon-Hydrogen Interaction—Consequences on Hydrogen Cracking, *Corrosion* 36 (1980) 53-59.
<https://doi.org/10.5006/0010-9312-36.2.53>.
- [157] E. Turkoz, What is Stress Intensity Factor? What Are the Loading/Fracture Modes?
<https://www.princeton.edu/~eturkoz/materials.html#> (accessed 16 November 2015).
- [158] T. L. Anderson, *Fracture Mechanics: Fundamentals and Applications*, 3rd ed., CRC Press/Taylor & Francis, Boca Raton, 2005.

CHAPTER 3: MATERIALS AND EXPERIMENTAL METHODS

3.1. Corrosion chamber

To investigate SCC behavior of SS304 and SS304L which have been used for fabricating dry storage canisters, a corrosion chamber was built at North Carolina State University. A CAD drawing of the corrosion chamber is included in Figure 3.1a and the photograph of the actual chamber is shown in Figure 3.1b. The length, width, and depth of the chamber are 762 mm x 305 mm x 305 mm (30 in. x 12 in. x 12 in.), respectively. The size of the chamber is sufficient to conduct SCC experiments of up to four specimens simultaneously. This feature will come in handy when evaluating many specimens either in different conditions or for measuring scatter in data points under the same condition. The sides and bottom of the chamber were fabricated from polycarbonate and the internal edges of the chamber were sealed using a marine grade silicone-based sealant. For suspending samples inside the chamber, a hanger was built with its ends resting on the top portion of the sides of the chamber opposite to each other. The hanger is equipped with four clamps with provisions for suspending samples in the marine solutions and also managing input/output signal wires from/to the samples. Both the hanger and clamps are made of Garolite (also known as Phenolic), a polymer matrix composite made of glass fibers impregnated with epoxy resins. It is a very strong, stiff, electrically non-conducting, and highly corrosion resistant material.



(a)



(b)

Figure 3.1. (a) A CAD model showing the design of the corrosion chamber and (b) a photograph of the corrosion chamber built.

3.2. Wedge opening loading specimen

In the study of SCC using fracture mechanics-based approach, a wide variety of specimens are used. Compact tension, single edge bend, and disk-shaped compact specimens are some specimen geometries most commonly used in the evaluation of fracture toughness. ASTM standard E399–12 can be referred to for further details on these specimens [1]. Wedge opening loading (WOL) specimen was developed in response to very large sample size requirement for conventional specimens for evaluating K_{IC} of medium to low strength metallic materials [2].

The WOL specimen geometry and related dimensions are shown in Fig. 3.2. A combination of CNC and electro-discharge machining (EDM) techniques were used for specimen preparation. While the notch of the WOL specimen was prepared using EDM, the rest was made using CNC machining. The WOL specimen will be loaded using an instrumented bolt which goes inside the specimen through the tapped hole labeled as 1 and impinges on the flat portion on a pin inserted through the hole labeled 2 in Fig. 3.2. The drawing of the pin is shown in Fig. 3.3. The WOL and pin are made of SS304 H – the material sent by CSM.

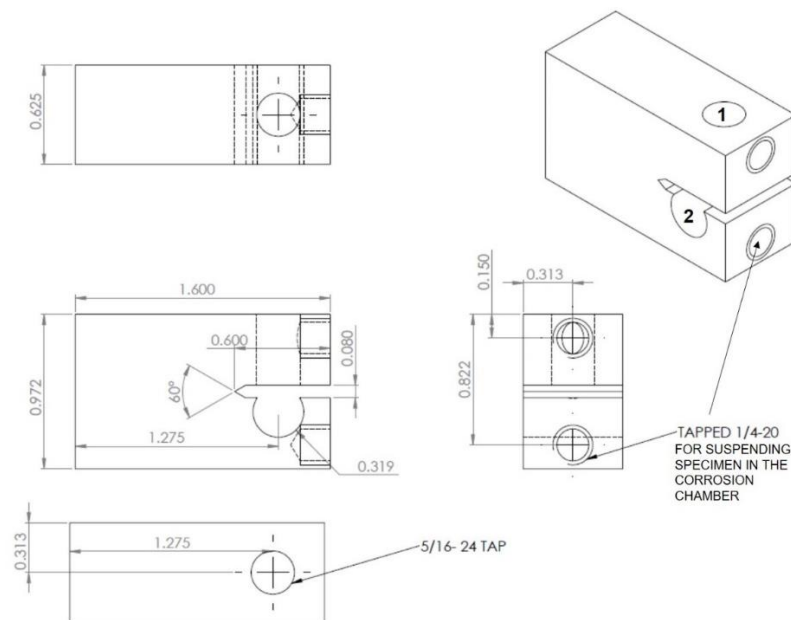


Figure 3.2. 2-D and 3-D drawing showing WOL specimen geometry and dimensions.

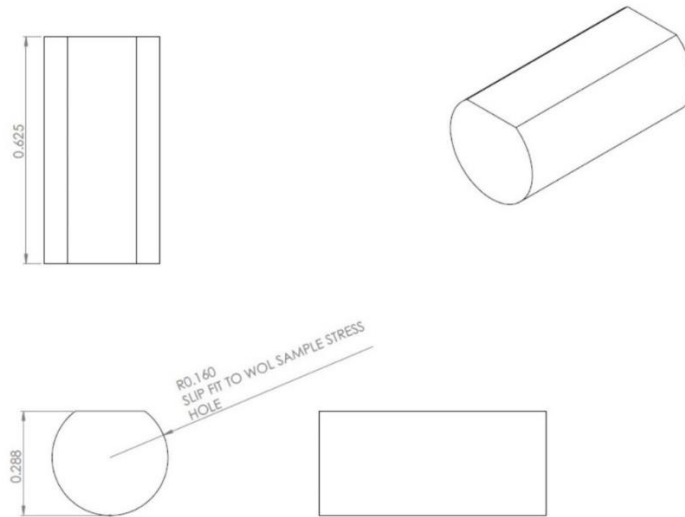


Figure 3.3. Pin made of SS 304H for assisting in loading of WOL specimen using instrumented bolt.

A photograph of the WOL specimen is shown in Fig. 3.4a along with the pin for which the drawing is shown in Fig. 3.3. A close-up view of notched region of the WOL specimen at two different magnifications are shown in Fig. 3.4b and 3.4c. In this case, the notch root radius was measured and was found to be equal to $\sim 193 \mu\text{m}$ (Fig. 3.4c).

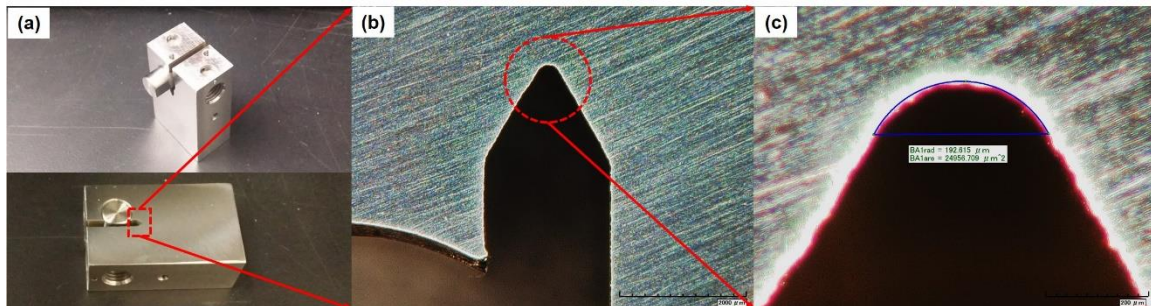


Figure 3.4. (a) Different views of WOL samples prepared from SS 304-H alloy supplied by Colorado School of Mines, Golden, (b) Optical macrograph showing tip region of the WOL specimen, and (c) A magnified view of the notch tip depicting the shape of the tip for measuring the radius of the tip (radius = $\sim 193 \mu\text{m}$).

3.3. Instrumented bolt for loading WOL specimen

For loading WOL specimen to a desired level, an instrumented bolt will be used. A photo of the instrumented bolt (procured from Strainsert company) is included in Fig. 3.5 and it is made of 17-4 PH stainless steel designed to be good to compressive loads to 2400 lb. The calibration of the bolt was carried out by the manufacturer and the calibration values are included in Table 3.1 which exhibit linear behavior (Fig. 3.6).



Figure 3.5. A drawing of instrumented bolt designed by Strainsert company.

Table 3.1. Strainsert Calibration Chart.

Test Load (lbf)	Test Load (N)	Signal (mV/V)
0	0	0
480	2135.15	0.515
960	4270.29	1.029
1440	6405.44	1.544
1920	8540.59	2.058
2400	10675.73	2.573

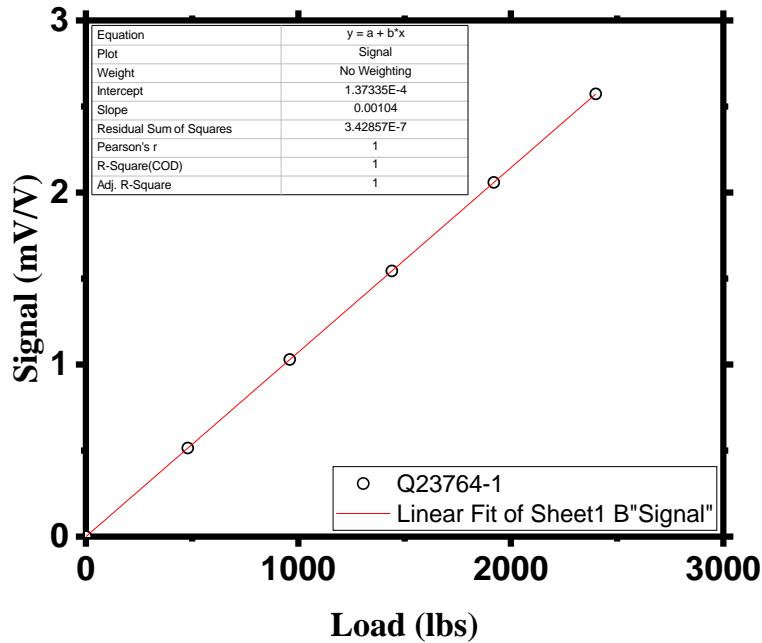


Figure 3.6. Instrumented bolt straight-line signal as a function of test load.

3.4. Fatigue pre-cracking

A 2D CAD drawing model of the wedge opening loading (WOL) SS304 specimens used in the project along with dimensions in inches is shown in Fig. 3.7a. Note that the dimensions of the actual WOL specimen differed from the original dimensions shown in Fig. 3.2 to accommodate instrumented bolt load to develop sufficient level of stress intensity. An actual machined WOL specimen is shown in Fig. 3.7b with the radius of the notch ranging from 150-250 μm where the variation of the notch radius comes from the uncertainty in the fabrication of the WOL specimens. The WOL specimens were fatigue pre-cracked using a fatigue machine from Test Resources model 910LX15 as shown in Fig. 3.8 to produce the desirable sharpness. A fatigue pre-crack in a WOL specimen is shown in Fig. 3.9.

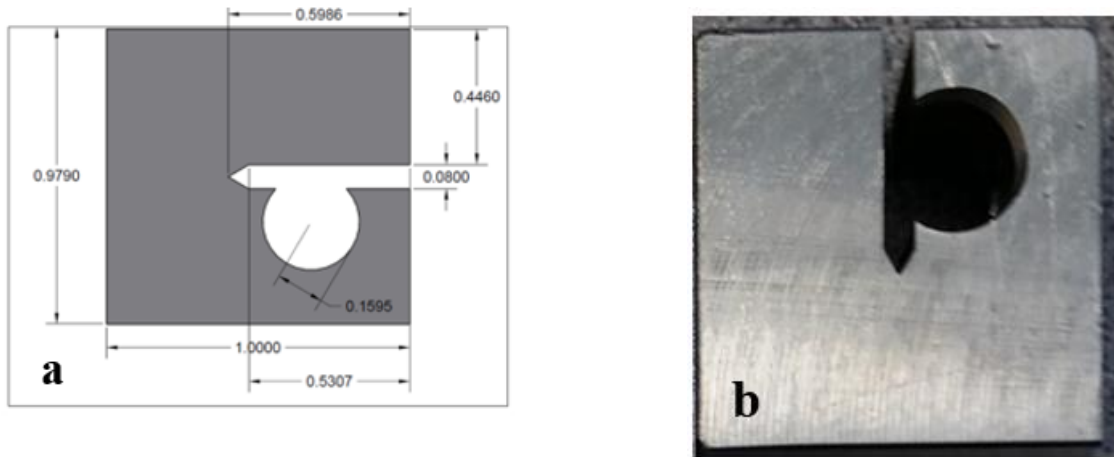


Figure 3.7. (a) Dimensions of WOL specimen in inches and (b) a WOL specimen.

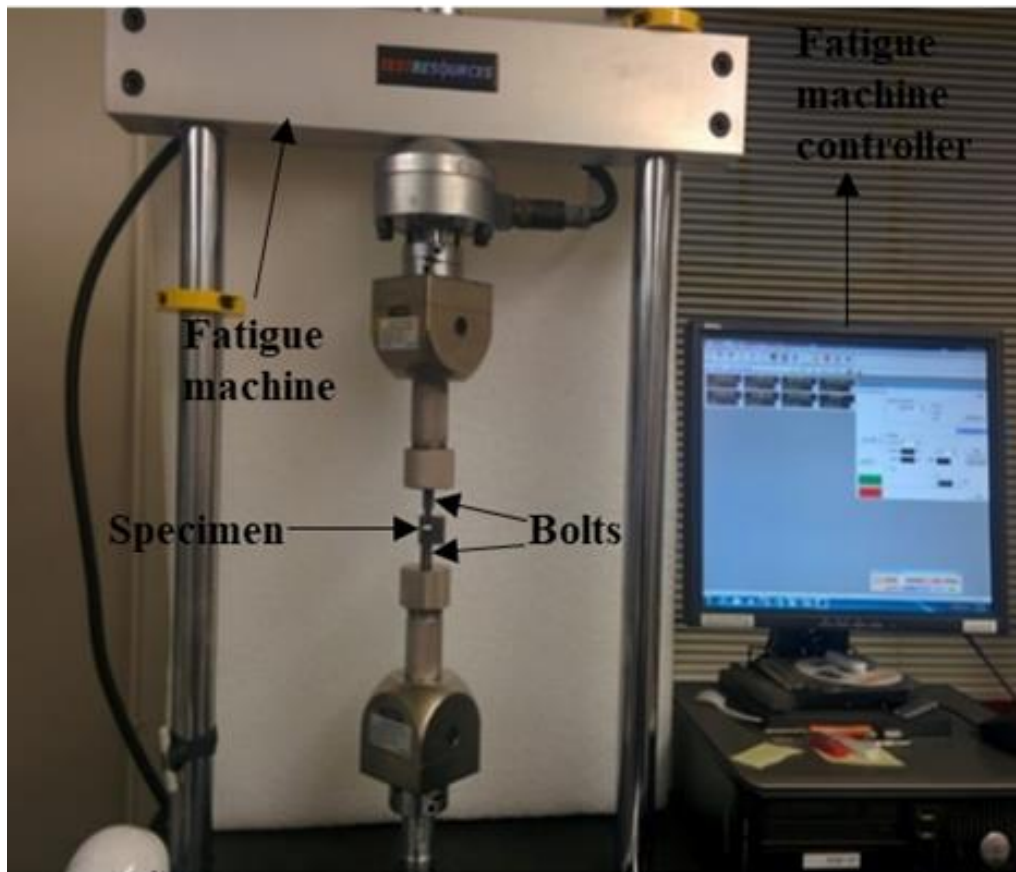


Figure 3.8. Fatigue pre-crack experimental setup.

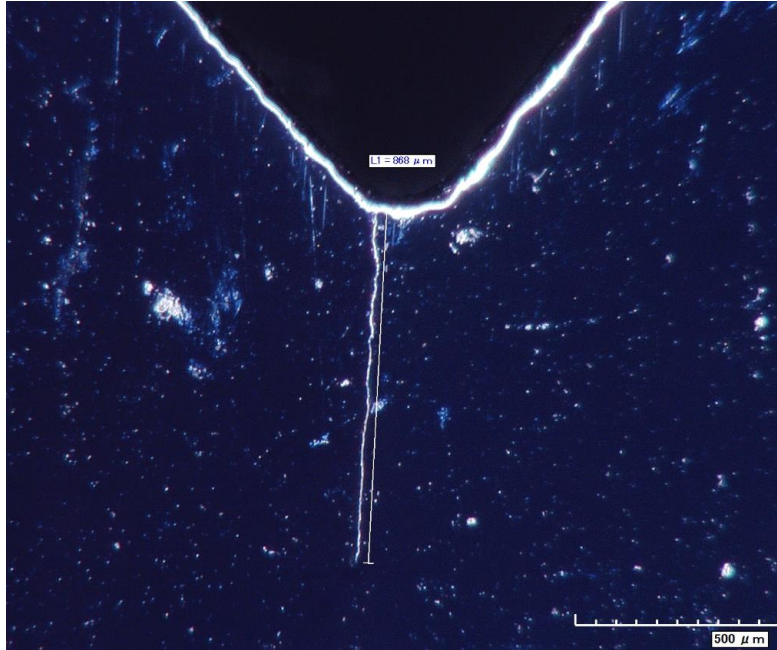


Figure 3.9. A fatigue pre-cracked WOL specimen.

The fatigue pre-crack experiments followed ASTM E399-12 [1], E1820-15 [3] and E1681-03 [4] where the WOL specimen was treated as a compact tension (CT) specimen and the stress intensity factor was calculated from the ASTM E399-12 [1],

$$K_Q = \frac{P_Q}{\sqrt{B B_N \sqrt{W}}} f\left(\frac{a}{W}\right) \quad (3.1)$$

$$f\left(\frac{a}{W}\right) = \frac{\left(2 + \frac{a}{W}\right) \left[0.886 + 4.64 \frac{a}{W} - 13.32 \left(\frac{a}{W}\right)^2 + 14.72 \left(\frac{a}{W}\right)^3 - 5.6 \left(\frac{a}{W}\right)^4\right]}{\left(1 - \frac{a}{W}\right)^{\frac{3}{2}}} \quad (3.2)$$

where P_Q = load applied (N or lbf)

B = specimen thickness (m or in)

B_N = specimen thickness between the roots of the side grooves (m or in)

W = specimen width (m or in)

a = crack length (m or in)

The fatigue pre-cracking experiment was performed under a sinusoidal cyclic loading at a load ratio of 0.1 with maximum applied load of 6,000 N giving a mean applied load of 3,300 N and a load amplitude of 2,700 N. Once the fatigue pre-crack of desired length was produced at the tip of the notch, the fatigue pre-crack lengths of the WOL specimens were measured using an optical microscope (Fig. 3.10).



Figure 3.10. Optical microscope to measure the fatigue pre-crack length.

3.5. Direct-current potential drop technique

Fracture mechanics-based SCC study involves monitoring of load, load line displacement (or crack mouth opening displacement), and crack length with time [5]. There are many ways crack length can be monitored – optical microscopy, scanning electron microscopy (SEM), replication, potential difference, and ultrasonics [6-17]. Due to its simplicity, the direct-current potential drop (DCPD) technique has been widely used for detecting crack initiation and monitoring crack growth. This technique involves supplying a constant current through the specimen and measuring

potential drop as crack propagates. The principle of DCPD as per ASTM E647–15 is as follows [18].

“Determining crack size from electric potential measurements relies on the principle that the electrical field in a cracked specimen with a current flowing through it is a function of the specimen geometry, and in particular the crack size. For a constant current flow, the electric potential or voltage drop across the crack plane will increase with increasing crack size due to modification of the electrical field and associated perturbation of the current streamlines. The change in voltage can be related to crack size through analytical or experimental calibration relationships.”

For prediction of crack length, a calibration curve has been developed for the specimen under consideration. Johnson [19] suggested that such calibration curves are independent of chemical composition, heat-treatment, and thickness. For the development of calibration chart, in the present case, the DCPD measurement unit involved a DC power supply from Kikusui (model number of PAT160-50T) and a nanovoltmeter from Keithley (model number of 2182A). The wires from the Keithley nanovoltmeter are attached to the WOL specimen as shown in Fig. 3.11 and Fig. 3.12 for measurements in air and marine environments respectively. During the DCPD measurement, a 0.2V and 5A current was supplied by the Kikusui DC power supply and a reading was obtained in mV from the Keithley nanovoltmeter up to six decimal points. Once the fatigue pre-crack length has been measured, the fatigue pre-cracked WOL specimen was setup as shown in Fig. 3.11 for DCPD measurement. After a reading has been recorded, the fatigue pre-cracking experiment was repeated (Fig. 3.8) for the second time along with fatigue pre-crack length (Figs. 3.10) and DCPD measurement (Figs. 3.11 & 3.12) to generate a calibration curve consisting of several data points.

For crack growth measurement, the DCPD measurement unit shown in Fig. 3.13a involves two DC power supplies from Kikusui (model number of PAT160-50T) for measurement of crack growth, BK Precision to provide electrical current for measuring applied load and two nanovoltmeters from Keithley (model 2182A) to measure the potential drop of the crack growth and from Fluke model 287 to measure the potential drop of the applied load throughout the experiment. The Keithley nanovoltmeter is attached to the WOL specimen and the load is applied through an instrumented bolt as shown in Fig. 3.13b. During the DCPD measurement, electrical current is supplied by the Kikusui and BK Precision DC power supply whereas the readings of crack growth and applied load are obtained in mV from the Keithley nanovoltmeter up to six decimal points and from Fluke nanovoltmeter up to three decimal points, respectively.

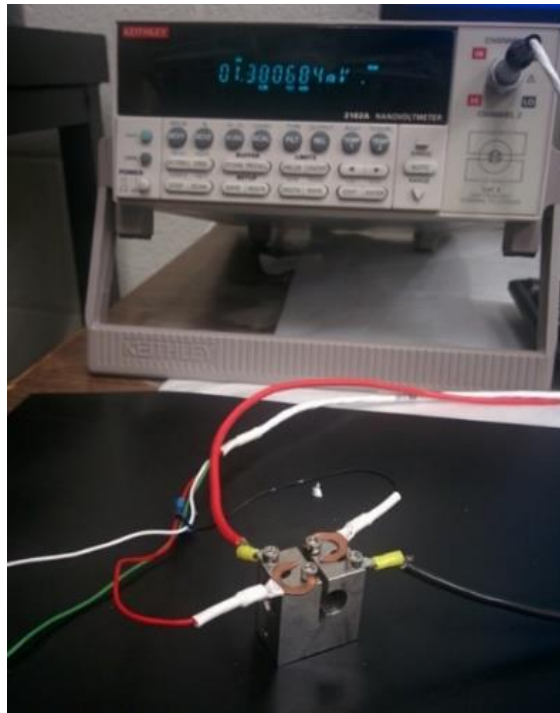


Figure 3.11. DCPD measurement in air for calibration chart.

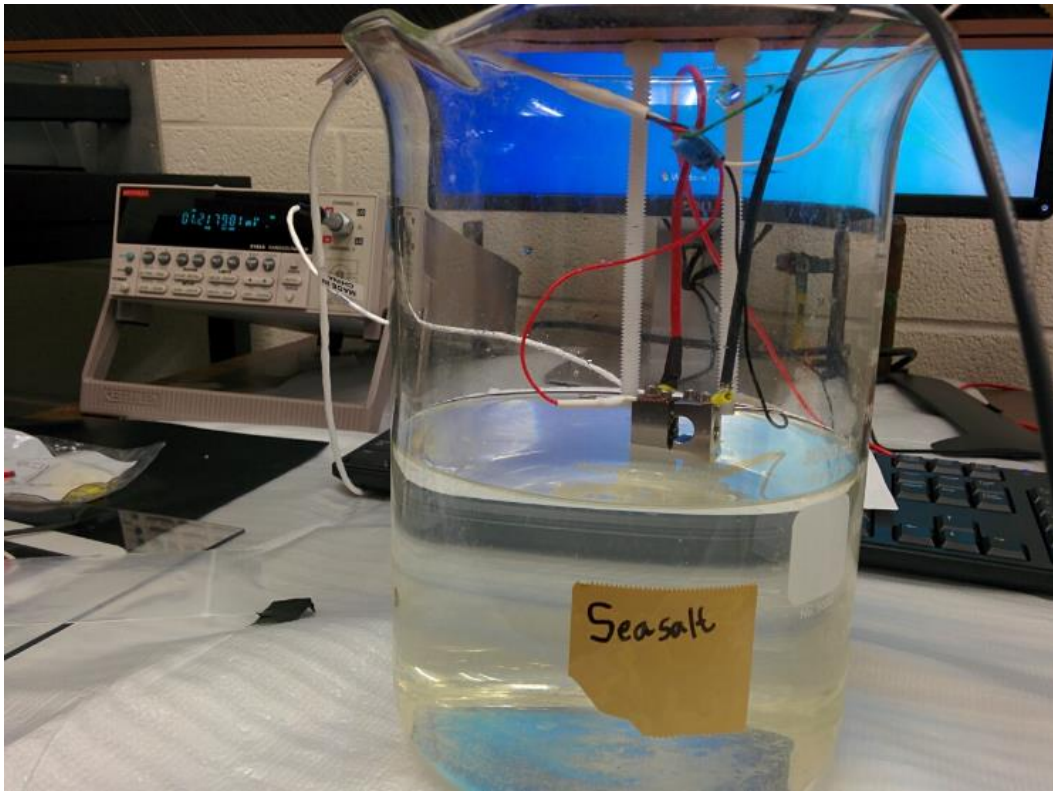


Figure 3.12. DCPD experiment setup in marine environment for calibration chart.

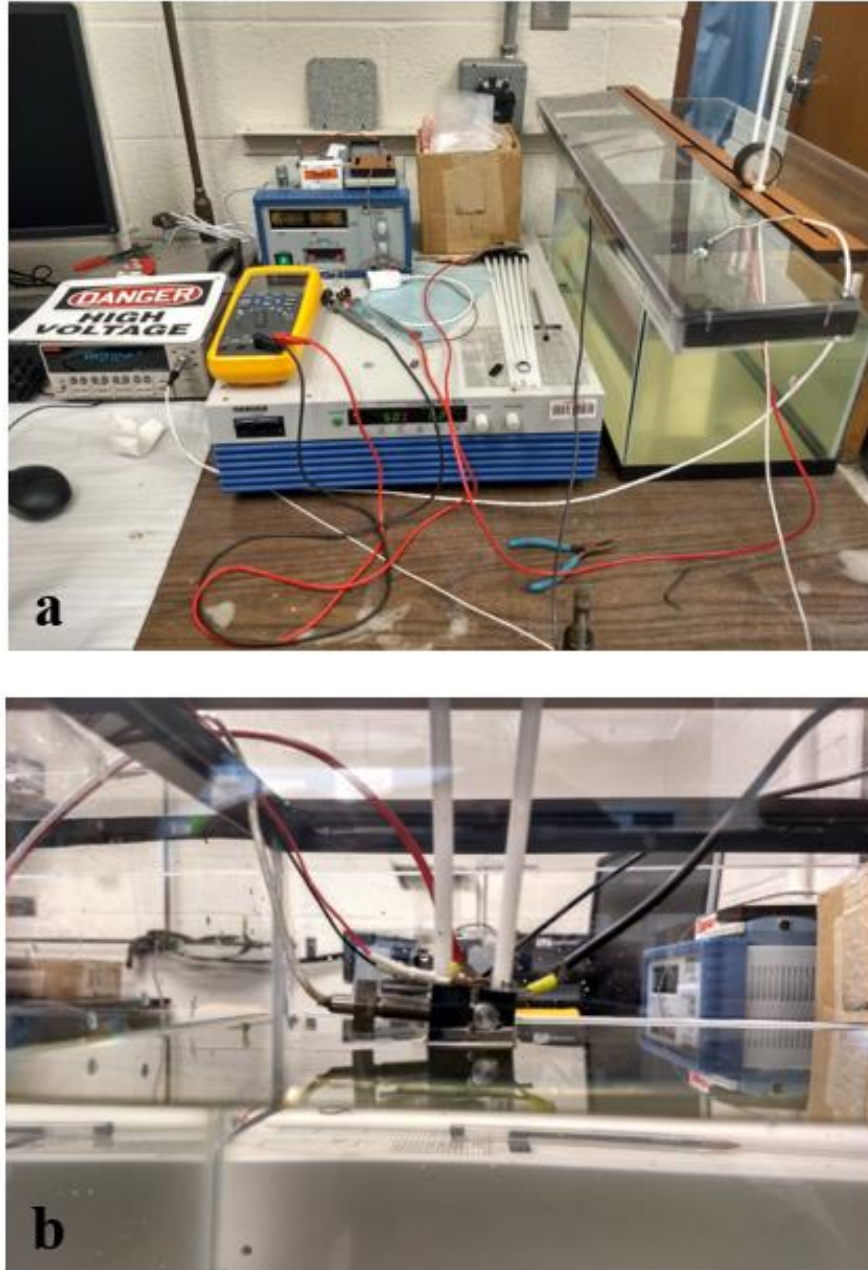


Figure 3.13. (a) Crack growth experimental setup and (b) WOL specimen submerged in marine environment.

The K_{ISCC} experiment involves loading the specimen such that the stress intensity factor is above K_{ISCC} and less than K_{IC} . A preliminary calculation has been performed that relates the stress intensity factor with the corresponding applied load for lower and upper limits of crack length of

7.72 and 9.43 mm ($0.45 \leq a/W \leq 0.55$), respectively. By utilizing Eqs. 3.1 and 3.2, for a specimen width of 0.675 in (17.145 mm) and a thickness of 0.625 in (15.875 mm), an applied load can be obtained for a specified value of stress intensity factor for the lower and upper limits of crack length.

The crack growth measurement is performed in marine environment (substitute ocean water) using DCPD technique where the fatigue pre-cracked WOL specimen is submerged in the corrosion chamber such that the fatigue pre-crack length is submerged in the marine solution with the notch staying above the surface of the marine solution [20].

3.6. References

- [1] ASTM, Standard Test Method for Linear-Elastic Plane-Strain Fracture Toughness K_{IC} of Metallic Materials, E399–12. ASTM International.
- [2] E. T. Wessel, State of the art of the WOL specimen for K_{IC} fracture toughness testing, Eng. Frac. Mech. 1 (1968) 77-82. [https://doi.org/10.1016/0013-7944\(68\)90017-9](https://doi.org/10.1016/0013-7944(68)90017-9).
- [3] ASTM, Standard Test Method for Measurement of Fracture Toughness, E1820-15. ASTM International.
- [4] ASTM, Standard Test Method for Determining Threshold Stress Intensity Factor for Environment-Assisted Cracking of Metallic Materials, E1681-03. ASTM International.
- [5] T. L. Anderson, Fracture Mechanics: Fundamentals and Applications, 3rd ed., CRC Press/Taylor & Francis, Boca Raton, 2005.
- [6] M. J. W. Kanters, J. Stolk, L. E. Govaert, Direct Comparison of the Compliance Method with Optical Tracking of Fatigue Crack Propagation in Polymers, Polymer Testing, 46 (2015) 98-107. <https://doi.org/10.1016/j.polymertesting.2015.07.005>.
- [7] W. Zhang, L. Cai, In-Situ SEM and Optical Microscopy Testing for Investigation of Fatigue Crack Growth Mechanism Under Overload, MATEC Web of Conferences 165 (2018). <https://doi.org/10.1051/matecconf/201816513013>.
- [8] Z. M. Connor, M. E. Fine, J. D. Achenbach, Acoustic, Electron and Optical Microscopy Visualization of Surface and Sub-surface Cracks, in: D. O. Thompson, D. E. Chimenti (Eds.), Review of Progress in Quantitative Nondestructive Evaluation, Springer, Boston, MA, 1998, pp. 1581-1588.
- [9] D. Kim, S. Ahn, K. Lee, The Development of Crack Measurement System Using the Direct Current Potential Drop Method for Use in the Hot Cell, JAERI Conference (1999) 140-150.

- [10] D. Chen, C. J. Gilbert, R. O. Ritchie, In Situ Measurement of Fatigue Crack Growth Rates in a Silicon Carbide Ceramic at Elevated Temperatures Using a DC Potential System, *J. Test. Eval.* 28 (2000) 236-241. <https://doi.org/10.1520/JTE12100J>.
- [11] S. Kalluri, J. Telesman, Characterization of Fatigue Crack Initiation and Propagation in Ti-6Al-4V with Electrical Potential Drop Technique, NASA Technical Memorandum 100877 (1988).
- [12] M. A. Hicks, A. C. Pickard, A Comparison of Theoretical and Experimental Methods of Calibrating the Electrical Potential Drop Technique for Crack Length Determination, *Int. J. Fract.* 20 (1982) 91-101. <https://doi.org/10.1007/BF01141259>.
- [13] A. Bakker, A DC Potential Drop Procedure for Crack Initiation and R-Curve Measurements During Ductile Fracture Tests, in: E. T. Wissel, F. J. Loss (Eds.), *Elastic-Plastic Fracture Test Methods: The User's Experience*, ASTM STP 856, ASTM International, West Conshohocken, PA, 1985, pp. 394-410.
- [14] T. Terachi, T. Yamada, T. Miyamoto, K. Arioka, SCC Growth Behaviors of Austenitic Stainless Steels in Simulated PWR Primary Water, *J. Nucl. Mater.* 426 (2012) 59-70. <https://doi.org/10.1016/j.jnucmat.2012.03.013>.
- [15] P. L. Andresen, Effects of Temperature on Crack Growth Rate in Sensitized Type 304 Stainless Steel and Alloy 600, *Corros. Sci.* 49 (1993). 714-725. <https://doi.org/10.5006/1.3316104>.
- [16] N. Parida, S. Tarafder, Monitoring Part-Through Crack Growth Using Compliance Technique, ICF10054PR, National Metallurgical Laboratory, India.

- [17] A. Keshtgar, M. Modarres, A Probabilistic Approach to Small Fatigue Crack Initiation and Sizing Using Acoustic Emission, Preprints (2017).
<https://doi.org/10.20944/preprints201702.0062.v1>.
- [18] ASTM, Standard Test Method for Measurement of Fatigue Crack Growth Rates, E647-15. ASTM International.
- [19] H. H. Johnson, Calibrating the Electric Potential Method for Studying Slow Crack Growth, Mater. Res. Stand. 5 (1965) 442-445.
- [20] M.O. Speidel, Stress Corrosion Cracking of Stainless Steels in NaCl Solutions, Metall. Trans. 12A (1981) 779-789. <https://doi.org/10.1007/BF02648342>.

CHAPTER 4: RESULTS AND DISCUSSION

4.1. Microstructural characterization of as-received samples

Prior to the crack growth experiments, the SS304H/L materials sensitized at 600 °C for 215 hours received from Colorado School of Mines (CSM) were mechanically polished down to mirror finish and etched with a solution of hydrochloric acid, nitric acid and water of equivalent ratio, cleaned with methanol and deionized water for metallography. The energy dispersive spectroscopy (EDS) in SEM was used to detect the distribution of different elements among different phases present in the alloy as shown in Fig. 4.1 and 4.2 for SS304H and L, respectively.

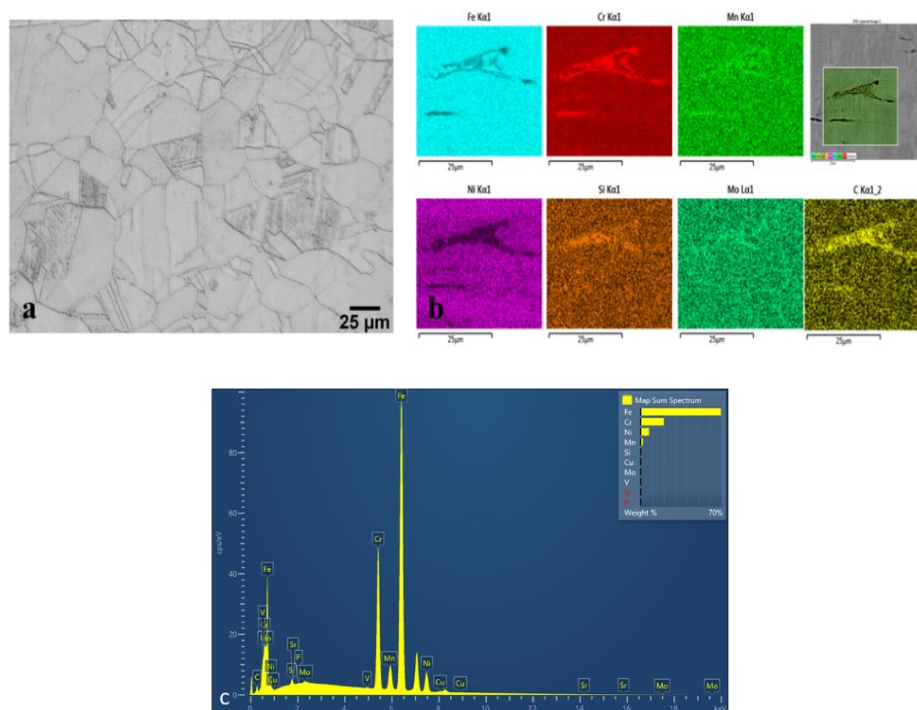


Figure 4.1. (a) Optical micrograph, (b) Elements identified from EDS and (c) Intensities of the identified elements through EDS of SS304H.

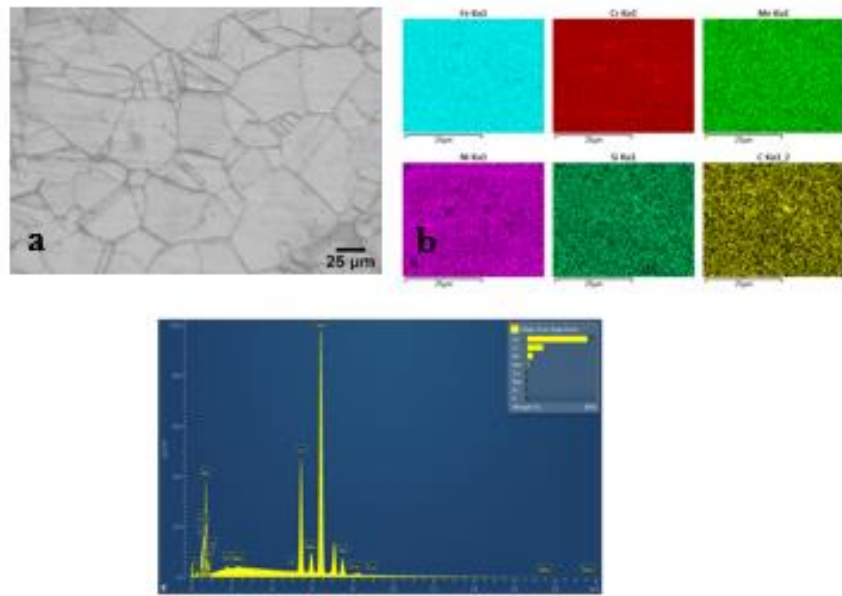


Figure 4.2. (a) Optical micrograph, (b) Elements identified from EDS and (c) Intensities of the identified elements through EDS of SS304L.

4.2. Mechanical properties

Tensile tests were performed at a strain rate of 10^{-3} /s in air at room temperature for both SS304H and SS304L in the rolling (RD) and transverse (TD) directions, and the results are tabulated in Table 4.1.

Table 4.1. Tensile test results of sensitized (at 600 °C for 215 hrs) SS304H/L with the errors indicated inside the brackets.

	Yield Stress (MPa)	UTS (MPa)	Uniform Elongation (%)	Total Elongation (%)
SS304H 215 hrs RD	302 (11)	701 (14)	80.8 (5.3)	92.4 (4.6)
SS304H 215 hrs TD	272 (9)	702 (14)	76.6 (2.8)	84.2 (1.3)
SS304L 215 hrs RD	264 (15)	670 (7)	84.3 (2.0)	97.7 (0.4)
SS304L 215 hrs TD	274 (5)	672 (22)	85.7 (4.8)	96.6 (8.4)

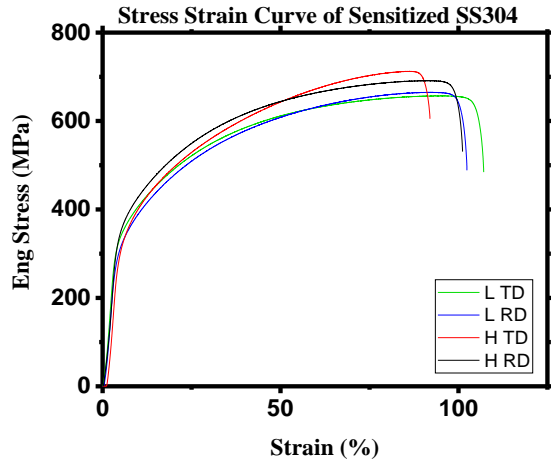


Figure 4.3. Engineering stress-engineering strain curve of SS304H/L in rolling and transverse directions.

4.3. Calibration chart

After the steps of the experiment were repeated several times as described in section 3.5, a calibration curve with a reliable set of data is generated as shown in Fig. 4.4. The objective of these DCPD measurements is to create a calibration curve for a WOL specimen that will be used to study the SCC behavior of SS304 in marine environments which also requires monitoring of crack-growth using DCPD during the experiment.

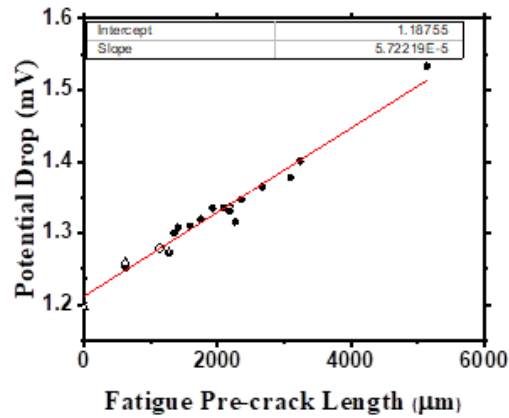


Figure 4.4. Calibration curve of potential drop of WOL specimen as a function of fatigue pre-crack length in air (solid) and marine environments (open).

The values from the DCPD measurements in the marine environment were plotted in the same graph as those in air and are shown in Fig. 4.4. Clearly, the DCPD measurements in marine environment yield similar results to those in air producing a linear relationship between the potential drop and the fatigue pre-crack length. In the fatigue pre-cracked WOL specimen, as crack length increases, resistance increases and therefore, the potential drop increases. This calibration curve was used for the SCC experiments in the project.

4.4. Crack growth experiments

4.4.1. Crack growth tests with non-sensitized SS304 specimens

Before using the sensitized SS304H/L, two crack growth experiments were performed using non-sensitized SS304 materials to characterize the archival materials. First experiment was conducted with a non-sensitized SS304 material with a fatigue pre-crack length of 2,475 μm but the specimen plastically deformed beyond an applied load of 1,000 lbf as shown in Fig. 4.5. Another attempt was made with the same material with a fatigue pre-crack length of 3,200 μm and the specimen, again, plastically deformed at 1,000 lbf as shown in Fig. 4.6. Although these two attempts did not produce important outcomes, a particular note is made on the maximum applied load of 1,000 lbf for non-sensitized SS304 material for future experiments.

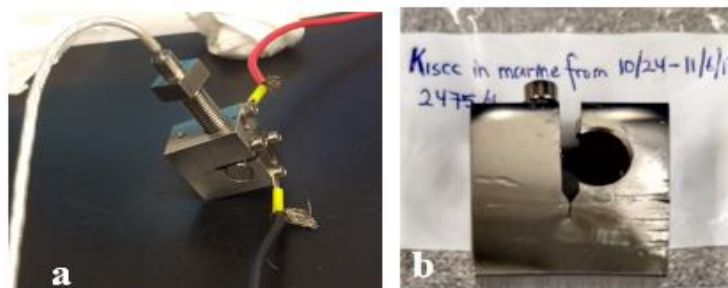


Figure 4.5. (a) A non-sensitized SS304 specimen with a fatigue pre-crack length of 2,475 μm under load and (b) The deformed specimen after 1,000 lbf.

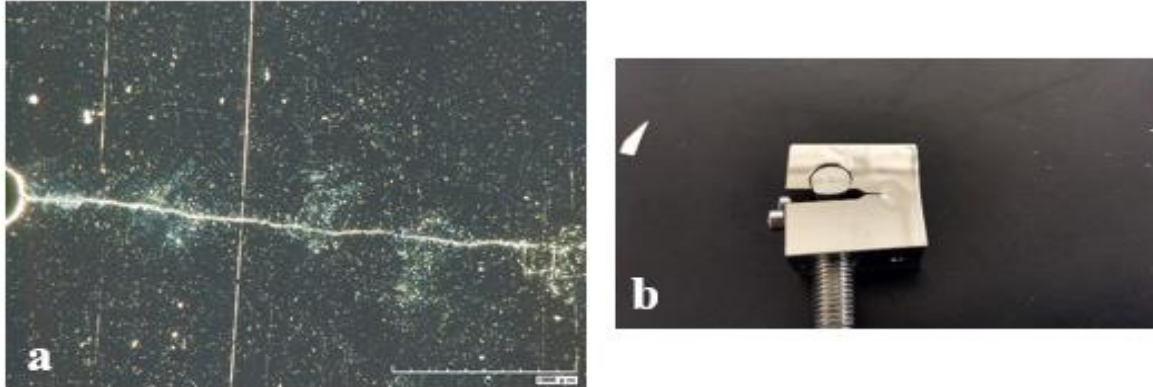


Figure 4.6. (a) Non-sensitized SS304 specimen fatigue pre-cracked to 3,200 μm and (b) The plastically-deformed specimen after 1,000 lbf.

With the consideration that the non-sensitized SS304 material cannot be loaded beyond 1,000 lbf without excessive plastic deformation ahead of the crack tip implying low value for stress intensity factor, the crack growth experiments were then performed with sensitized SS304 H/L. A sensitized SS304H specimen was fatigue pre-cracked to 897 μm and submerged in substitute ocean water (composition given in Table 4.2) with an applied load of 1,872 lbf ($34 \text{ MPa m}^{1/2}$ from Eq. 3.1 and 3.2) at room temperature for six weeks. In addition, a calculation was performed to determine the stress intensity factor that corresponds to the initial applied load with an example shown in Table 4.3.

Table 4.2. Chemical composition of the substitute ocean water [1,2].

Compound	NaCl	MgCl ₂	Na ₂ SO ₄	CaCl ₂	KCl	NaHCO ₃	KBr	H ₃ BO ₃	SrCl ₂	NaF
Concentration (g/L)	24.53	5.20	4.09	1.16	0.695	0.201	0.101	0.027	0.025	0.003

Table 4.3. Load calculation versus K_I values for a specimen with two different crack lengths.

K_I (MPa \sqrt{m})	$a_o = 7.72$ mm		$a_o = 9.43$ mm	
	P (N)	P (lbf)	P (N)	P (lbf)
5	1245.29	279.95	914.51	205.59
10	2490.57	559.90	1829.02	411.18
15	3735.86	839.86	2743.53	616.77
20	4981.15	1119.81	3658.04	822.36
25	6226.43	1399.76	4572.55	1027.95
30	7471.72	1679.71	5487.06	1233.54
35	8717.01	1959.66	6401.57	1439.13
40	9962.29	2239.61	7316.08	1644.72
45	11207.58	2519.57	8230.59	1850.31
50	12452.87	2799.52	9145.10	2055.90
55	13698.16	3079.47	10059.61	2261.49
60	14943.44	3359.42	10974.12	2467.08
65	16188.73	3639.37	11888.63	2672.67
70	17434.02	3919.32	12803.14	2878.26
75	18679.30	4199.28	13717.65	3083.85
80	19924.59	4479.23	14632.16	3289.44
85	21169.88	4759.18	15546.67	3495.03
90	22415.16	5039.13	16461.18	3700.62
95	23660.45	5319.08	17375.69	3906.21
100	24905.74	5599.03	18290.20	4111.80

4.4.2. Crack growth experiments with sensitized SS304H specimens in substitute ocean water

The plots of bolt load and crack length with time in Figs. 4.7a and 4.7b indicate that the applied load decreases slowly and the crack length remains constant. Thus, the crack did not propagate for the first 310 hrs of the experiment. But the steep decrease in bolt load with time and increase in crack length with time (Figs. 4.7c and 4.7d) afterwards suggest that crack propagation occurred. The stress intensity factor decreases exponentially with crack extension (Fig. 4.7e) and further data analyses yielded the average crack growth rate of SS304H at 22 °C under substitute ocean water to be $0.975 \times 10^{-10} \pm 9.528 \times 10^{-12}$ m/s which is in good agreement with the average crack growth rate for SS304 at 22 °C as reported by Speidel of 1.438×10^{-10} m/s [3].

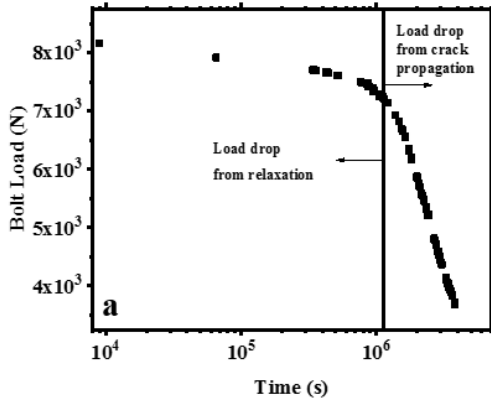


Figure 4.7a. Bolt load variation with time

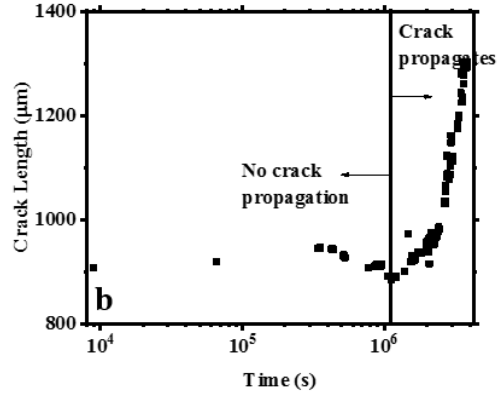


Figure 4.7b. Crack length versus time

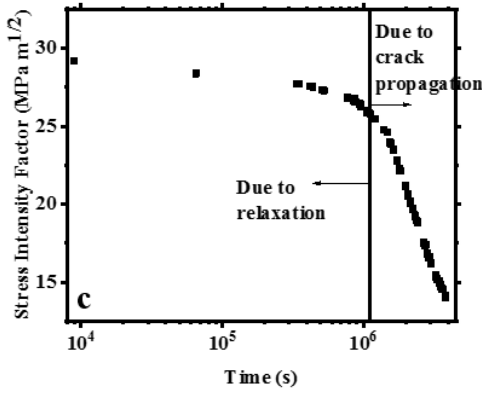


Figure 4.7c. Stress intensity factor with time

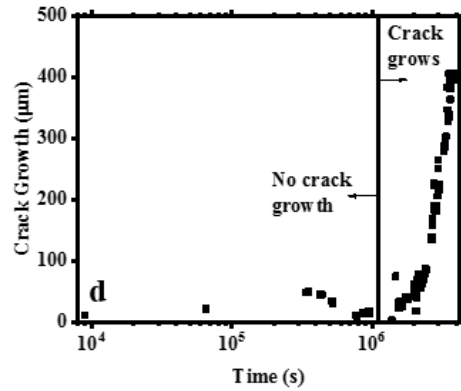


Figure 4.7d. Crack growth versus time

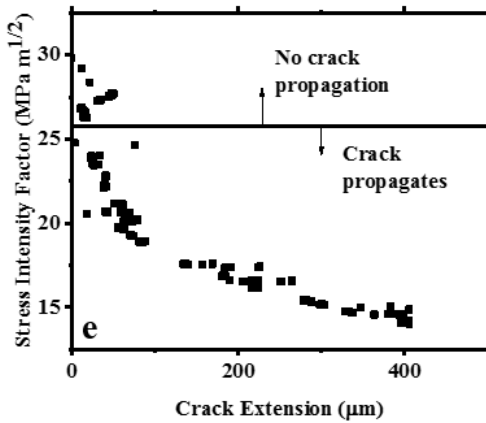


Figure 4.7e. Stress intensity factor versus crack extension

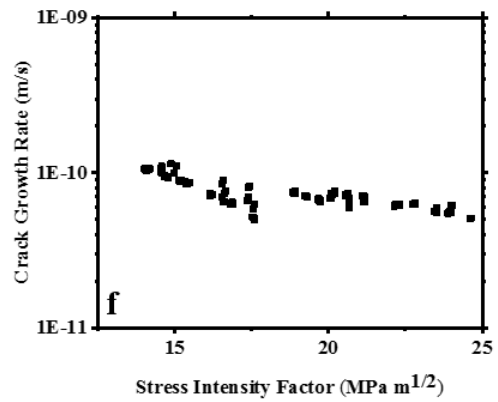


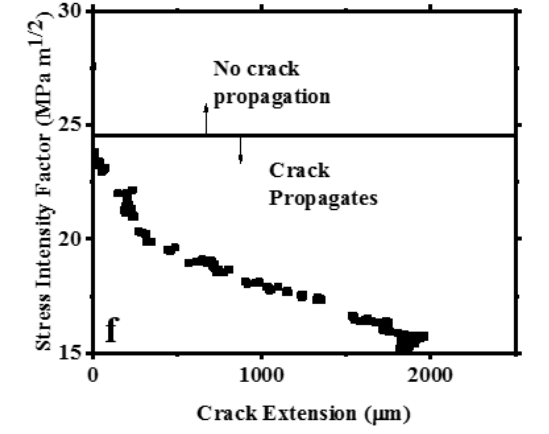
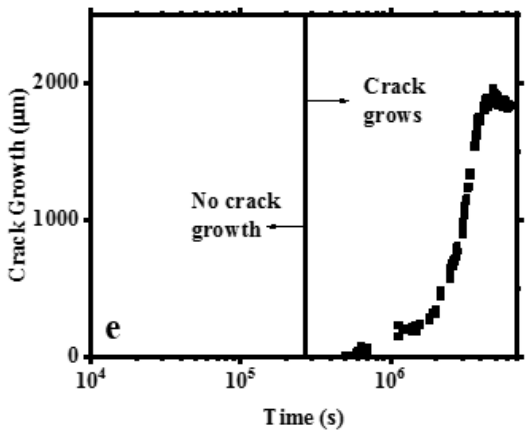
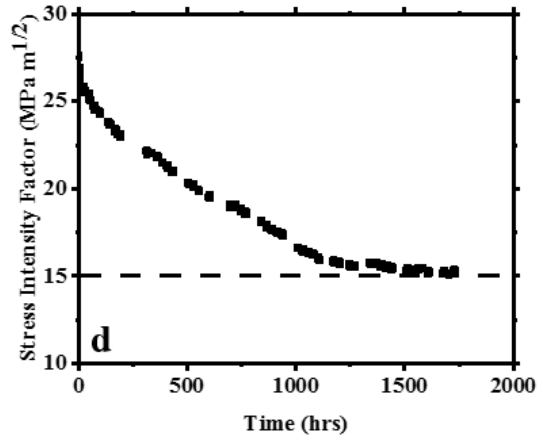
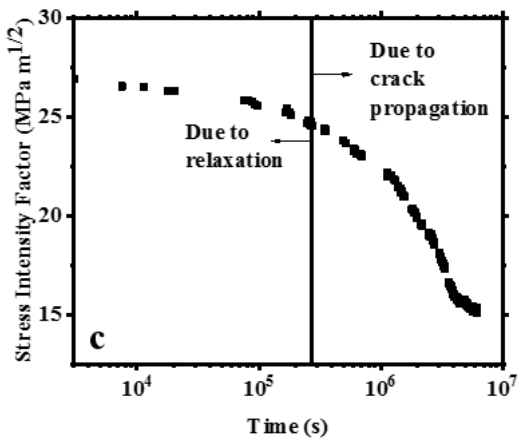
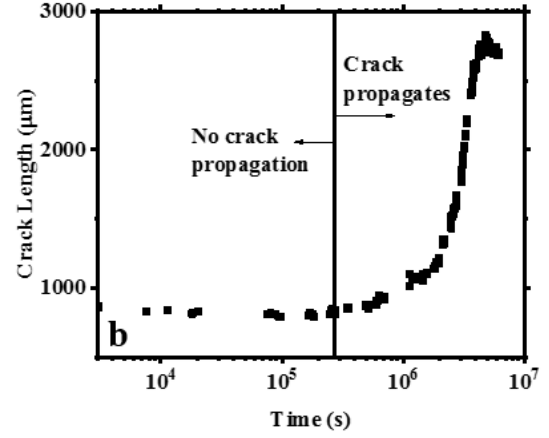
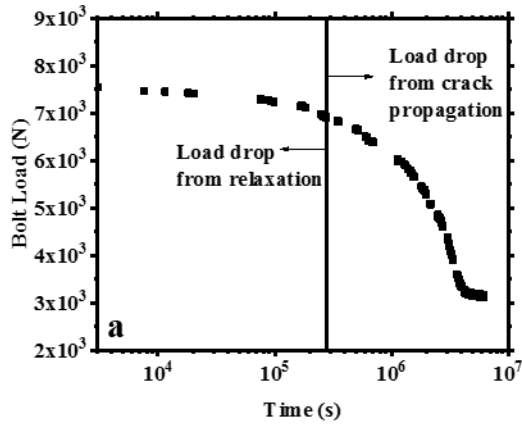
Figure 4.7f. Crack growth rate with stress intensity factor for SS304H under substitute ocean water at 22 °C.

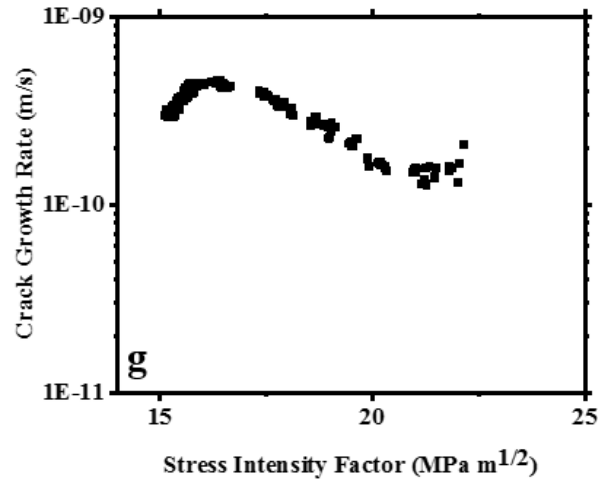
Another experiment was conducted with a sensitized SS304H specimen fatigue pre-cracked to 860 μm and with an applied load of 1,730 lbf ($31 \text{ MPa m}^{1/2}$) submerged in substitute ocean water at 37 $^{\circ}\text{C}$ for nine weeks. As the experiment was conducted at higher temperature, the crack propagation occurred earlier than at 22 $^{\circ}\text{C}$. From the bolt load behavior with time in Fig. 4.8a and crack length versus time in Fig. 4.8b, crack is noted to propagate after three days of the experiment. Performing the experiment for a longer time produced a saturation in the behavior of stress intensity factor with time as shown in Fig. 4.8d giving a threshold stress intensity factor (K_{ISCC}) of SS304H at 37 $^{\circ}\text{C}$ under substitute ocean water of $15 \text{ MPa m}^{1/2}$. Although there is no direct comparison for K_{ISCC} at this temperature, a fair comparison can be made with that obtained by Speidel for sensitized SS304 in 22% NaCl environment at 105 $^{\circ}\text{C}$ of $9 \text{ MPa m}^{1/2}$ [4]. Figure 4.8f shows that the stress intensity factor decreases in the same manner as in the previous experiment and data analyses from Fig. 4.8g for SS304H experiment at 37 $^{\circ}\text{C}$ under substitute ocean water produces an average crack growth rate of $3.258 \times 10^{-10} \pm 9.551 \times 10^{-11} \text{ m/s}$. A calculation of J_{ISCC} is shown in Eq. 4.1,

$$J = \frac{K^2(1-\nu^2)}{E} \quad (4.1)$$

and by using the obtained data from the crack growth experiment of $K_{\text{ISCC}} = 15 \text{ MPa m}^{1/2}$, $\nu = 0.3$, and $E = 200 \text{ GPa}$, $J_{\text{ISCC}} = 1023.75 \text{ J/m}^2$ is obtained.

Figure 4.8. (a) Bolt load versus time, (b) crack length versus time, (c) stress intensity factor versus logarithmic time, (d) threshold stress intensity factor, (e) crack growth versus time, (f) stress intensity factor versus crack growth and (g) crack growth rate with stress intensity factor for SS304H under substitute ocean water at 37 °C.





Another sensitized SS304H specimen was fatigue pre-cracked to 735 μm and submerged in substitute ocean water with a starting applied load of 30 $\text{MPa m}^{1/2}$ at 60 $^{\circ}\text{C}$. The plots of bolt load and crack length with time in Figs. 4.9a and 4.9b indicate that the applied load decreases slowly and the crack length remains constant for the first 18 hours of the experiment. Based on the applied load behavior with time, the stress intensity factor with time was obtained as displayed in Fig. 4.9c. Fig. 4.9d shows the crack growth behavior with time indicating crack extension occurred after 18 hours (6.7×10^4 s). In addition, following crack propagation, the stress intensity factor decreases exponentially with crack extension (Fig. 4.9e). Crack growth rate behavior with stress intensity factor in Fig. 4.9f produces an average crack growth rate of SS304H at 60 $^{\circ}\text{C}$ under substitute ocean water of $1.580 \times 10^{-9} \pm 2.593 \times 10^{-10}$ m/s.

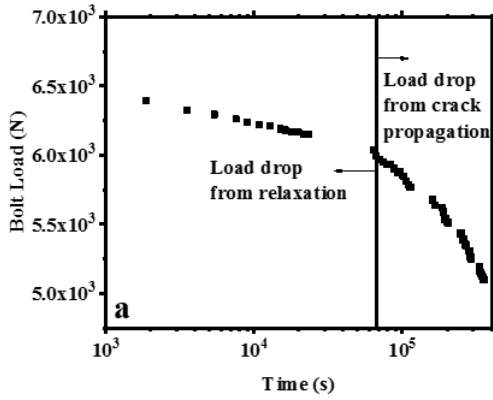


Figure 4.9a. Bolt load versus time

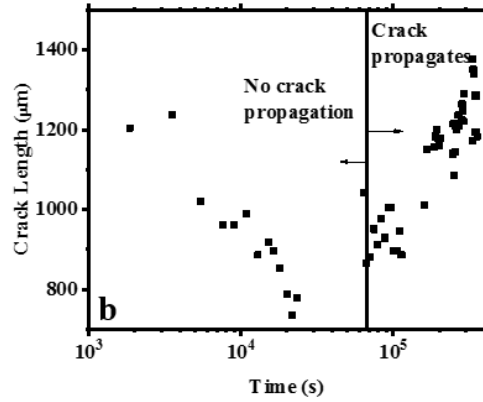


Figure 4.9b. Crack length versus time

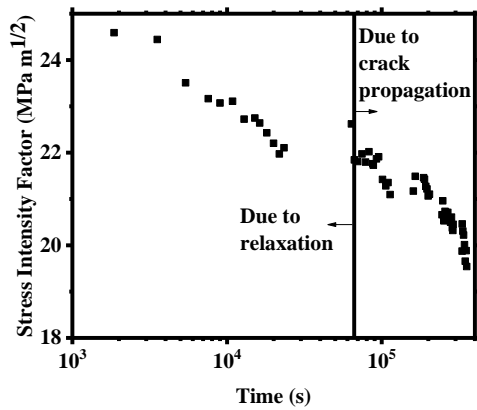


Figure 4.9c. Stress intensity factor with time

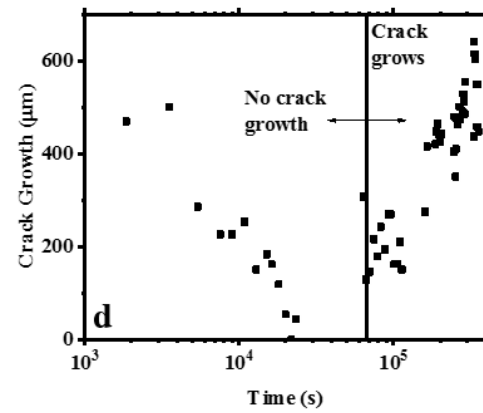


Figure 4.9d. Crack growth versus time

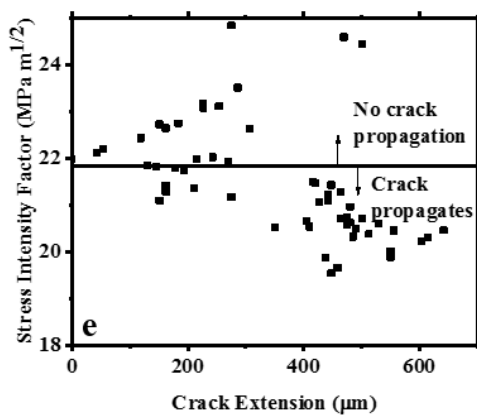


Figure 4.9e. Stress intensity factor with crack extension

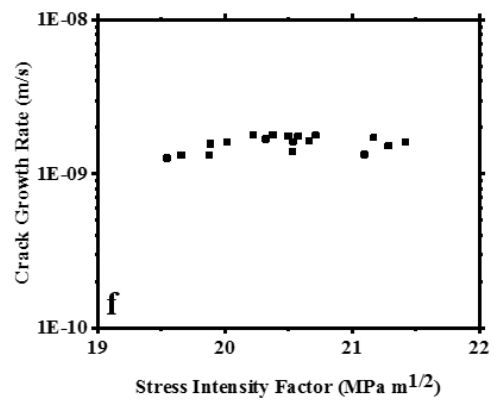


Figure 4.9f. Crack growth rate versus stress intensity factor for SS304H at 60 °C.

4.4.3. Crack growth experiments with sensitized SS304L specimens in substitute ocean water

To determine the effect of carbon content on corrosion resistance, three experiments were conducted with sensitized SS304L specimens. Three specimens were fatigue pre-cracked to 1,450 μm with an initial applied load of 1,712 lbf ($34.3 \text{ MPa m}^{1/2}$), 980 μm with an initial applied load of 1,545 lbf ($28.6 \text{ MPa m}^{1/2}$) and 1,000 μm with 1,472 lbf ($27.3 \text{ MPa m}^{1/2}$) and were all submerged in substitute ocean water at temperatures of 21, 38 and 60 °C, respectively. Data analyses yielded an average crack growth rate of $3.064 \times 10^{-11} \pm 4.009 \times 10^{-12} \text{ m/s}$ for SS304L experiment at 21 °C, $1.945 \times 10^{-10} \pm 1.315 \times 10^{-11} \text{ m/s}$ at 38 °C and $8.830 \times 10^{-10} \pm 9.863 \times 10^{-11} \text{ m/s}$ at 60 °C. These average crack growth rates are lower compared to those for SS304H indicating that the lower the carbon content, the better the corrosion resistance and therefore, the lower the crack growth rate. The results from the experiments with sensitized SS304L are presented in Figs. 4.10-4.12, respectively for the three specimens.

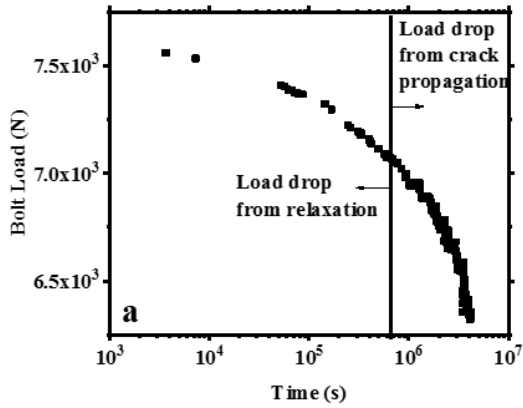


Figure 4.10a. Bolt load versus time

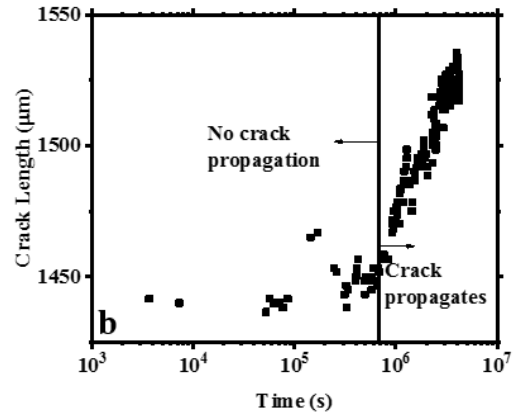


Figure 4.10b. Crack length versus time

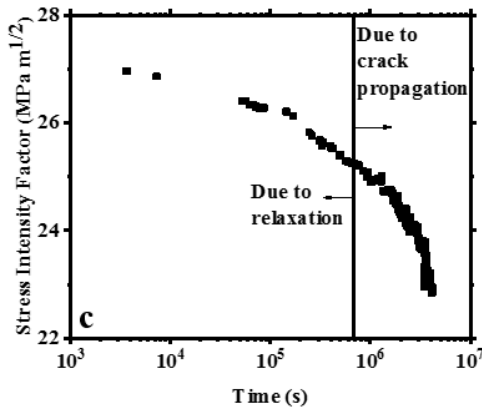


Figure 4.10c. Stress intensity factor with time

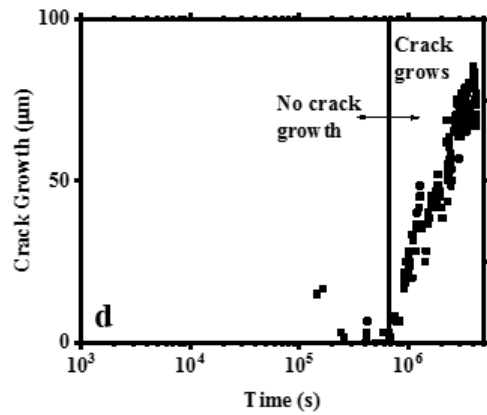


Figure 4.10d. Crack growth versus time

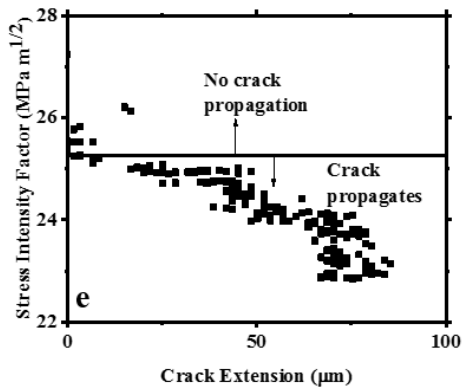


Figure 4.10e. Stress intensity factor with crack extension

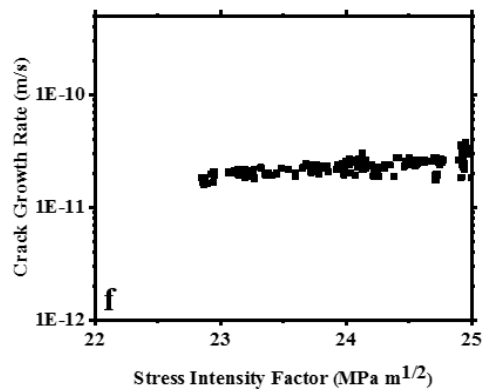


Figure 4.10f. Crack growth rate versus stress intensity factor for SS304L at 21 °C.

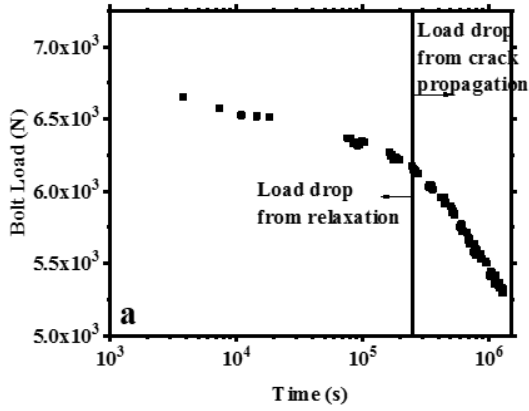


Figure 4.11a. Bolt load versus time

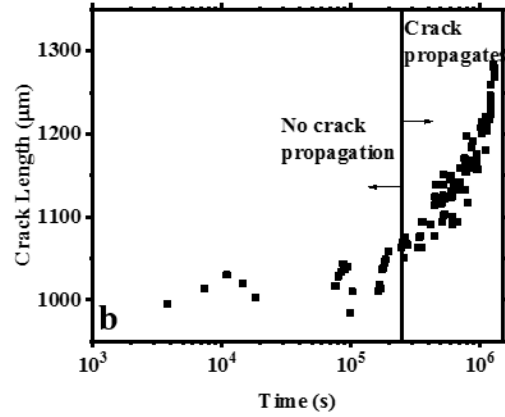


Figure 4.11b. Crack length versus time

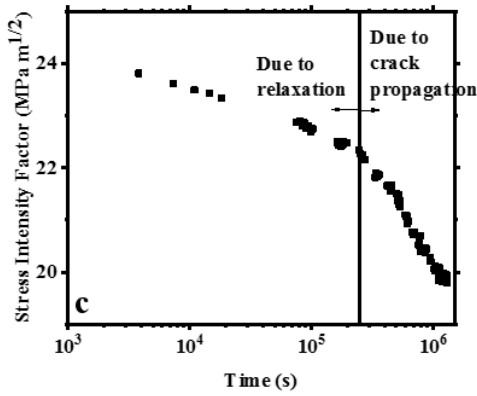


Figure 4.11c. Stress intensity factor with time

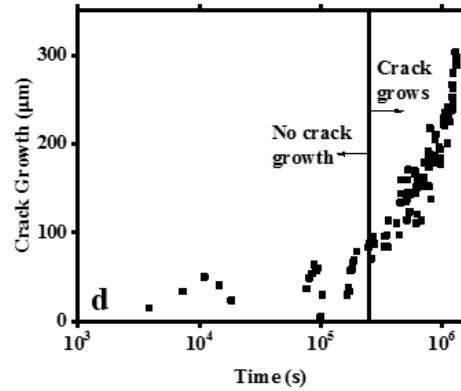


Figure 4.11d. Crack growth versus time

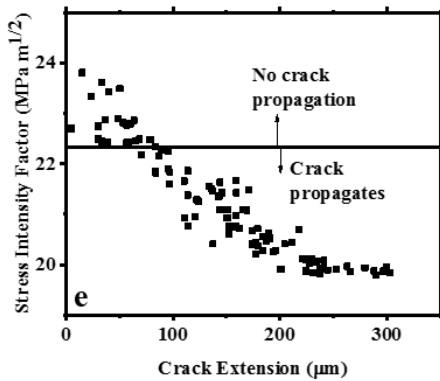


Figure 4.11e. Stress intensity factor with crack extension

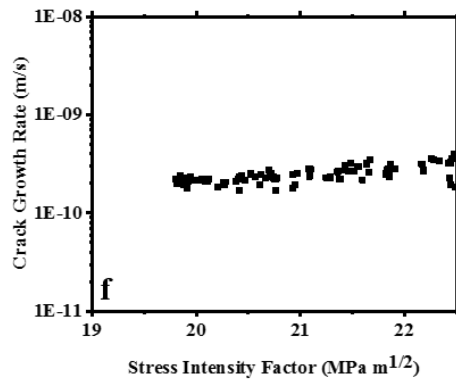


Figure 4.11f. Crack growth rate versus stress intensity factor for SS304L at 38 °C.

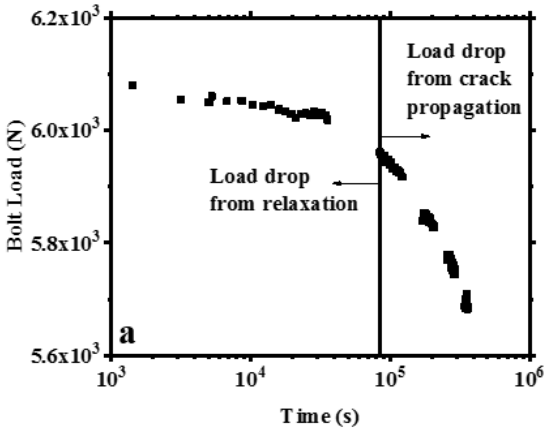


Figure 4.12a. Bolt load versus time

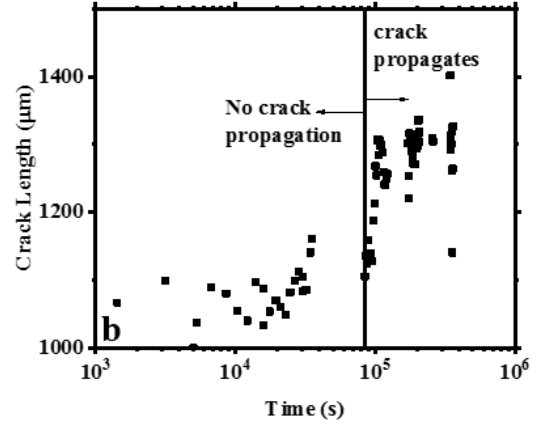


Figure 4.12b. Crack length versus time

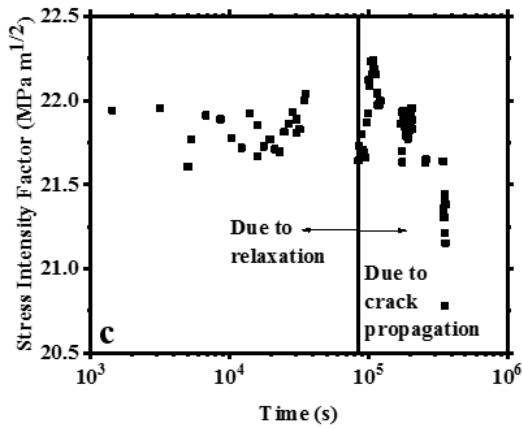


Figure 4.12c. Stress intensity factor with time

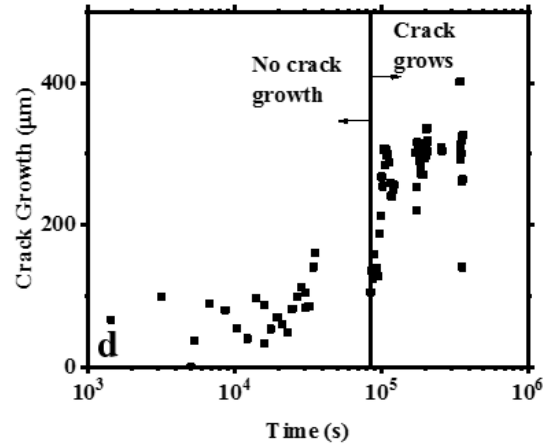


Figure 4.12d. Crack growth versus time

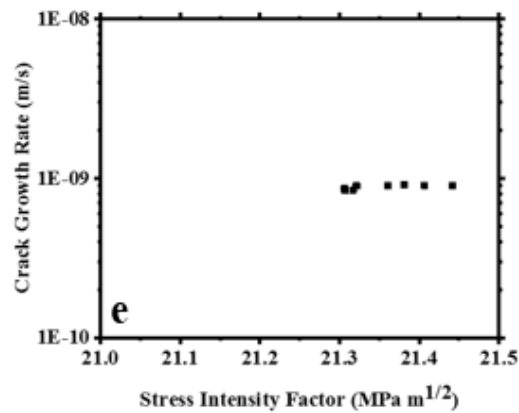


Figure 4.12e. Crack growth rate versus stress intensity factor for SS304L at 60 °C.

4.4.4. Effect of temperature on crack growth of sensitized SS304 specimens in substitute ocean water

The temperature dependence of the crack growth rates is described through an Arrhenius equation as expressed by

$$\frac{da}{dt} = C \exp\left[\frac{-Q}{RT}\right] \quad (4.2)$$

where da/dt = crack growth rate (m/s), C = an arbitrary constant, Q = activation energy (J/mol), R = universal gas constant (8.314 J/mol K) and T = temperature (K). The average crack growth rates obtained with sensitized SS304H and sensitized SS304L each at three different temperatures are plotted as a function of their corresponding inverse temperatures in Fig. 4.13. The activation energy is then evaluated from the slope of the lines to be 60.9 ± 0.62 kJ/mol for sensitized SS304H and 69.1 ± 8.96 kJ/mol for sensitized SS304L, respectively.

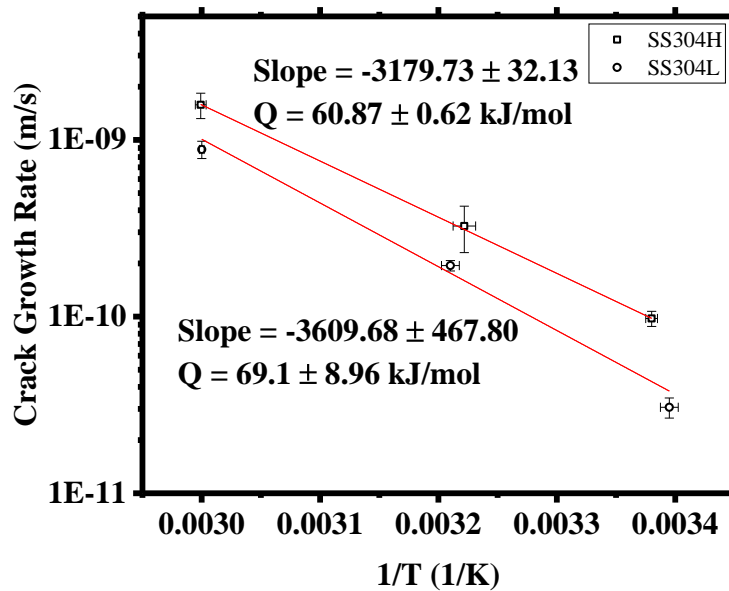
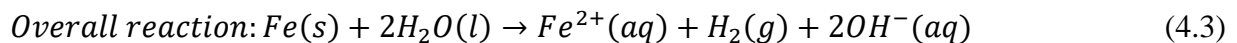
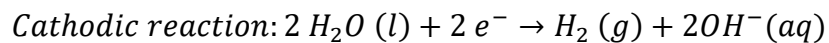
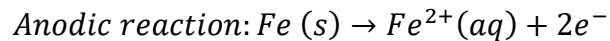


Figure 4.13. Arrhenius plot of crack growth rates for sensitized SS304H and sensitized SS304L.

These two activation energies are in agreement with those obtained by Khatak et al in the range of 50-65 kJ/mol for sensitized SS304 in NaCl environment [5,6]. Louthan and Derrick associated this activation energy with hydrogen diffusion in iron and austenitic stainless steels [6-8] implying hydrogen embrittlement is responsible for stress corrosion cracking. Hydrogen is produced in the cathode as shown in Eq. 4.3 where it then enters the region of higher triaxial tensile stress regions in the steel matrix at the crack tip creating corrosion tunnels. These corrosion tunnels in turn initiate crack which then sharpen the crack tip thereby increasing the stress concentration. Hydrogen then segregates at slip bands and grain boundaries ahead of the crack tip separating the grain boundaries to produce intergranular fracture [9-12]. This propagating crack caused by crack-tip deformation produces brittle fracture as encountered in in-service structures [13]. As in any reaction, temperature dictates the speed of the particles' movement [14] and for the case of crack growth, the speed of hydrogen propagation through the tunnels enhances crack growth. Increasing temperature increases the speed of the particles resulting in an increase of speed of hydrogen propagation through the tunnels which is reflected in higher average crack growth rates for higher operating temperatures as seen in Fig. 4.13. The effect of temperature on crack growth rate is confirmed by Andresen [15] and Spencer et al [16].



The average crack growth rates obtained from the experiments with sensitized SS304H and sensitized SS304L in substitute ocean water are compared with those from Speidel with sensitized SS304 in NaCl solution [3] in Fig. 4.14.

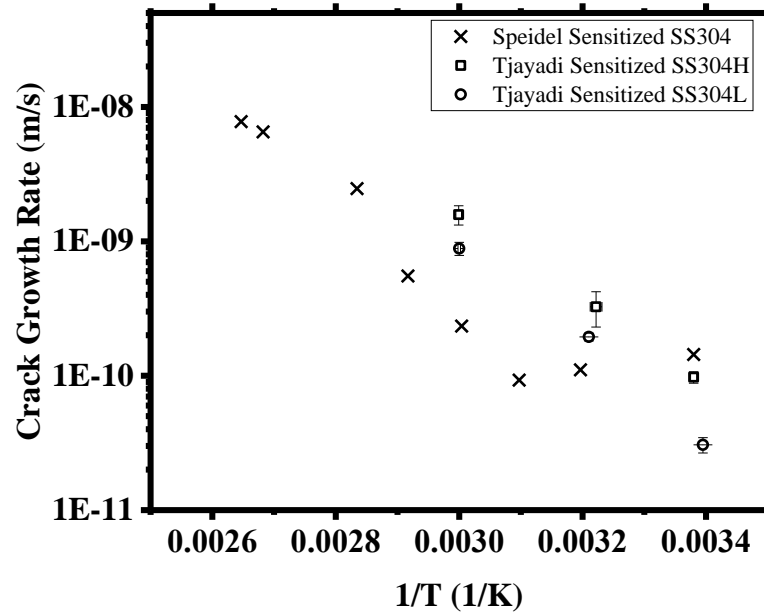


Figure 4.14. Comparison of average crack growth rates between the experimental values and those from Speidel at 22, 40 and 60 °C [3].

4.4.5. Effect of temperature on crack initiation in substitute ocean water

Figure 4.15a shows time for crack initiation versus temperature and Fig. 4.15b shows Arrhenius plot of crack initiation time for both sensitized SS304H and sensitized SS304L where the time for crack initiation is strongly dependent upon temperature. Temperature dictates the speed of the particles' movement in a reaction [14] and for the case of crack initiation, temperature governs the speed of transport of chloride ions to the crack tip where chloride ions remove the antioxidant or passive surface film from the surface of a material and initiate the oxidation process

[17,18]. Increasing temperature increases the speed of transport of chloride ions to the crack tip implying that the destruction of passive surface film will occur earlier. This is reflected in Fig. 4.15 where crack initiation occurs earlier for higher operating temperature. The influence of temperature on crack initiation was also investigated by Andresen in his study with sensitized SS304 [15] and Spencer et al. with SS304L [16] who obtained an activation energy of 42 and 34 kJ/mol, respectively indicating diffusion of chloride ions to the crack tip.

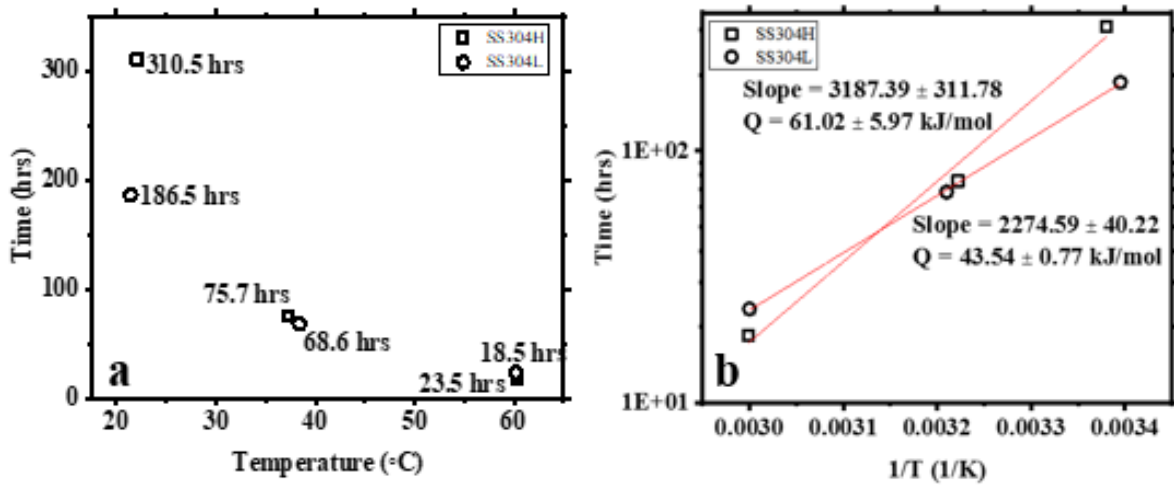


Figure 4.15. (a) Crack initiation time versus temperature and (b) Arrhenius plot of crack initiation time for sensitized SS304H and sensitized SS304L under substitute ocean water.

Thompson suggested that two mechanisms are involved in SCC [19]; slip dissolution mechanism which is responsible for crack tip sharpening and crack initiation [20,21] and hydrogen embrittlement which causes crack propagation [22-24]. Based on the experiments conducted, chloride ions are vital for crack initiation in breaking the passive surface film and hydrogen embrittlement is responsible for crack propagation in SCC with temperature being an important parameter [25]. As hydrogen is produced from the corrosion reaction, temperature dictates the speed of the reaction kinetics of hydrogen, i.e. temperature determines the speed of the hydrogen

transport to the crack tip and once the crack initiates, hydrogen diffuses through the grain boundaries for crack propagation [26]. The higher the temperature, the faster the hydrogen transport to the crack tip as indicated by the crack initiation time and faster the hydrogen propagation through grain boundaries as shown by the crack growth rates.

4.4.6. Crack growth experiments on sensitized SS304L in NaCl solution

An experiment was carried out to investigate the effect of salt concentration on crack growth rate with sensitized SS304L at 39 °C in a higher salt concentration of 126 g/L NaCl. The specimen was fatigue pre-cracked to 732 μm with an initial applied load of 1,631 lbf (28.9 MPa m^{1/2}) and yielded an average crack growth rate of $1.985 \times 10^{-10} \pm 2.603 \times 10^{-11}$ m/s (Fig. 4.16e) indicating that higher salt concentration does not increase the crack growth rate in SS304L. However, the crack initiation occurred faster at higher salt concentration (64.5 hrs) compared to the experiment with sensitized SS304L at 38 °C in 42 g/L substitute ocean water (68.6 hrs). Therefore, the higher the salt concentration, the faster is the crack initiation.

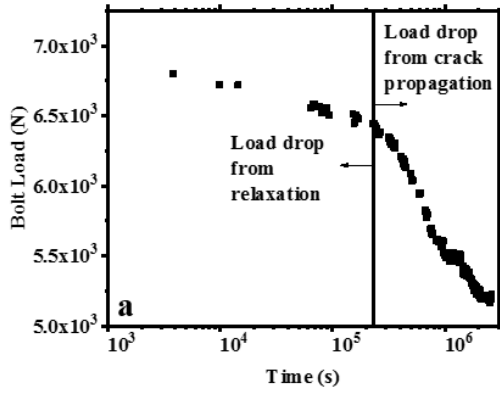


Figure 4.16a. Bolt load versus time

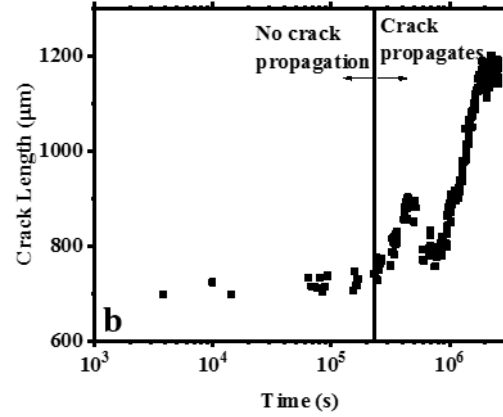


Figure 4.16b. Crack length versus time

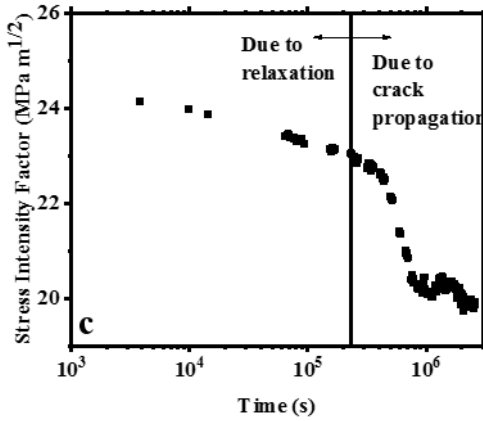


Figure 4.16c. Stress intensity factor with time

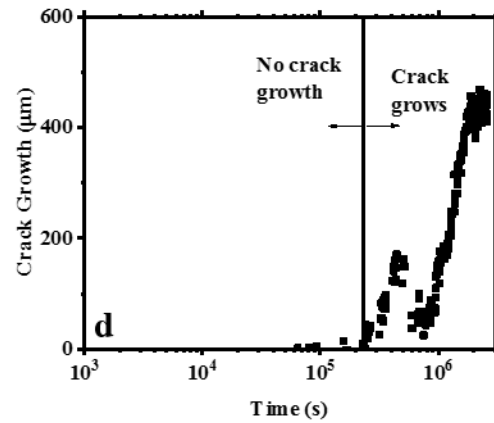


Figure 4.16d. Crack growth versus time

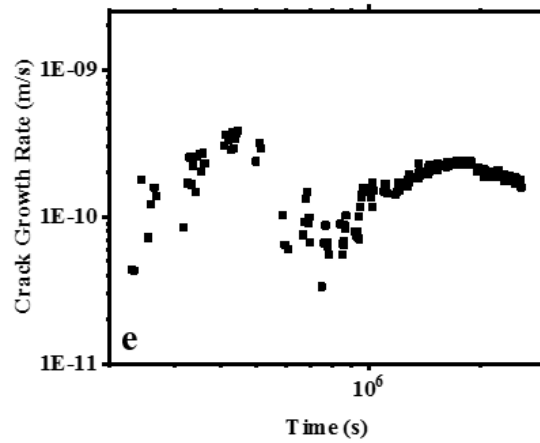


Figure 4.16e. Crack growth rate versus time for SS304L in 126 g/L NaCl solution at 39 °C.

4.4.7. Crack growth experiments on sensitized SS304H specimens in MgCl₂ solution

To inspect whether the chlorine in MgCl₂ brine is more aggressive than that in NaCl which was presumed to contribute to the higher crack growth rate in MgCl₂ brine [4], an experiment was implemented with sensitized SS304H at 60 °C in MgCl₂ brine. The specimen was fatigue pre-cracked to 700 μm and an initial stress intensity factor of 22 MPa m^{1/2} was applied. An average crack growth rate of $1.017 \times 10^{-9} \pm 1.052 \times 10^{-10}$ m/s was obtained from Fig. 4.17e which is of the same order of magnitude as that of sensitized SS304H under substitute ocean water at the same temperature of 60 °C. This suggests that temperature is the main parameter in determining the average crack growth rate. In assessing the effect of chlorine in MgCl₂ brine and NaCl on average crack growth rate, Speidel conducted the experiments at 105 °C with NaCl and 130 °C with MgCl₂ brine which resulted in the higher crack growth rate under MgCl₂ brine due apparently to its higher operating temperature [4].

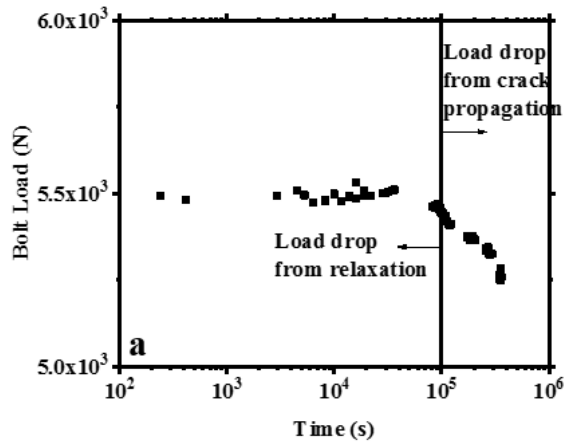


Figure 4.17a. Bolt load versus time

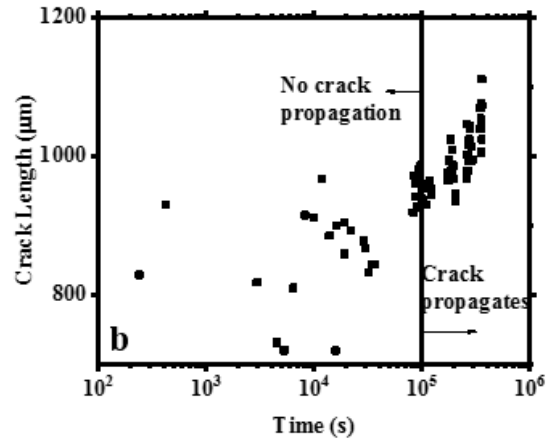


Figure 4.17b. Crack length versus time

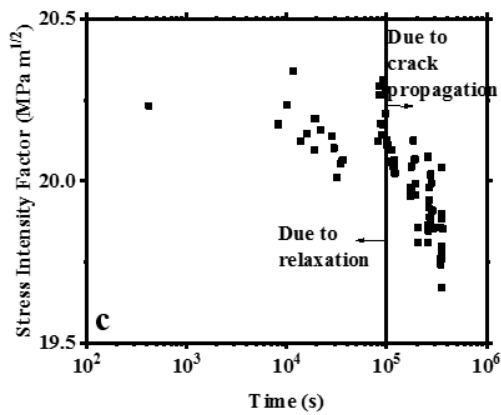


Figure 4.17c. Stress intensity factor with time

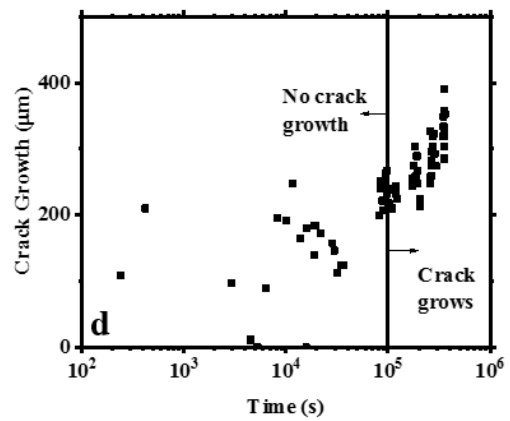


Figure 4.17d. Crack growth versus time

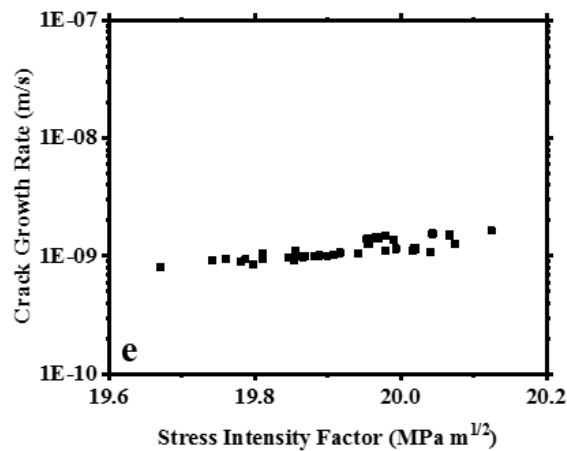


Figure 4.17e. Crack growth rate versus stress intensity factor for SS304H at 60 °C in MgCl₂.

4.4.8. Crack growth experiments with sensitized SS304H specimens in NaCl + HCl solution

An experiment was carried out with sensitized SS304H under NaCl + 3mL/L HCl solution at 60 °C to study the effect of pH on crack growth rate. The specimen had a fatigue pre-crack length of 847 μm and the experiment began with an initial stress intensity factor of 24.4 $\text{MPa m}^{1/2}$. The experimental results are shown in Figs. 4.18. An average crack growth rate of $2.146 \times 10^{-9} \pm 1.190 \times 10^{-10}$ m/s was achieved (Fig. 4.18e) from the experiment which is significantly higher than that with sensitized SS304H under substitute ocean water at 60 °C. One plausible reason for the higher average crack growth rate is the lower pH (0.9) of the solution indicating that more hydrogen exists in the solution which act as a catalyst for the crack propagation apart from the operating temperature.

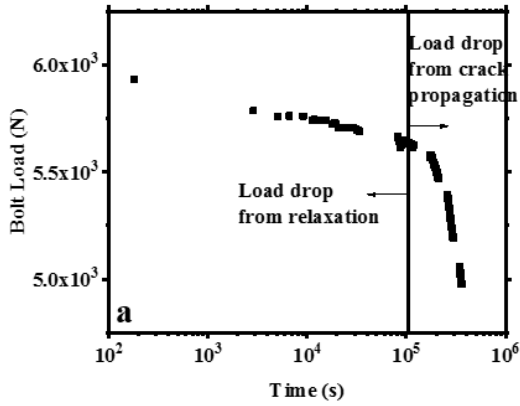


Figure 4.18a. Bolt load versus time

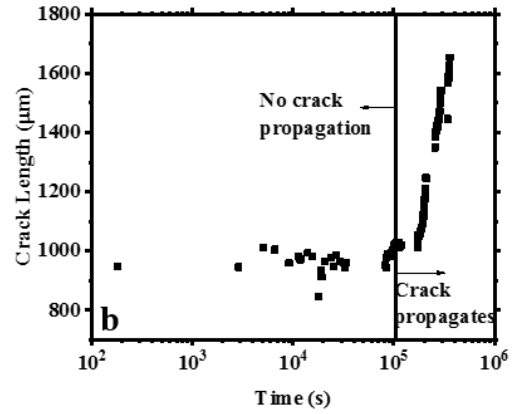


Figure 4.18b. Crack length versus time

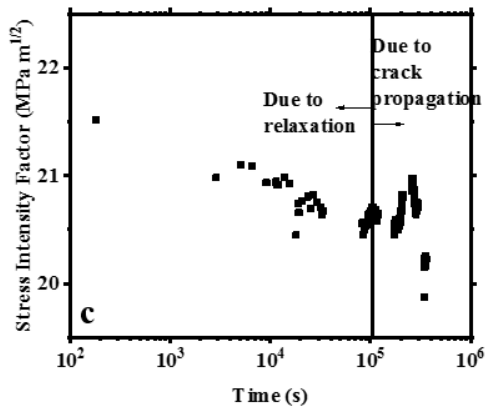


Figure 4.18c. Stress intensity factor with time

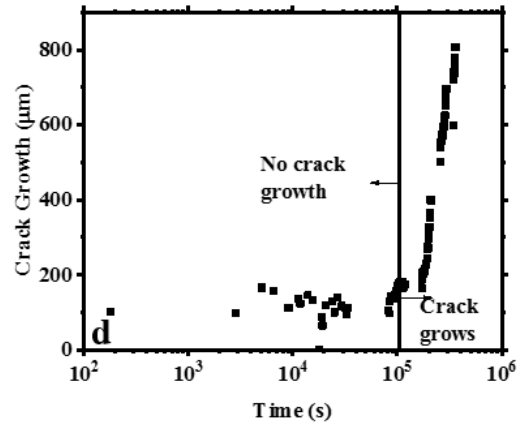


Figure 4.18d. Crack growth versus time

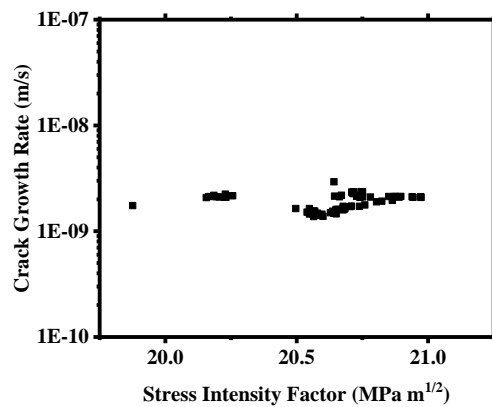


Figure 4.18e. Crack growth rate versus stress intensity factor for SS304H at 60 °C in NaCl + 3mL/L HCl solution.

4.5. Microstructural characterization following crack growth experiments

4.5.1. Microstructural characterization of non-sensitized SS304 specimens

After the crack growth experiments, the specimens were cleaned with acetone and observed under microscope for crack growth measurement. Subsequently, the specimen was etched with the same solution as mentioned previously to observe the nature of crack propagation. Although the specimens were plastically deformed during loading for the two crack growth experiments with non-sensitized SS304 material and crack growth rate could not be obtained, they were still submerged under substitute ocean water to investigate the material behavior under marine environment. After 12 days of submersion, the non-sensitized specimen exhibited pitting corrosion as observed in Fig. 4.19.

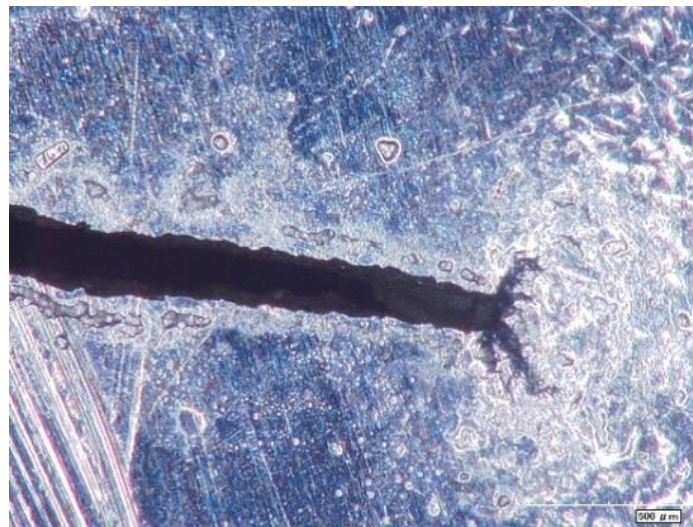


Figure 4.19. A non-sensitized SS304 specimen with pitting corrosion after submersion in marine environment.

4.5.2. Microstructural characterization of sensitized SS304H

Optical microscopy was also performed on the sensitized SS304H specimens submerged in substitute ocean water at 22 °C. Figure 4.20a illustrates that the stress corrosion cracking in marine environment does not only open the crack but also produce branching at the crack tip. Crack length measurement from the micrograph yielded a value of 1,310 μm indicating a crack growth of 413 μm (after subtracting the fatigue pre-crack length of 897 μm) while the DCPD measurement yielded a crack growth of 405 μm showing a good agreement. As noted in Fig. 4.20, crack propagation occurred intergranularly.

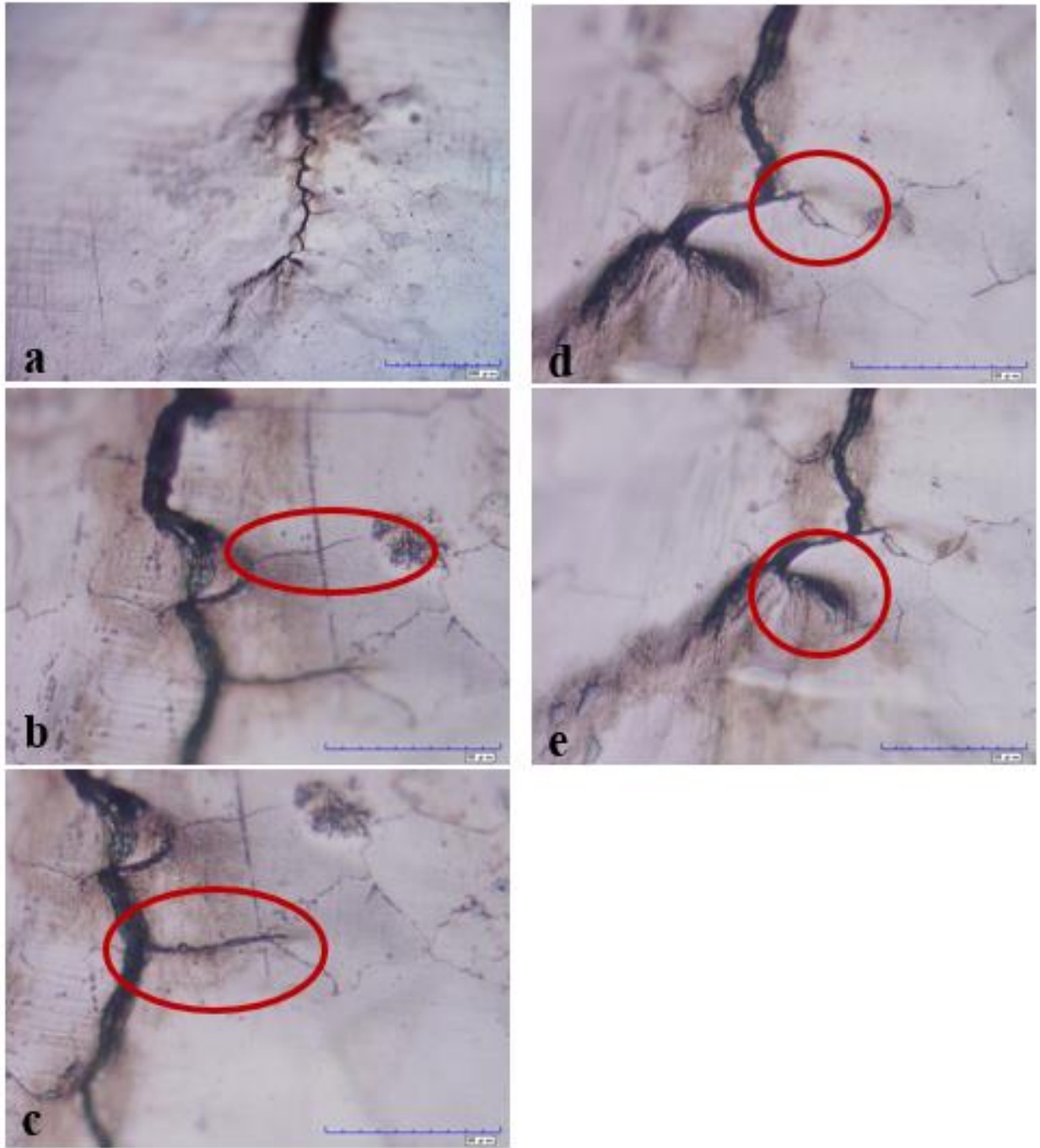


Figure 4.20. (a) Cracked sensitized SS304H and branching at the crack tip and (b)-(e) intergranular crack propagation of sensitized SS304H after submersion in marine environment at 22 °C.

The crack growth experiment of sensitized SS304H at 37 °C corroded the entire WOL specimen as illustrated in Fig. 4.21a. Crack length measurement from the micrograph yielded a value of 2,775 μm indicating a crack growth of 1,915 μm whereas the DCPD measurement yielded a crack growth of 1,840 μm again in good agreement. Observation under metallurgical microscope shows most of the cracks propagated intergranularly as displayed in Fig. 4.21c-f.

Figure 4.22a shows the condition of the sensitized SS304H WOL specimen after the submersion in substitute ocean water at 60 °C while Fig. 4.22c and d illustrate that the stress corrosion cracking in marine environment opened the crack with branching of the crack as in the previous experiments. Crack length measurement from the micrograph yielded a value of 1,377 μm as displayed in Fig. 4.22b indicating a crack growth of 642 μm (after subtracting the fatigue pre-crack length of 735 μm) while the DCPD measurement yielded a crack growth of 615 μm . Intergranular crack propagations are shown in Figs. 4.22e and 4.22f for SS304H specimen tested at 60 °C.

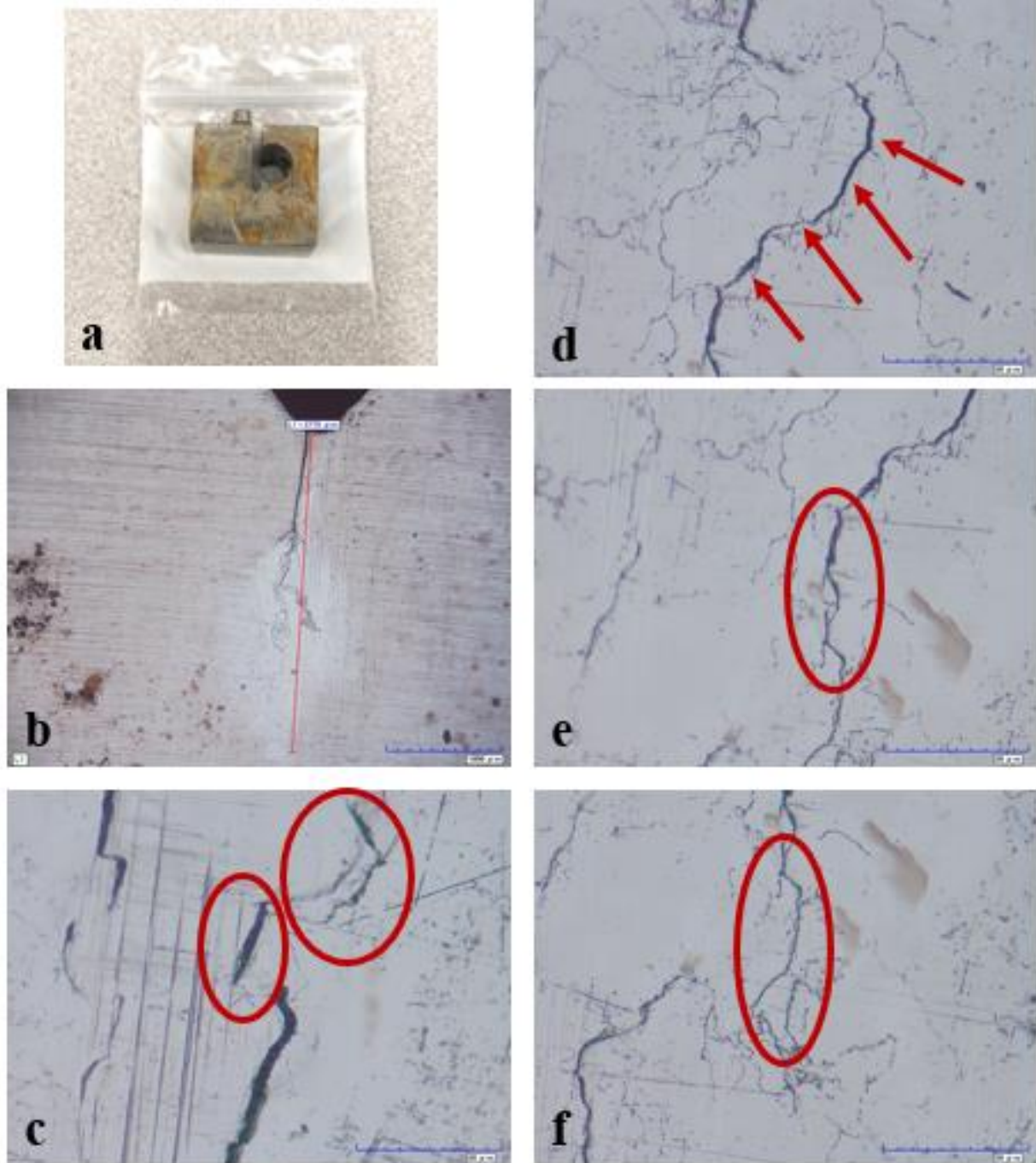


Figure 4.21. (a) A WOL specimen of sensitized SS304H after nine weeks under substitute ocean water at 37 °C, (b) crack length measurement of 2775 μm under a metallurgical microscope and (c)-(f) intergranular crack propagation of sensitized SS304H after submersion in marine environment for nine weeks at 37 °C.

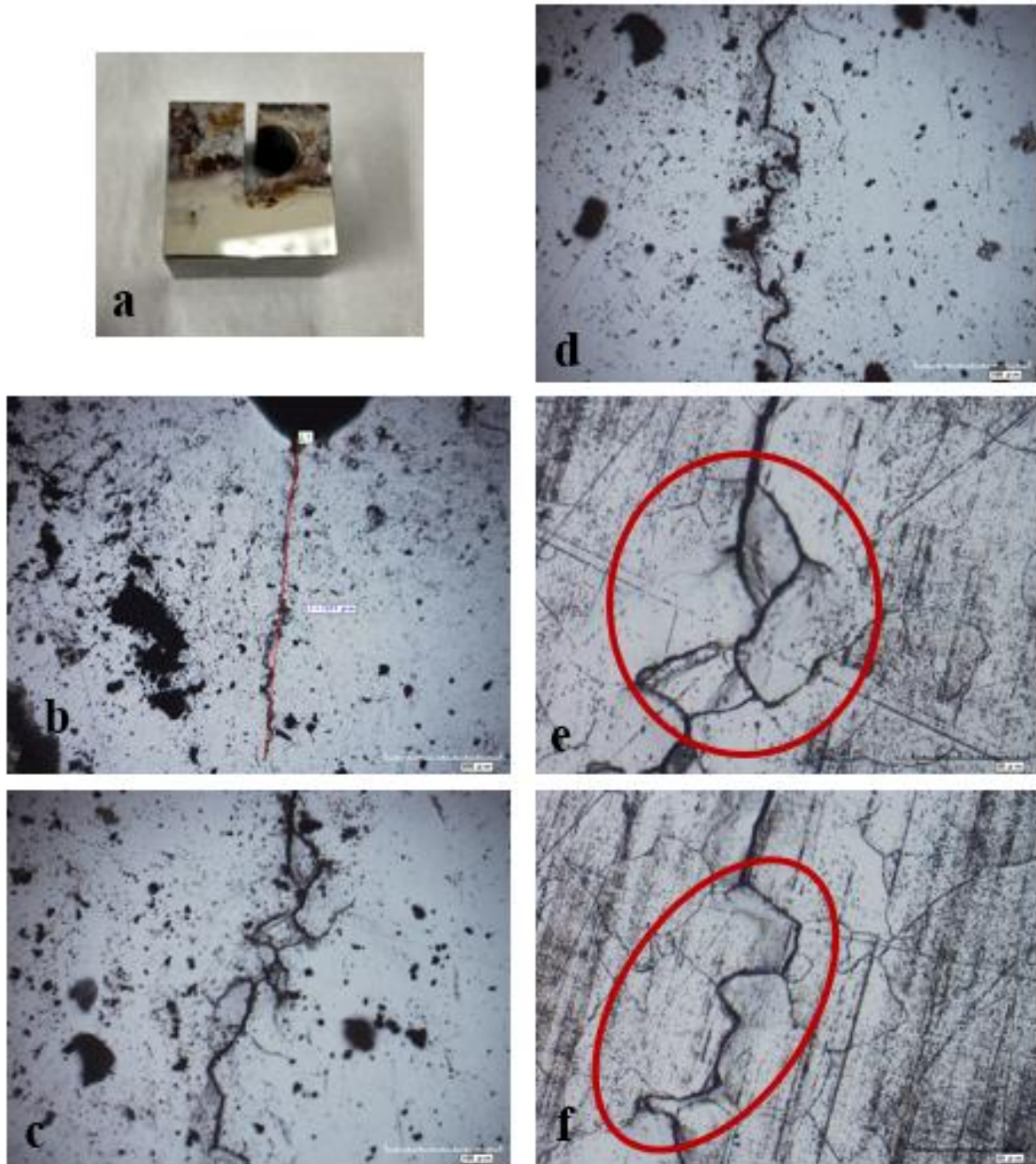


Figure 4.22. (a) Conditions of sensitized SS304H WOL specimen after the experiment under substitute ocean water at 60 °C, (b) a total crack length of 1377 μm, (c) and (d) cracked open sensitized SS304H and branching of the crack and (e) and (f) intergranular crack propagation of sensitized SS304H after submersion in substitute ocean water at 60 °C.

4.5.3. Microstructural characterization of sensitized SS304L

The crack growth experiment using sensitized SS304L in substitute ocean water at a temperature of 21 °C produces a total crack length of 1,535 μm from the micrograph as shown in Fig. 4.23a indicating a crack growth of 85 μm in agreement with the DCPD measurement of 75 μm . An intergranular crack propagation of the sensitized SS304L from the experiment is shown in Fig. 4.23b.

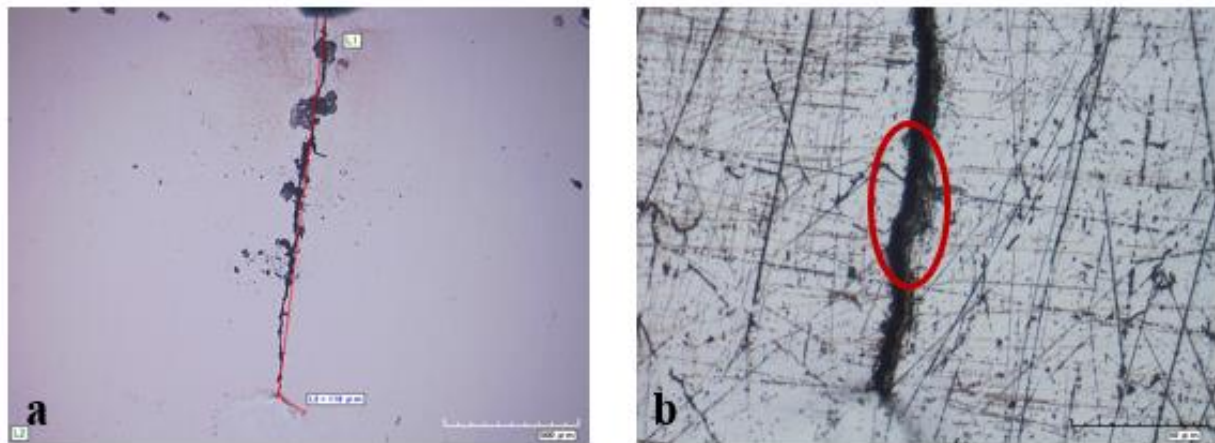


Figure 4.23. (a) A measurement of total crack length of 1535 μm and (b) intergranular crack propagation of sensitized SS304L after submersion in substitute ocean water at 21 °C.

Figure 4.24a exhibits the condition of WOL specimen after the crack growth experiment of sensitized SS304L at a temperature of 38 °C and Fig. 4.24b illustrates a crack growth of 277 μm from the micrograph which agrees well with the crack growth from the DCPD measurement of 298 μm . Figures 4.24c-f exhibit intergranular crack propagation of sensitized SS304L after submersion in substitute ocean water at 38 °C.

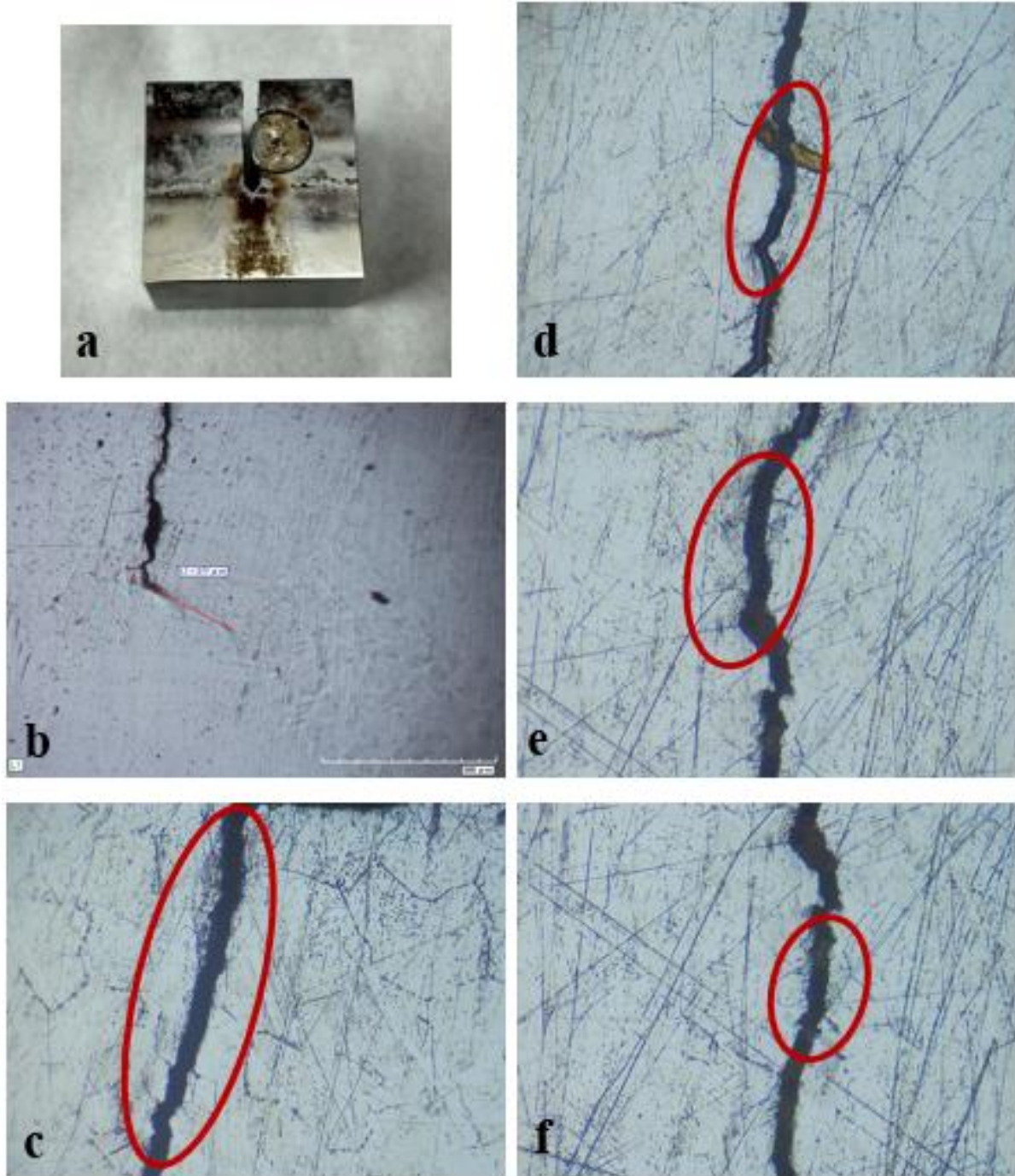


Figure 4.24. (a) Condition of WOL specimen after the experiment, (b) crack growth measurement of 277 μm using optical microscopy and (c)-(f) intergranular crack propagation of sensitized SS304L after submersion in substitute ocean water at 38 °C.

Figure 4.25a shows the condition of WOL specimen after the crack growth experiment using sensitized SS304L at a temperature of 60 °C whereas Fig. 4.25b displays the total crack length from the micrograph. Intergranular crack propagation of sensitized SS304L after the experiment is shown in Fig. 4.25c and d.

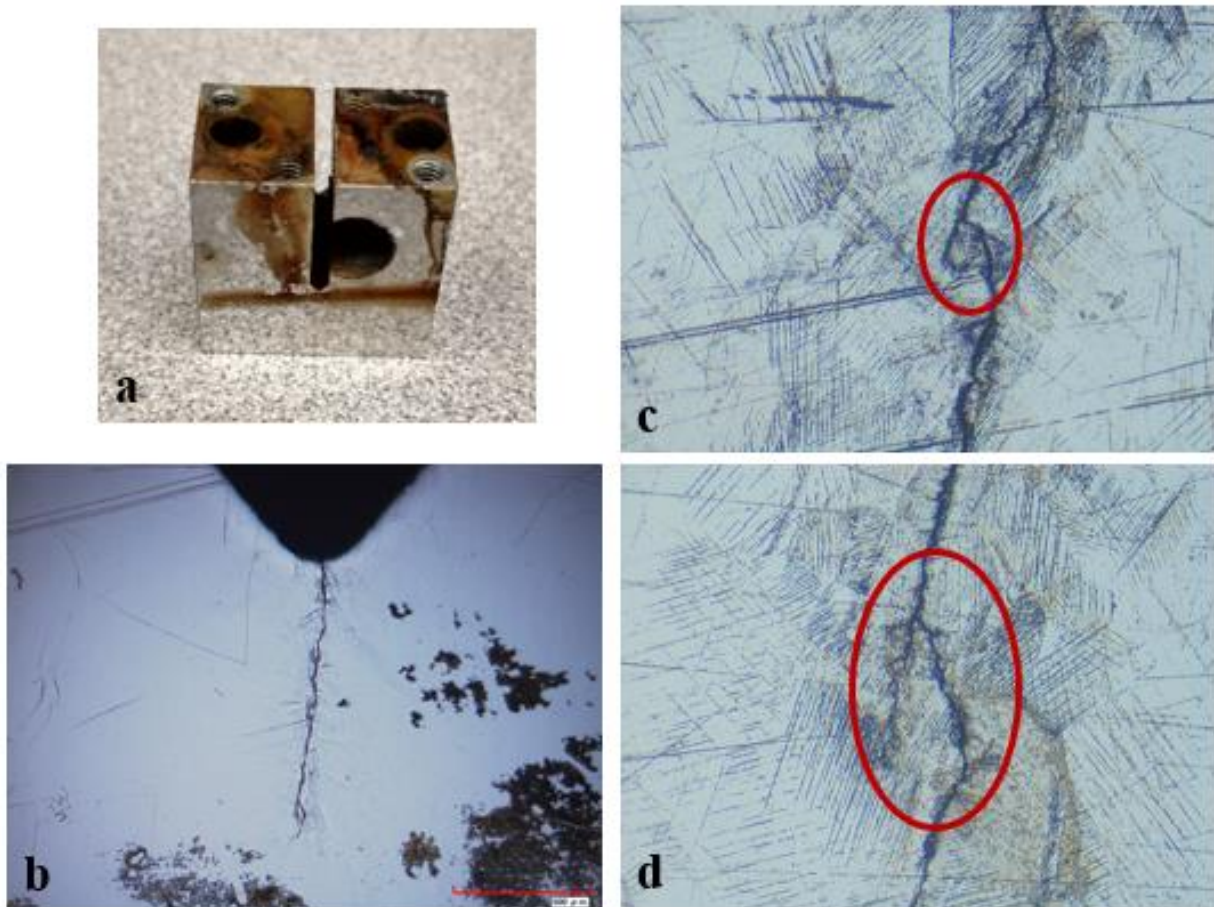


Figure 4.25. (a) Condition of sensitized SS304L WOL specimen after the experiment, (b) total crack length and (c) and (d) intergranular crack propagation of sensitized SS304L after submersion in substitute ocean water at 60 °C.

4.5.4. Microstructural characterization of sensitized SS304L in 126 g/L NaCl

The condition of WOL specimen after the crack growth experiment of sensitized SS304L at a temperature of 39 °C in 126 g/L NaCl solution is included in Fig. 4.26a while Fig. 4.26b displays a crack growth of 444 μm from the micrograph matching the crack growth from the DCPD measurement of 443 μm . Intergranular crack propagation of sensitized SS304L after the experiment is shown in Fig. 4.26c and d.

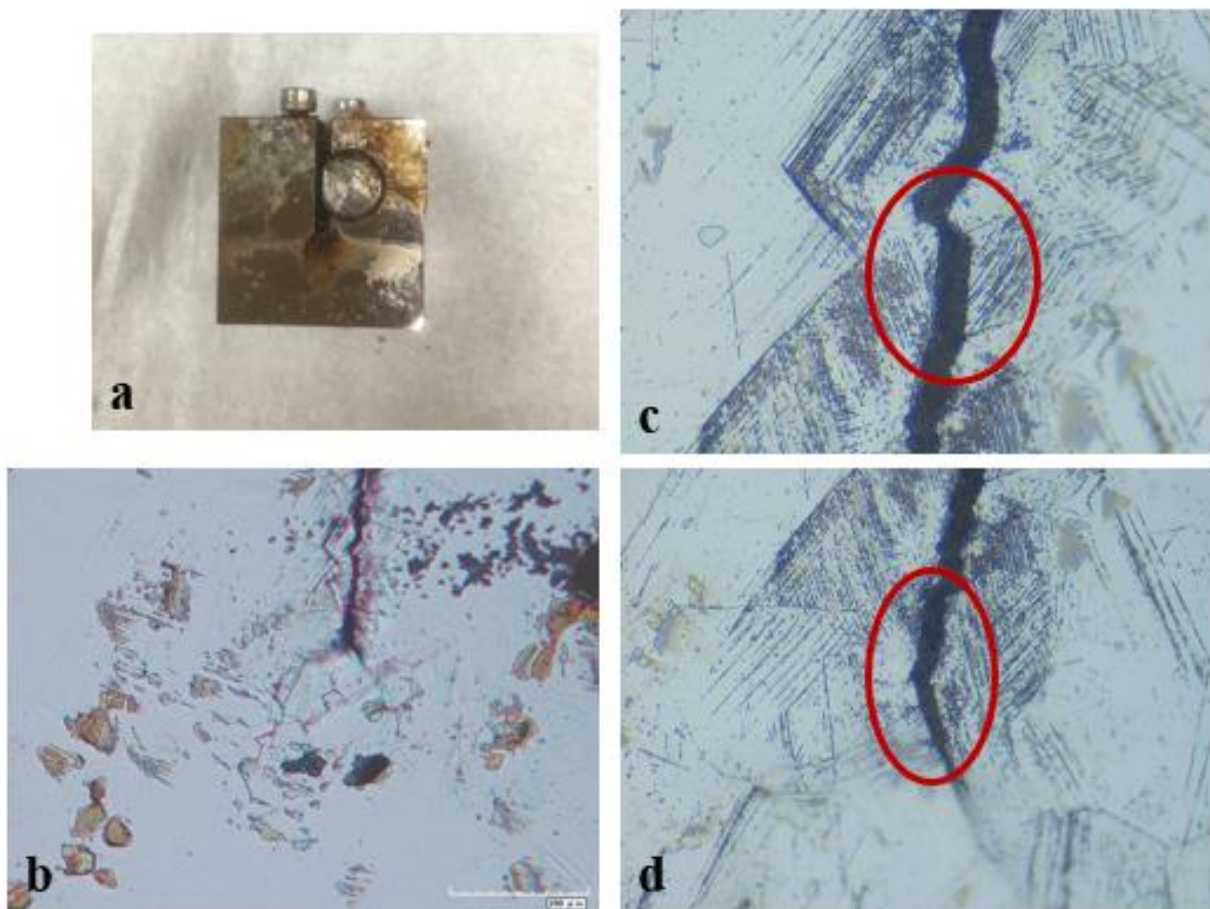


Figure 4.26. (a) Condition of sensitized SS304L WOL specimen after the experiment, (b) crack growth of 444 μm using optical microscopy and (c) and (d) intergranular crack propagation of sensitized SS304L after submersion in 126 g/L NaCl solution at 39 °C.

4.5.5. Microstructural characterization of sensitized SS304H in MgCl₂ brine

The crack growth experiment with sensitized SS304H in MgCl₂ brine at a temperature of 60 °C grew the crack by 390 μm from the micrograph as shown in Fig. 4.27a which conforms to the DCPD measurement. Intergranular crack propagation of sensitized SS304H after the experiment is shown in Fig. 4.27b-e.

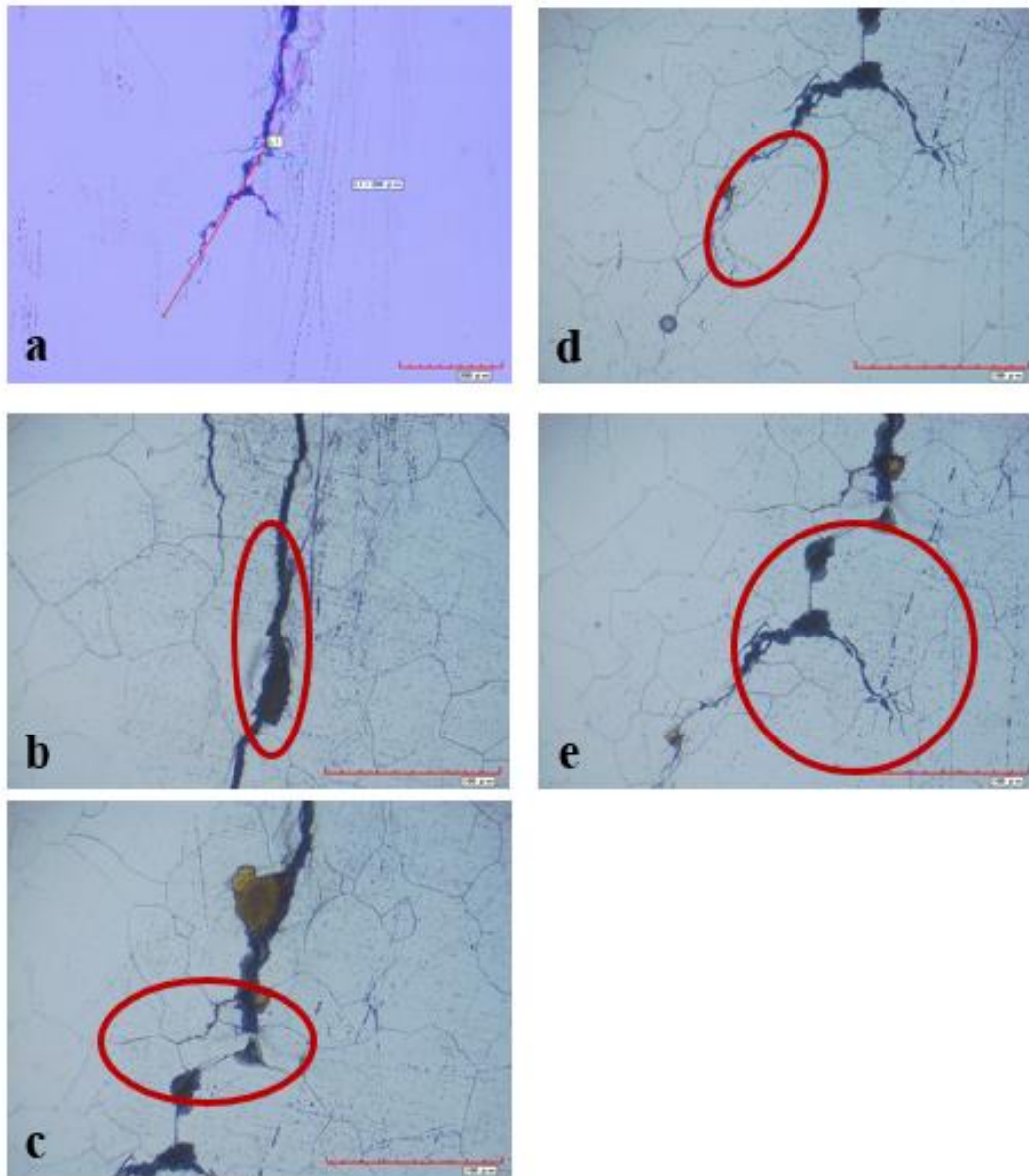


Figure 4.27. (a) A crack growth of 390 μm and (b)-(e) intergranular crack propagation of sensitized SS304H after submersion in MgCl₂ solution at 60 °C.

4.5.6. Microstructural characterization of sensitized SS304H in NaCl + HCl solution

Figure 4.28a shows the condition of WOL specimen after the crack growth experiment whereas Fig. 4.28b displays the total crack length from the micrograph. Intergranular crack propagation of sensitized SS304H after the experiment is shown in Fig. 4.28c-f. All the observed intergranular crack propagations are due to the chromium depletion along the grain boundaries [27-29].

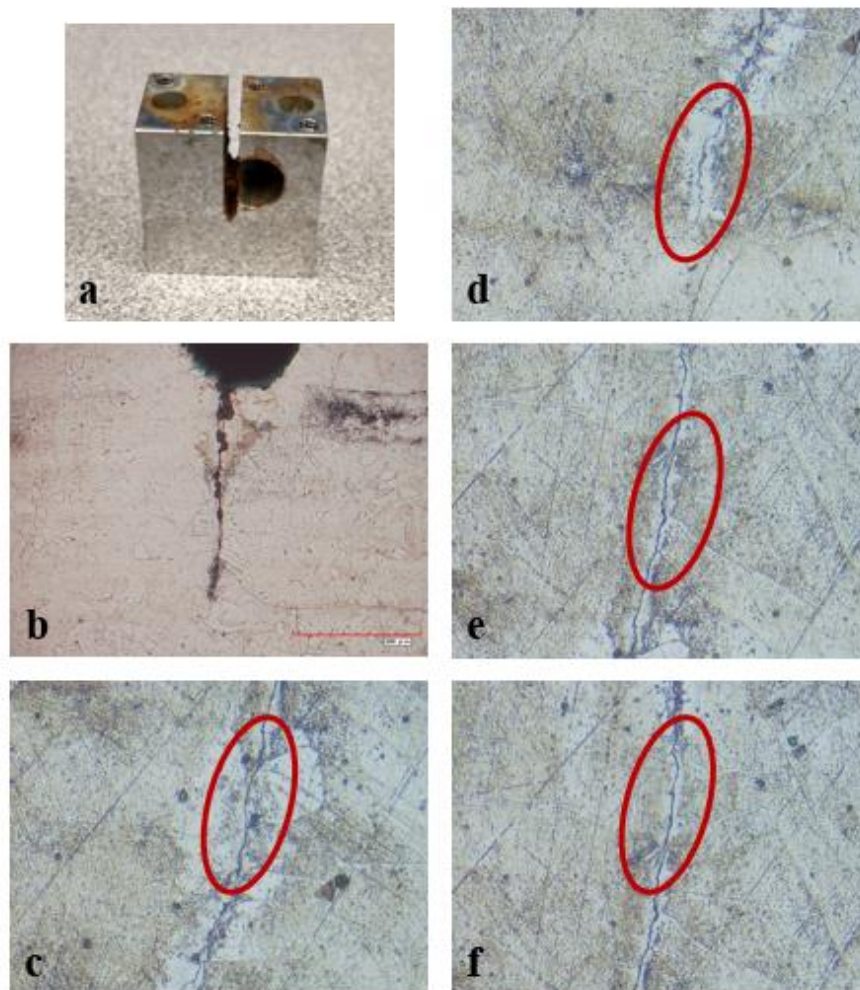


Figure 4.28. (a) Condition of sensitized SS304H WOL specimen after the experiment and (b) total crack length using optical microscopy and (c)-(f) intergranular crack propagation of sensitized SS304H after submersion in 42 g/L NaCl + 3 mL/L HCl solution at 60 °C.

4.6. References

- [1] Lake Products Company LLC, “Sea Salt,” ASTM D1141-52 Formula a, Table 1, Sec. 4.
- [2] ASTM, Standard Practice for the Preparation of Substitute Ocean Water, D1141–98. ASTM International.
- [3] C. Bryan, D. Enos, Summary of Available Data for Estimating Chloride-Induced SCC Crack Growth Rates for 304/316 Stainless Steel, Sand 2016-2922R. Sandia National Laboratories.
- [4] M.O. Speidel, Stress Corrosion Cracking of Stainless Steels in NaCl Solutions, Metall. Trans. 12A (1981) 779-789. <https://doi.org/10.1007/BF02648342>.
- [5] H.S. Khatak, J.B. Gnanamoorthy, P. Rodriguez, Studies on the Influence of Metallurgical Variables on the Stress Corrosion Behavior of AISI 304 Stainless Steel in Sodium Chloride Solution Using the Fracture Mechanics Approach, Metall. Mater. Trans. 27A (1996) 1313-1325. <https://doi.org/10.1007/BF02649868>.
- [6] A. J. Russell, D. Tromans, A Fracture Mechanics Study of Stress Corrosion Cracking of Type-316 Austenitic Steel, Metall. Trans. 10A (1979) 1229-1238. <https://doi.org/10.1007/BF02811978>.
- [7] M. R. Louthan, Jr., R. G. Derrick, Hydrogen Transport in Austenitic Stainless Steel, Corros. Sci. 15 (1975) 565-577. [https://doi.org/10.1016/0010-938X\(75\)90022-0](https://doi.org/10.1016/0010-938X(75)90022-0).
- [8] Y. Ito, M. Saito, K. Abe, E. Wakai, Effect of Hydrogen on Crack Growth Behavior in F82H Steel Using Small-Size Specimen, Small Spec. Test Tech. 6 (2015) 209-224. <https://doi.org/10.1520/STP157620140026>.
- [9] N. C. Pruitt, Jr., T. S. Sudarshan, M. R. Louthan, Jr., Influence of pH on the Crevice Corrosion and Stress Corrosion Cracking Behavior of 304 Stainless Steel, J. Mater. Eng. 10 (1988) 99-108. <https://doi.org/10.1007/BF02833866>.

- [10] R.K.S. Raman, S. Pal, A Simple Approach to the Determination of Threshold Stress Intensity for Stress Corrosion Cracking (K_{ISCC}) and Crack Growth of Sensitized Austenitic Stainless Steel, *Metall. Mater. Trans.* 42A (2011) 2643-2651. <https://doi.org/10.1007/s11661-011-0704-1>.
- [11] S. Pal, R.N. Ibrahim, R.K.S. Raman, Studying the Effect of Sensitization on the Threshold Stress Intensity and Crack Growth for Chloride Stress Corrosion Cracking of Austenitic Stainless Steel Using Circumferential Notch Tensile Technique, *Eng. Frac. Mech.* 82 (2012) 158-171.
- [12] T. Terachi, T. Yamada, T. Miyamoto, K. Arioka, SCC Growth Behaviors of Austenitic Stainless Steels in Simulated PWR Primary Water, *J. Nucl. Mater.* 426 (2012) 59-70. <https://doi.org/10.1016/j.jnucmat.2012.03.013>.
- [13] C. D. Beachem, A New Model for Hydrogen-Assisted Cracking, *Metall. Mater. Trans.* 3B (1972) 437-451. <https://doi.org/10.1007/BF02642048>.
- [14] J. Clark, The Effect of Temperature on Rate of Reaction. [https://chem.libretexts.org/Bookshelves/Physical_and_Theoretical_Chemistry_Textbook_Maps/Supplemental_Modules_\(Physical_and_Theoretical_Chemistry\)/Kinetics/Rate_Laws/Reaction_Mechanisms/Reaction_Mechanisms/The_Effect_of_Temperature_on_Rate_of_Reaction](https://chem.libretexts.org/Bookshelves/Physical_and_Theoretical_Chemistry_Textbook_Maps/Supplemental_Modules_(Physical_and_Theoretical_Chemistry)/Kinetics/Rate_Laws/Reaction_Mechanisms/Reaction_Mechanisms/The_Effect_of_Temperature_on_Rate_of_Reaction), 2019 (accessed Sep 10, 2019).
- [15] P. L. Andresen, Effects of Temperature on Crack Growth Rate in Sensitized Type 304 Stainless Steel and Alloy 600, *Corros. Sci.* 49 (1993). 714-725. <https://doi.org/10.5006/1.3316104>.
- [16] D. T. Spencer, M. R. Edwards, M. R. Wenman, C. Tsitsios, G. G. Scatigno, P. R. Chard-Tuckey, The Initiation and Propagation of Chloride-Induced Transgranular Stress-Corrosion

- Cracking (TGSCC) of 304L Austenitic Stainless Steel Under Atmospheric Conditions, Corros. Sci. 88 (2014) 76-88. <http://doi.org/10.1016/j.corsci.2014.07.017>.
- [17] S. W. Dean, Stress Corrosion – New Approaches, ASTM STP 610, ed. H. L. Craig, ASTM, (1976) 308.
- [18] L. G. Mallinson, Ageing Studies and Lifetime Extension of Materials, 1st ed., Springer Science + Business Media LLC, New York, 2001, pp. 560.
- [19] A. W. Thompson, Environment Sensitive Fracture of Engineering Materials, in: Z. A. Forouli (Ed.), AIME, Warrendale, PA, 1979, pp. 379.
- [20] F. A. Champion, Symposium on Internal Stresses in Metals and Alloys, Institute of Metals, London, 1948, p.468.
- [21] F. P. Ford, The Crack-Tip System and Its Relevance to the Prediction of Cracking in Aqueous Environments, NACE 10, EICM Proceedings, pp.139-165.
- [22] E. N. Pugh, A Post Conference Evaluation of Our Understanding of the Failure Mechanisms, in: R. W. Staehle et al. (Eds.), Stress Corrosion Cracking and Hydrogen Embrittlement of Iron Base Alloys, NACE 5, Houston, TX (1977) pp. 37-51.
- [23] Z. Szklarska-Smialowska, Various Forms of Localized Corrosion Common Features and Differences, NACE 5 (1977) 30-36.
- [24] O. M. Alyousif, R. Nishimura, The Stress Corrosion Cracking Behavior of Austenitic Stainless Steels in Boiling Magnesium Chloride Solution, Corros. Sci. 49 (2007) 3040-3051. <https://doi.org/10.1016/j.corsci.2006.12.023>.
- [25] K. van Gelder, J. G. Erlings, J. W. M. Damen, A. Visser, The Stress Corrosion Cracking of Duplex Stainless Steel in H₂S/CO₂/Cl⁻ Environments, Corros. Sci. 27 (1987) 1271-1279. [https://doi.org/10.1016/0010-938X\(87\)90114-4](https://doi.org/10.1016/0010-938X(87)90114-4).

- [26] B. F. Brown, Stress Corrosion Cracking Control Measures, First, U.S. Government Printing Office, Washington, 1977.
- [27] V. Kumar, P. Joshi, S. Dhakar, Analysis of the Effect of Sensitization on Austenitic Stainless Steel 304L Welded by GTAW Process, IJTIR 14 (2015).
- [28] S. Ghosh, V. Kain, A. Ray, H. Roy, S. Sivaprasad, S. Tarafder, K. K. Ray, Deterioration in Fracture Toughness of 304LN Austenitic Stainless Steel Due to Sensitization, Metall. Mater. Trans. 40A (2009) 2938-2949. <https://doi.org/10.1007/s11661-009-0023-y>.
- [29] S. F. Hasan, S.I.J. Alrubaiey, Effect of Sensitization on Microhardness and Corrosion Resistance of Austenitic Stainless Steel, IJOCAAS 2 (2017).

CHAPTER 5: CONCLUSIONS AND FUTURE WORK

The average crack growth rates of all the conducted experiments are summarized in Table 5.1, and the comparison of crack growth measurement using DCPD technique and optical microscopy are displayed in Table 5.2.

Based on the conducted experiments, it can be concluded that:

1. From the experiments using sensitized SS304H and sensitized SS304L at 22, 37 and 60 °C, activation energies of 60.9 ± 0.62 and 69.1 ± 8.96 kJ/mol are obtained from the crack growth rates respectively indicating that hydrogen diffusion controls the SCC crack propagation in iron and steels whereas activation energies of 61.02 ± 5.97 and 43.54 ± 0.77 kJ/mol are obtained from the crack initiation time respectively indicating chloride ion diffusion controls crack initiation.
2. Hydrogen embrittlement is the main mechanism for stress corrosion cracking with temperature being the main important parameter as it governs the hydrogen propagation for crack growth as shown in Fig. 5.1 and chloride transport to the crack tip for crack initiation in Fig. 5.2.
3. The threshold stress intensity factor (K_{ISCC}) of sensitized SS304H under substitute ocean water at 37 °C is $15 \text{ MPa m}^{1/2}$, and therefore, its J_{ISCC} is 1023.75 J/m^2 .
4. Reducing carbon concentration in SS304L increases the corrosion resistance and thus, lowers the crack growth rate.
5. Increasing salt concentration does not significantly increase the crack growth rate in sensitized SS304L (6.13 vs 6.26 mm/yr); therefore, salt concentration does not affect the crack growth rate in sensitized SS304L.

6. However, increasing salt concentration makes the cracks initiate slightly earlier (68.6 vs 64.5 hrs) in sensitized SS304L; thus, salt concentration influences crack initiation in sensitized SS304L where the higher the salt concentration, the faster is the crack initiation.
7. DCPD technique is suitable for monitoring load changes and crack growth during SCC experiments.
8. Microstructural characterization after the experiments for the sensitized specimens indicates that cracks propagate intergranularly due to the chromium depletion by forming carbides ($M_{23}C_6$) along the grain boundaries.

Table 5.1. Summary of crack growth experiments.

Specimen	Temp (°C)	Environment	pH	Salt Conc. (g/L)	Average da/dt (m/s)	Average da/dt (mm/year)	Crack Initiation (hrs)
304H	22.0 ± 0.6	Substitute ocean water	8.2	42	0.975 x 10 ⁻¹⁰ ± 9.528 x 10 ⁻¹²	3.07 ± 0.30	310.5
	37.2 ± 0.9				3.258 x 10 ⁻¹⁰ ± 9.551 x 10 ⁻¹¹	10.27 ± 3.01	75.7
	60.3 ± 0.5				1.580 x 10 ⁻⁹ ± 2.593 x 10 ⁻¹⁰	49.83 ± 8.18	18.5
304L	21.4 ± 0.7				3.064 x 10 ⁻¹¹ ± 4.009 x 10 ⁻¹²	0.97 ± 0.13	186.5
	38.4 ± 0.7				1.945 x 10 ⁻¹⁰ ± 1.315 x 10 ⁻¹¹	6.13 ± 0.42	68.6
	60.2 ± 0.2				8.830 x 10 ⁻¹⁰ ± 9.863 x 10 ⁻¹¹	27.85 ± 3.11	23.5

Table 5.1 (continued).

304L	39.0 ± 0.8	NaCl		126	1.985 x 10⁻¹⁰ ± 2.603 x 10⁻¹¹	6.26 ± 0.82	64.5
304H	60.8 ± 1.1	MgCl₂		6.1 mol/kg	1.017 x 10⁻⁹ ± 1.052 x 10⁻¹⁰	32.07 ± 3.32	27.7
304H	60.1 ± 0.5	NaCl + HCl	0.9	42	2.146 x 10⁻⁹ ± 1.190 x 10⁻¹⁰	67.68 ± 3.75	28.7

Table 5.2. Comparison of crack growth values from DCPD technique and optical microscopy

Specimen	Temp (°C)	Environment	pH	Salt Conc. (g/L)	Crack Growth DCPD (µm)	Crack Growth Optical Microscopy (µm)	Difference (%)
304H	22.0 ± 0.6	Substitute ocean water	8.2	42	405	413	1.94
	37.2 ± 0.9				1840	1915	3.92
	60.3 ± 0.5				615	642	4.21
304L	21.4 ± 0.7				75	85	11.76
	38.4 ± 0.7				298	277	7.58
	60.2 ± 0.2				402	367	9.54
304L	39.0 ± 0.8	NaCl		126	443	444	0.07
304H	60.8 ± 1.1	MgCl₂		6.1 mol/kg	390	353	9.49
304H	60.1 ± 0.5	NaCl + HCl	0.9	42	807	760	6.18

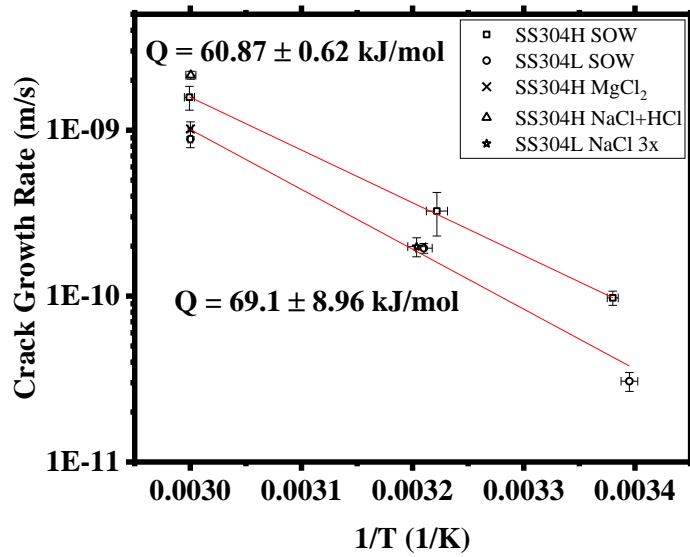


Figure 5.1. Crack growth rate versus inverse temperature for sensitized SS304H and sensitized SS304L under different environments.

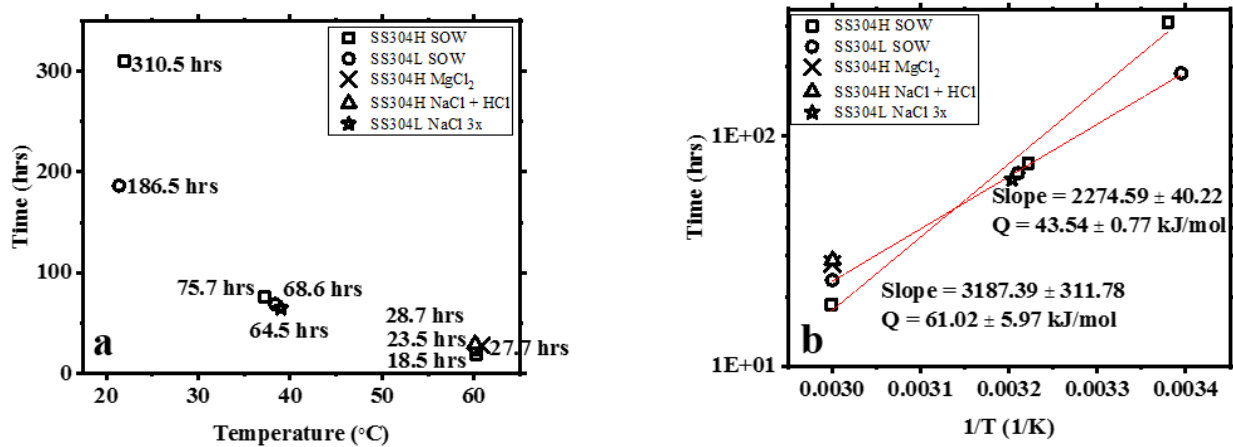


Figure 5.2 (a) Crack initiation time with temperature and **(b)** Arrhenius plot of crack initiation time for sensitized SS304H and sensitized SS304L under different environments.

FUTURE WORK

The following crack growth experiments are suggested:

1. Sensitized SS304H under substitute ocean water or NaCl solution at higher concentrations such as at 126 g/L at 40 °C to determine the effect of salt concentration on average crack growth rates and/or crack initiation times of sensitized SS304H.
2. Sensitized SS304H and L under MgCl₂ brine at different temperatures (22, 40 and 60 °C) to determine the activation energy from their average crack growth rates as a function of inverse temperature.
3. Sensitized SS304H and L under substitute ocean water or NaCl solution with different pH levels to assess the effect of pH on average crack growth rates, crack initiation time or other factors.
4. Sensitized SS304H and L of several different degrees of sensitization under substitute ocean water at varied temperatures such as at 22, 40 and 60 °C. Such experiments can give useful information on the effect of degree of sensitization on the following but not limited to average crack growth rates, crack initiation time and activation energy.

ACKNOWLEDGMENTS

I would like to thank Scott Gordon from Colorado School of Mines for providing the SS304 plates, Chris Sanford for fabricating the WOL specimens, Dr. Harvey West for the assistance during fatigue pre-crack experiments and the use of the microscopes Ervin Miller for helping me with cables and electrical equipments. We also would like to extend our appreciation to Prof. Zeev Shayer from Colorado School of Mines and Dr. Charles Bryan from Sandia National Laboratory for the discussions about the experiment. This work was supported by NEUP IRP, “Innovative Approach to SCC Inspection and Evaluation of Canister in Dry Storage.”

APPENDICES

Appendix A

Publications and presentations

Publications:

- [1] **L. Tjayadi**, N. Kumar and K. L. Murty, Fracture Mechanics-Based Study of Stress Corrosion Cracking of SS304 Dry Storage Canister for Spent Nuclear Fuel, TMS. Mar 2019. San Antonio, TX.
- [2] **L. Tjayadi**, N. Kumar and K. L. Murty, Understanding Stress Corrosion Cracking Behavior of Austenitic Stainless Steel SS304 for Dry Storage Canisters in Simulated Sea-water, TMS. Feb 2020. San Diego, CA.

Presentations:

- [1] **L. Tjayadi**, N. Kumar and K. L. Murty, Fracture Mechanics-Based Study of Stress Corrosion Cracking of SS304 Dry Storage Canister for Spent Nuclear Fuel, TMS. Mar 2019. San Antonio, TX.
- [2] N. Kumar, **L. Tjayadi** and K. L. Murty, Stress Corrosion Cracking Behavior of Austenitic Stainless Steel SS304 for Dry Storage Canisters in Simulated Sea-water, TMS. Feb 2020. San Diego, CA.

Appendix B

Fracture Mechanics-Based Study of Stress Corrosion Cracking of SS304 Dry Storage Canister for Spent Nuclear Fuel

Fracture Mechanics-Based Study of Stress Corrosion Cracking of SS304 Dry Storage Canister for Spent Nuclear Fuel



Leonardi Tjayadi, Nilesh Kumar and Korukonda L. Murty

Abstract Many independent spent fuel storage installations (ISFSI) are located along the coastal regions in the US and the dry storage canisters consisting of spent nuclear fuels are envisioned to undergo chloride-induced stress corrosion cracking (SCC) in heat-affected zone. In the present study, we have investigated SCC behavior of sensitized SS304H under substitute ocean water at room temperature using wedge opening loading (WOL) specimens. The alloy was sensitized at 600 °C for 215 h followed by microstructural characterization. The crack growth during the test was monitored using direct current potential drop technique. The crack growth rate for the SS304H alloy was within the same order of magnitude as reported in literature for SS304 alloy under chloride environment.

Keywords Crack growth · Fatigue pre-cracking · Fracture mechanics · Potential drop · SCC · Stainless steel

Introduction

The spent nuclear fuels (SNF) in the U.S. after being removed from the reactor are submerged in spent fuel pools at reactor facilities for at least 5 years before being transferred to dry storage facilities at independent spent fuel storage installations (ISFSI). At ISFSI, SNFs are stored in horizontal and/or vertical dry casks canisters that are typically made of austenitic stainless steel (SS) types 304 and 316 encapsu-

L. Tjayadi
Department of Nuclear Engineering, NC State University, Raleigh, NC, USA
e-mail: ltjayad@ncsu.edu

N. Kumar (✉)
Metallurgical and Materials Engineering, The University of Alabama, Tuscaloosa, AL, USA
e-mail: nkumar@eng.ua.edu

K. L. Murty
Nuclear Engineering, NC State University, Raleigh, NC, USA
e-mail: murty@ncsu.edu

© The Minerals, Metals & Materials Society 2019
The Minerals, Metals & Materials Society (ed.), *TMS 2019 148th Annual Meeting & Exhibition Supplemental Proceedings*, The Minerals, Metals & Materials Series, https://doi.org/10.1007/978-3-030-05861-6_106

1089

ltjayad@ncsu.edu

lated in a larger concrete overpack equipped with air ventilation for natural cooling. The air ventilation for natural cooling enables exposure of the dry canister to ambient site conditions of the spent fuel storage facilities that are usually located near the ocean [1]. In several locations in the U.S., the atmospheric seacoast conditions have high concentration of chloride salts that get deposited on the dry storage canisters through the concrete ventilation leading to possible chloride-induced stress corrosion cracking (CISCC) [2, 3].

Electric Power Research Institute (EPRI) performed a study on the degradation mode of materials in ISFSI and listed, among many, CISCC as potential degradation mode for the canisters [4]. With the proximity of the ISFSI to the ocean in the US, CISCC poses a big issue in stainless steel dry canisters. Canister inspections by EPRI and Sandia National Laboratories indicated that chloride salts were found on the canister surface at the ISFSI near marine environments [5–7]. Considering the halt of Yucca Mountain Nuclear Waste Repository [8] and nuclear waste reprocessing facility projects for nonproliferation issues, the importance of dry storage facilities at ISFSI has become greater.

One way to investigate SCC to evaluate the structural lifetime is by applying fracture mechanics-based approach to determine the crack growth in a corrosive environment. Many studies have been carried out on the SCC of austenitic stainless steel but they were under different solution and/or environmental conditions. Alyousif and Nishimura conducted SCC experiment of austenitic SS in boiling magnesium chloride (MgCl_2) solutions [9], whereas Raman and Pal performed SCC experiment of sensitized austenitic SS in MgCl_2 at 154 °C [10]. Speidel [11] conducted SCC study in NaCl solution at room temperature and reported an average crack growth rate of 10^{-10} m/s. Khatak et al. utilized a boiling NaCl solution in an acidic environment [12]. More experimental work is needed on SCC in salt composition close to marine salt at room temperature to understand SCC phenomenon of SS used in storage canisters. We present here crack growth experiments under substitute ocean water at room temperature with a wedge opening loading (WOL) specimen to investigate the SCC behavior of SS304H.

Experimental Procedure

Material

The SS304H material was received from the Colorado School of Mines in sensitized condition (600 °C for 215 h) and the chemical composition is given in Table 1. In this condition, the SS304H has yield strength of 302 ± 11 MPa, ultimate tensile strength of 701 ± 14 MPa, uniform elongation of $80.8 \pm 5.3\%$ and total elongation of $92.4 \pm 4.6\%$.

Table 1 Chemical composition (wt%) of SS304H [13]

C	0.0418	Cu	0.4005	N	0.0844	S	0.0010
Co	0.1345	Mn	1.7495	Ni	8.0725	Si	0.2930
Cr	18.1930	Mo	0.2985	P	0.0335	Fe	Balanced

Microstructural Characterization

Prior to the crack growth experiment, the SS304H material was mechanically polished down to the mirror finish and etched with a solution of hydrochloric acid, nitric acid and water of equivalent ratio, and cleaned with methanol and deionized water for metallography. The energy dispersive spectroscopy (EDS) in scanning electron microscope (SEM) was used to detect the distribution of different elements among different phases present in the alloy. After the crack growth experiment, the specimen was cleaned with acetone and observed under micrograph for crack growth measurement. Subsequently, the specimen was etched with the same solution to observe the nature of crack propagation.

Stress Corrosion Cracking

Fatigue Pre-cracking

WOL specimens were fatigue pre-cracked (following ASTM standards E399-12 [14], E1820-15 [15], and E1681-03 [16]) using a fatigue machine from TestResources model 910LX15 (Fig. 1) to produce the desirable sharpness. The fatigue pre-cracking was carried out under sinusoidal cyclic loading at a load ratio of 0.1 with a maximum force of 4.5 kN for 321,000 cycles, 5 kN for 100,000 cycles, 5.5 kN for 100,000 cycles and 6 kN for 28,000 cycles. One face of the WOL specimen was mechanically polished with final polishing at 50 nm diamond suspension before the fatigue pre-crack experiment to observe the crack nucleation and propagation. The dimensions of the WOL specimen in inches are shown in Fig. 2a and the WOL specimen is included in Fig. 2b.

Direct Current Potential Drop Technique for Crack Size Measurement

Fracture mechanics-based SCC study involves monitoring of load, load line displacement (or crack mouth opening displacement), and crack length with time. There are many ways by which crack length can be monitored—optical microscopy, scanning electron microscopy, replication, potential difference, and ultrasonic. Due to its simplicity, the direct current potential drop (DCPD) technique has been widely used

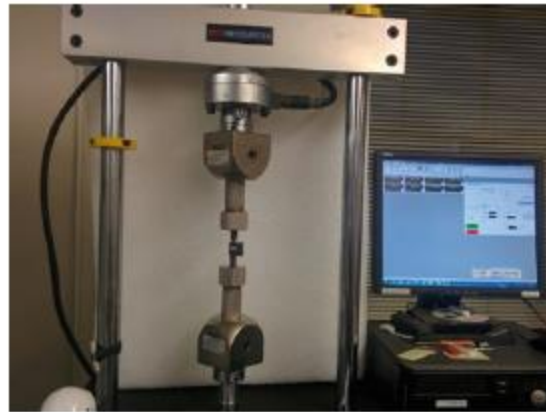


Fig. 1 Fatigue pre-cracking experimental setup

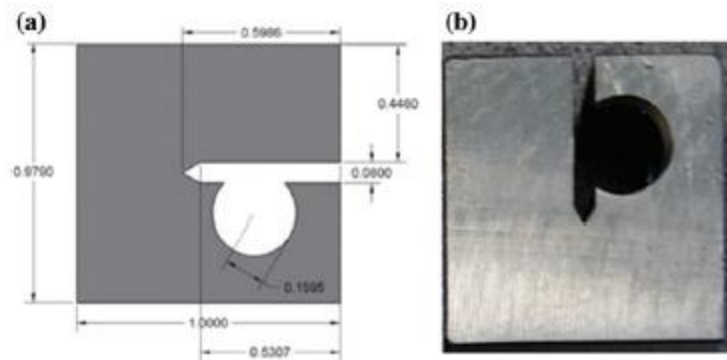


Fig. 2 **a** Drawing of WOL specimen in inches and **b** A photo of a WOL specimen

for detecting crack initiation and monitoring its growth. This technique involves supplying a constant current through the specimen and measuring potential drop as crack propagates. Once a fatigue pre-crack was produced at the tip of the notch, the pre-cracking was stopped and the crack length was measured using an optical microscope as well as the DCPD measurement using the setup shown in Fig. 3a consisting of a direct current supply unit (Kikushi, PAT160-50T) and a nanovoltmeter (Keithley 2182A). Then, the same procedure was repeated several more times in air and in substitute ocean water to obtain several data points to construct a calibration curve between the crack length and potential drop (Fig. 3c). A crack growth experiment was conducted for 6 weeks by submerging the WOL specimen in the substitute ocean water (Table 2) and loaded with an instrumented bolt as shown in Fig. 3b while monitoring the potential drop for crack growth. A load of 1875 lbf

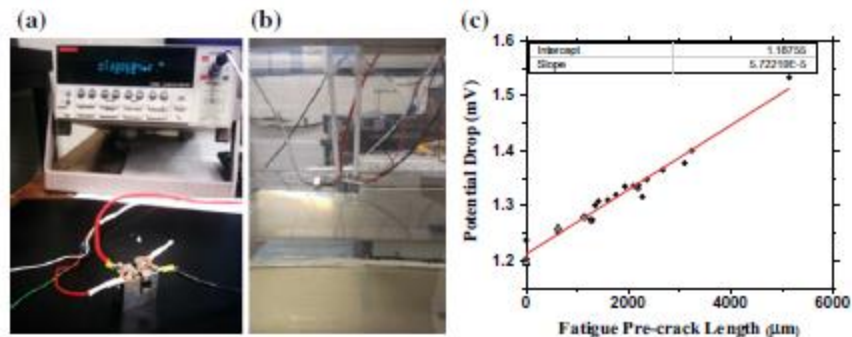


Fig. 3 a The DCPD setup to measure potential drop, b A WOL specimen submerged in substitute ocean water during crack growth experiment and c Calibration chart of potential drop

Table 2 Chemical composition of the substitute ocean water [17]

Compound	NaCl	MgCl ₂	Na ₂ SO ₄	CaCl ₂	KCl	NaHCO ₃	KBr	H ₃ BO ₃	SrCl ₂	NaF
Concentration (g/l.)	24.53	5.20	4.09	1.16	0.695	0.201	0.101	0.027	0.025	0.003

was applied at the beginning of the experiment to achieve an initial stress intensity factor of $30 \text{ MPa m}^{1/2}$. For prediction of crack length, a calibration curve (Fig. 3c) is developed for the specimen under consideration.

Results and Discussion

Microstructural Characterization of As-Received Sample

The microstructure of the as-received sample is shown in Fig. 4a and the elements present in the SS304H material are shown in Fig. 5b following energy dispersive spectroscopy (EDS).

Crack Growth During Stress Corrosion Cracking

The fatigue pre-cracking was done at a load ratio of 0.1 with varying maximum force that produced a pre-crack of nearly $900 \mu\text{m}$ length (Fig. 5). The variation of instrumented bolt load with time in Fig. 6a suggests that crack did not propagate until 2 weeks into the experiment as there is only a small drop in the applied load due to the relaxation of the instrumented bolt. After 2 weeks, the load dropped rapidly reaching half of its initial value towards the end of the experiment implying stress

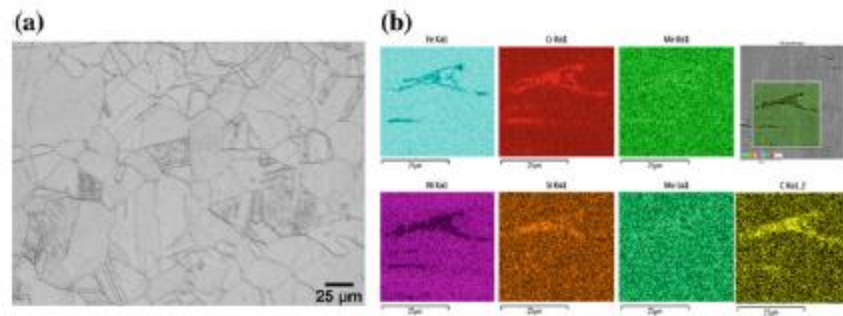


Fig. 4 **a** Micrograph of as-received SS304H and **b** Elements identified from the EDS of SS304H

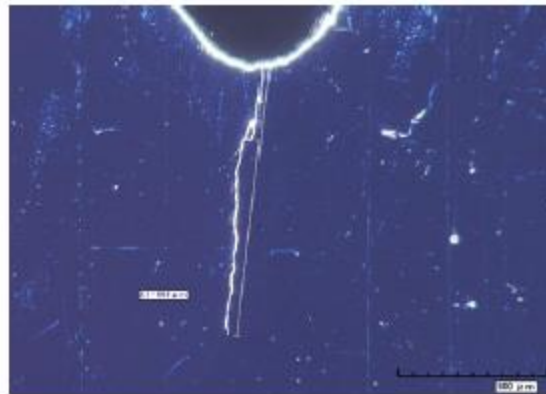


Fig. 5 Fatigue pre-crack of WOL SS304H specimen

corrosion cracking and crack propagation occurred since then. By considering that the crack propagation occurred after 400 h, the average crack growth rate for SS304H at room temperature under marine environment is found to be $0.975 \times 10^{-10} \pm 9.528 \times 10^{-12}$ m/s. As a comparison, for a sensitized SS304 at a room temperature of 22 °C, Speidel reported a crack growth value of 1.438×10^{-10} m/s [18]. The variation of stress intensity factor as a function of crack extension presented in Fig. 6b shows the decrease in the stress intensity factor from the initial value of 30 to 25 MPa m^{1/2} is most likely due to the load relaxation in first two weeks and from 25 to below 15 MPa m^{1/2} due to a sharp decrease in applied load due to increase in crack length.

Microstructural Characterization After the SCC Experiment

Optical microscopy was performed on the WOL specimen and Fig. 7a, b illustrates that the stress corrosion cracking in a marine environment does not only open the

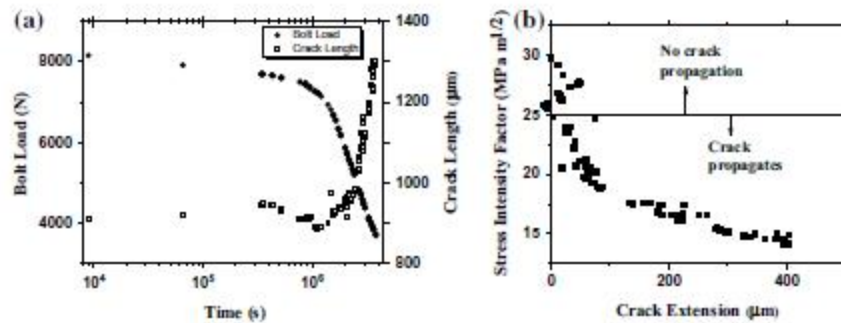


Fig. 6 a Time variation of load from instrumented bolt and b Stress intensity versus crack length

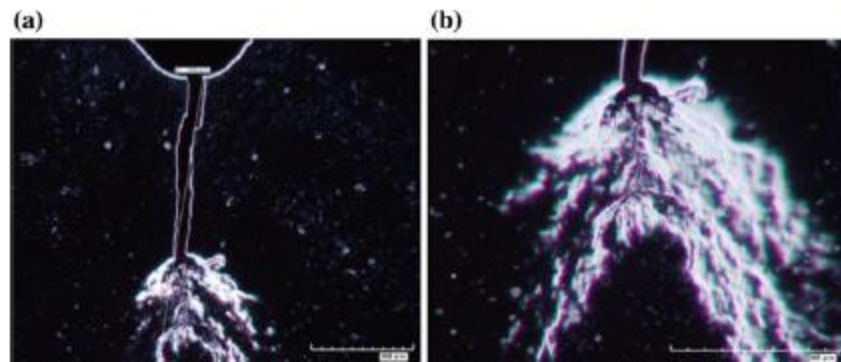


Fig. 7 a Cracked WOL specimen post-SCC and b Crack branching at the crack tip

crack but also produce branching at the crack tip. Crack length measurement from the micrograph yielded a value of 1300 μm indicating a crack growth of 400 μm (after subtracting the fatigue pre-crack length) throughout the experiment. The DCPD measurement yielded a crack growth of 405 μm which is in good agreement with the crack length measured using the optical microscope.

Conclusions

Stress corrosion cracking of dry storage canisters for spent nuclear fuel storage was investigated by performing crack growth experiment on WOL specimen made of SS304H under substitute ocean water at room temperature. Before starting the crack growth experiment, a WOL specimen was fatigue pre-cracked to different lengths and their corresponding potential drop values were monitored after each fatigue pre-crack using a DCPD technique to establish a calibration chart. Another WOL

specimen was fatigue pre-cracked close to 900 μm for the crack growth experiment and submerged in the marine environment at room temperature for 6 weeks. Crack growth was observed after 2 weeks (400 h) from the start of the experiment and an average crack growth rate of 0.975×10^{-10} m/s was noted in SS304H at room temperature. The optical microscope and SEM were used to measure the crack length after the SCC experiment. The micrographs of the SCC fractured sample revealed that the crack propagated intergranularly.

Acknowledgements We would like to thank Scott Gordon from Colorado School of Mines for providing the SS304 plates, Chris Sanford for manufacturing the WOL specimens, and Dr. Harvey West for the assistance during fatigue pre-crack experiments and the use of the optical microscope. We also would like to extend our appreciation to Prof. Zeev Shayer from Colorado School of Mines and Dr. Charles Bryan from Sandia National Laboratory for the discussions about the experiment. This work is supported by NEUP IRP, "Innovative Approach to SCC Inspection and Evaluation of Canister in Dry Storage."

References

1. Oberson G, Dunn D, Mintz T, He X, Pabalan R, Miller L (2013) US NRC-sponsored research on stress corrosion cracking susceptibility of dry storage canister materials in marine environments. In: WM2013 Conference, Phoenix, AZ, February 24–28, 2013, Paper Number 13344
2. National atmospheric deposition program/national trends network. <http://nadp.sws.uiuc.edu>
3. Sjong A, Edelstein L (2008) Marine atmospheric SCC of unsensitized Stainless steel rock climbing protection. *J Fail Anal Prev* 8:410
4. Modes and effects analysis (FMEA) of welded stainless steel canisters for dry cask storage systems. EPRI, Palo Alto, CA: 2013. 3002000815
5. EPRI (2014) Calvert Cliffs stainless steel dry storage canister inspection. EPRI, Palo Alto, CA, p 460
6. EPRI 2014. EPRI flaw growth and flaw tolerance assessment for dry cask storage canisters. Presentation to the NRC, August 5, 2014
7. Bryan C, Enos D (2014) Analysis of dust samples collected from spent nuclear fuel interim storage containers at hope creek, Delaware, and Diablo Canyon, California, SAND2014-16383. Sandia National Laboratories, Albuquerque, NM, p 281
8. <http://www.nei.org/issues-policy/nuclear-waste-management/disposal>. Last Accessed on 22 Sept 2016
9. Alyousif OM, Nishimura R (2007) The stress corrosion cracking behavior of austenitic stainless steels in boiling magnesium chloride solution. *Corrosion Sci* 49:3040–3051. Elsevier
10. Raman RS, Pal S (2011) A simple approach to the determination of threshold stress intensity for stress corrosion cracking (K_{ISCC}) and crack growth of sensitized austenitic stainless steel. *Metallurg Mater Trans A* 42A
11. Speidel MO (1981) Stress corrosion cracking of stainless steels in NaCl solutions. *Metallurg Trans A* 12A
12. Khatak HS, Gnanamoorthy JB, Rodriguez P (1996) Studies on the influence of metallurgical variables on the stress corrosion behavior of AISI 304 stainless steel in sodium chloride solution using the fracture mechanics approach. *Metallurg Mater Trans A* 27A
13. North American stainless, "Metallurgical Test Report," Certificate 995147 01
14. ASTM International, "Standard Test Method for Linear-Elastic Plane-Strain Fracture Toughness K_{IC} of Metallic Materials," E399-12
15. ASTM International, "Standard Test Method for Measurement of Fracture Toughness," E1820-15

16. ASTM International, "Standard Test Method for Determining Threshold Stress Intensity Factor for Environment-Assisted Cracking of Metallic Materials," E1681-03
17. Lake Products Company LLC, "Sea Salt," ASTM D1141-52 Formula a, Table 1, Sec. 4
18. Bryan C Summary of available data for estimating chloride-induced SCC crack growth rates for 304/316 stainless steel," Sand 2016-2922R. Sandia National Laboratories

Appendix C

Understanding stress corrosion cracking behavior of austenitic stainless steel SS304 for dry storage canisters in simulated sea-water

Understanding stress corrosion cracking behavior of austenitic stainless steel SS304 for dry storage canisters in simulated sea-water

Leonardi Tjayadi¹, Nilesh Kumar² and Korukonda L Murty³

Abstract

A number of recent studies have suggested that dry storage canisters (DSCs) made of austenitic stainless steel SS304 to store spent nuclear fuel located along coastal region may undergo stress corrosion cracking (SCC) if their useful life is extended due to lack of a permanent underground burial repository. It, therefore, becomes necessary to understand SCC behavior of SS304 in marine environment. We report here our results on SCC of SS304H in simulated sea-water using fracture mechanics approach as a function of temperature. The average crack growth rates were noted to be $0.975 \times 10^{-10} \pm 9.528 \times 10^{-12}$, $3.258 \times 10^{-10} \pm 9.551 \times 10^{-11}$ and $1.580 \times 10^{-9} \pm 2.593 \times 10^{-10}$ m/s at 22, 37, and 60 °C, respectively. The activation energy of the crack-growth process was estimated to be 60.9 kJ/mol corresponding to diffusion of hydrogen in steel. Optical microscopy revealed intergranular nature of the crack-growth.

Keywords: Crack growth, Fatigue pre-cracking, Fracture mechanics, Hydrogen embrittlement, Intergranular cracking, Potential drop, SCC, Stainless steel

1. Introduction

After being removed from the reactor, the spent nuclear fuels (SNF) in the U.S. are stored in spent fuel pools at reactor facilities for more than five years before transporting to dry storage facilities at Independent Spent Fuel Storage Installations (ISFSI) for storage for more several decades. SNFs are placed in dry canisters at ISFSI that are usually made of austenitic stainless steel (SS) types 304 and 316 contained in a larger concrete case equipped with air ventilation for natural cooling. The air ventilation on the concrete case provides a path for the dry canister to be exposed to the ambient site conditions of the spent fuel storage facilities typically located close to the ocean [1]. The atmospheric seacoast conditions in the U.S. contain high concentration of chloride salts that get deposited on the dry storage canisters through the air ventilation on the concrete resulting in chloride-induced stress corrosion cracking (CISCC) [2-3].

An investigation was conducted by Electric Power Research Institute (EPRI) on the material degradation mode in ISFSI and listed CISCC as a potential degradation mode for the dry canisters [4]. CISCC presents a big issue in stainless steel dry canisters considering the vicinity of the ISFSI to the ocean in the US. EPRI and Sandia National Laboratories performed canister inspections and found chloride salts on the surface of the canister at the ISFSI nearby marine environments [5-7]. With the uncertainty of the Yucca Mountain Nuclear Waste Repository [8] and nuclear waste reprocessing facility projects for non-proliferation issues, the dry storage facilities at ISFSI has to be given much attention.

Determining the average crack growth rate in a corrosive environment can prove beneficial in investigating SCC of dry canister and help assessing its structural lifetime. SCC studies of austenitic stainless steel have been conducted under magnesium chloride (MgCl₂) [9-13] and NaCl [14-16] solutions where it is reported that hydrogen diffusion is responsible for the intergranular cracking of sensitized stainless steels [9-16]. This paper presents crack growth experiments using fracture mechanics with a wedge opening loading (WOL) specimen of sensitized SS304H under substitute ocean water at three different temperatures to investigate the SCC behavior of SS304H.

2. Experimental Procedure

2.1 Material

The sensitized SS304H material (600 °C for 215 hours) was provided by the Colorado School of Mines whose chemical composition is shown in Table 1. Tensile test produces a yield strength of 302 ± 11 MPa, ultimate tensile strength of 701 ± 14 MPa, uniform elongation of $80.8 \pm 5.3\%$ and total elongation of $92.4 \pm 4.6\%$.

¹ Doctoral Student, Department of Nuclear Engineering, NC State University, Raleigh, NC, USA (ltjayad@ncsu.edu)

² Assistant Professor, Metallurgical and Materials Engineering, University of Alabama, Tuscaloosa, AL, USA (nkumar@eng.ua.edu)

³ Progress Energy Distinguished Professor of Nuclear Engineering, NC State University, Raleigh, NC, USA (murty@ncsu.edu)

Table 1. Chemical composition (wt.%) of SS304H [17].

C	Co	Cr	Cu	Mn	Mo	N	Ni	P	S	Si	Fe
0.0418	0.1345	18.1930	0.4005	1.7495	0.2985	0.0844	8.0725	0.0335	0.0010	0.2930	Bal

2.2 Microstructural Characterization

For the microstructural characterization of as-received material, the sensitized SS304H material was mechanically polished to a mirror finish and etched with a solution made of equivalent volume ratio of hydrochloric acid, nitric acid and water, then cleaned with methanol and deionized water. Scanning electron microscope (SEM) feature of energy dispersive spectroscopy (EDS) was utilized to identify the elemental composition present in the alloy. The specimen was cleaned with acetone post crack growth experiment and observed under micrograph for measurement of crack growth. The specimen was then etched with the same solution to observe the crack morphology.

2.3 Stress Corrosion Cracking

2.3.1 Fatigue Pre-cracking

A fatigue machine from TestResources model 910LX15 was used to fatigue pre-crack the WOL specimens conforming to ASTM standards E399 – 12 [18], E1820 – 15 [19], and E1681 – 03 [20] to generate the desired fatigue pre-crack length. The fatigue pre-cracking was performed under sinusoidal cyclic loading at a load ratio of 0.1 with a maximum force of 6 kN. Before the fatigue pre-crack experiment, one side of the WOL specimen was mechanically polished with final polishing at 50 nm diamond suspension so the fatigue pre-crack length can be clearly observed. Fig. 1a shows the dimensions of the WOL specimen in inches and Fig. 1b displays the WOL specimen.

2.3.2 Crack Growth Measurement Using Direct Current Potential Drop Technique

SCC investigation using fracture mechanics approach consists of monitoring of load and crack length with time. The direct-current potential drop (DCPD) technique because of its simplicity has been extensively used for monitoring crack growth among scanning electron microscopy, optical microscopy, replication and ultrasonic. In the DCPD technique, a constant current is continuously supplied to the specimen and the potential drop is measured as crack grows. The fatigue pre-cracking was stopped once the desired fatigue pre-crack length was generated and the fatigue pre-crack length was then measured using an optical microscope. The potential drop for the corresponding fatigue pre-crack length was measured using the DCPD technique that consists of a direct current supply unit (Kikusui PAT160-50T) and a nanovoltmeter (Keithley 2182A). Another fatigue pre-crack experiment was performed again to produce a new fatigue pre-crack length and its potential drop was measured again. This procedure was repeated numerous times to acquire a number of data points for the calibration curve of potential drop as a function of crack length as can be seen in Fig. 2.

Crack growth experiments were performed at three different temperatures of 22, 37 and 60 °C by submerging the WOL specimen in the substitute ocean water whose composition is given in Table 2 where the fatigue pre-crack length (Fig. 3) is submerged in the solution and the notch stays above the solution. Initial stress intensity factors of 34.1, 31.4 and 30.3 MPa.m^{1/2} were applied at the beginning of the experiments through an instrumented bolt to the specimens fatigue pre-cracked to 897, 860 and 735 μm for 22, 37 and 60 °C, respectively.

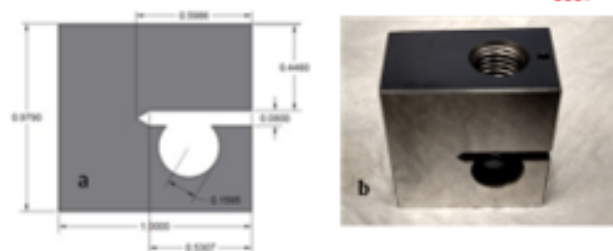


Figure 1a. Dimensions of WOL specimen in inches and **b.** An image of a WOL specimen.

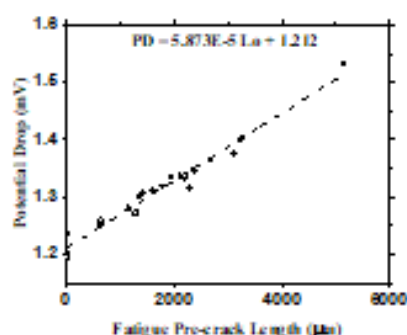


Figure 2. Calibration chart of potential drop as a function of fatigue pre-crack length.

Table 2. Chemical composition of the substitute ocean water in g/L [21].

NaCl	MgCl ₂	Na ₂ SO ₄	CaCl ₂	KCl	NaHCO ₃	KBr	H ₃ BO ₃	SrCl ₂	NaF
24.53	5.20	4.09	1.16	0.695	0.201	0.101	0.027	0.025	0.003

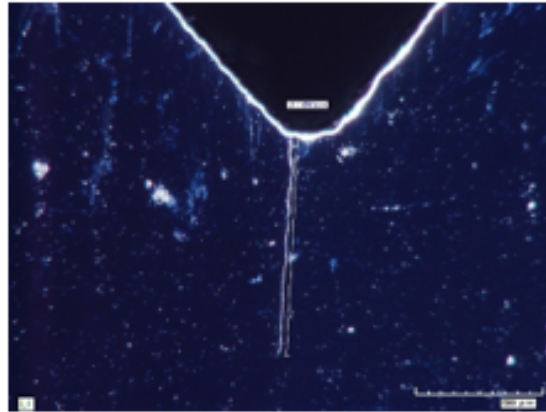


Figure 3. Fatigue pre-cracked sensitized SS304H WOL specimen.

3. Results and Discussion

3.1 Microstructural Characterization of As-Received Material

The microstructure of the as-received material is displayed in Fig. 3a and the elements present in the sensitized SS304H material are shown in Fig. 3b using energy dispersive spectroscopy (EDS).

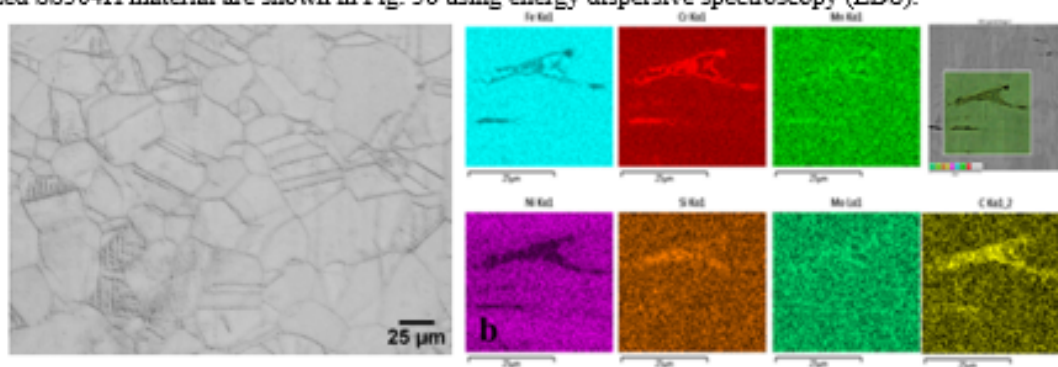


Figure 4a. Micrograph and b. Elements identified using the EDS of sensitized SS304H.

3.2 Crack Growth during Stress Corrosion Cracking

The plot of stress intensity factor with time in Fig. 5a indicates that the applied load decreases slowly due to load relaxation and thus, the crack did not propagate for the first 310 hrs of the experiment. The steep decrease in stress intensity factor with time afterwards suggests that crack propagation occurred. Data analyses yielded an average crack growth rate of SS304H at 22 °C under substitute ocean water of $0.975 \times 10^{-10} \pm 9.528 \times 10^{-12}$ m/s which is in good agreement with the average crack growth rate for SS304 at 22 °C as reported by Speidel of 1.438×10^{-10} m/s [22].

Another experiment was conducted with a sensitized SS304H specimen fatigue pre-cracked to 860 μm and with an initial stress intensity factor of $31.4 \text{ MPa m}^{1/2}$ submerged in substitute ocean water at 37 °C. As the experiment was conducted at higher temperature, the crack propagation occurred earlier than the previous one at 22 °C. From the stress intensity factor behavior with time in Fig. 6a, crack is noted to propagate after 75 hrs of the experiment. Data analyses from Fig. 6b for SS304H experiment at 37 °C under substitute ocean water produces an average crack growth rate of $3.258 \times 10^{-10} \pm 9.551 \times 10^{-11}$ m/s.

Another sensitized SS304H specimen was fatigue pre-cracked to 735 μm and submerged in substitute ocean water with a starting applied load of $30.3 \text{ MPa m}^{1/2}$ at 60 °C. The plot of stress intensity factor with time in Fig. 7a indicates that the crack propagates after six hours of the experiment following a steep decrease in the applied load. In addition, crack growth rate behavior with stress intensity factor in Fig. 7b produces an average crack growth rate of SS304H at 60 °C under substitute ocean water of $1.580 \times 10^{-9} \pm 2.593 \times 10^{-10}$ m/s. The average crack growth rates for the three different temperatures are summarized in Table 3.

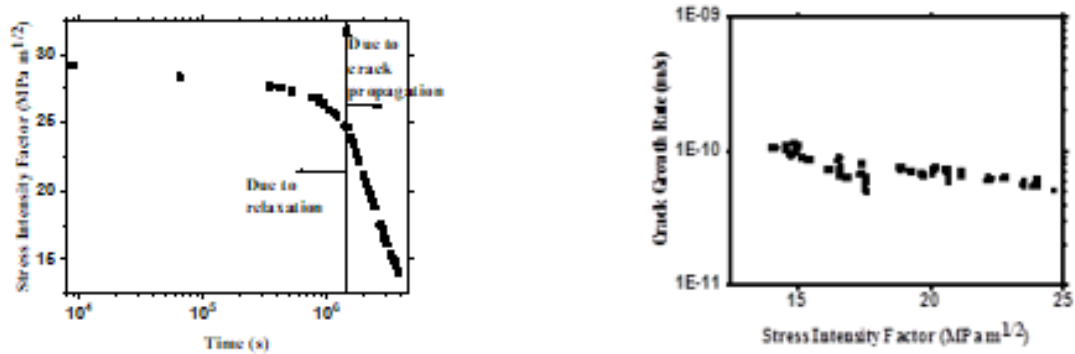


Figure 5 a. Stress intensity factor behavior with time and b crack growth rate as a function of stress intensity factor for sensitized SS304H under substitute ocean water at 22 °C.

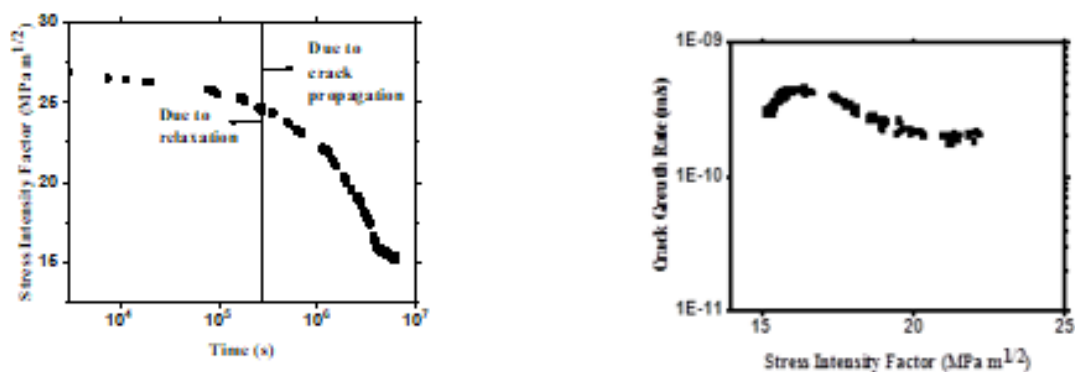


Figure 6 a. Stress intensity factor behavior with time and b crack growth rate as a function of stress intensity factor for sensitized SS304H under substitute ocean water at 37 °C.

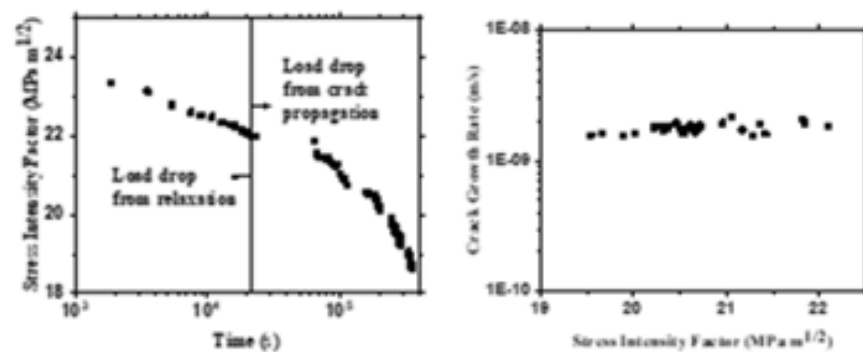


Figure 7 a. Stress intensity factor behavior with time and b crack growth rate as a function of stress intensity factor for sensitized SS304H under substitute ocean water at 60 °C.

Table 3. Average crack growth rates of sensitized SS304H under substitute ocean water at 22, 37 and 60 °C.

Temperature (°C)	Average da/dt (m/s)	Average da/dt (mm/year)
22.0 ± 0.6	$0.975 \times 10^{-10} \pm 9.528 \times 10^{-12}$	3.07 ± 0.30
37.2 ± 0.9	$3.258 \times 10^{-10} \pm 9.551 \times 10^{-11}$	10.27 ± 3.01
60.3 ± 0.5	$1.580 \times 10^{-9} \pm 2.593 \times 10^{-10}$	49.83 ± 8.18

Following Arrhenius dependency on the average crack growth rates as a function of inverse of temperature, a slope indicating an activation energy of 60.9 kJ/mol is obtained which is in agreement with the range suggested by Khatak et al of 50-65 kJ/mol [15] which indicates that hydrogen diffusion in steels is responsible for the corrosion reaction [23].

3.3 Microstructural Characterization after the SCC Experiment

After the crack growth experiments, the WOL specimens were etched and observed under optical microscopy to observe the nature of crack propagation as shown in Figs. 8a, b and c for 22, 37 and 60 °C, respectively where all specimens exhibit intergranular crack propagation due to chromium depletion at the grain boundary. Crack growth measurements from the micrograph produced values of 413, 1915 and 642 μm as compared to the crack growth values from DCPD technique of 405, 1840 and 615 μm for 22, 37 and 60 °C, respectively. The crack growth values from the micrograph are in good agreement with those from the DCPD measurement.

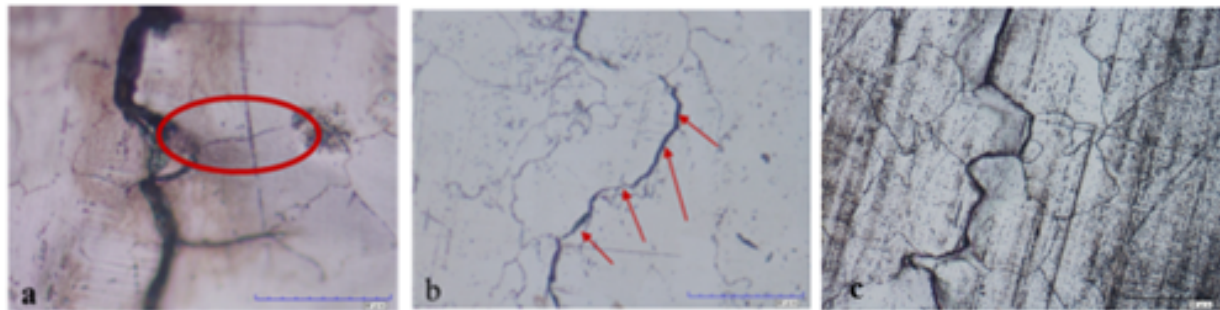


Figure 8. Intergranular crack propagation of the sensitized SS304H specimens after crack growth experiments at a. 22 °C, b. 37 °C and c. 60 °C.

4. Conclusions

Crack growth experiments using fracture mechanics approach were conducted with sensitized SS304H WOL specimens under substitute ocean water to study the SCC behavior of dry storage canisters for spent nuclear fuel. Prior to crack growth experiments, fatigue pre-cracking on a WOL specimen was conducted several times to different lengths and their corresponding potential drop values were measured using a DCPD technique to generate a calibration chart. Crack growth experiments under substitute ocean water at 22, 37 and 60 °C produce average crack growth rates of $0.975 \times 10^{-10} \pm 9.528 \times 10^{-12}$, $3.258 \times 10^{-10} \pm 9.551 \times 10^{-11}$ and $1.580 \times 10^{-9} \pm 2.593 \times 10^{-10}$ m/s, respectively giving an activation energy of 60.9 kJ/mol suggesting hydrogen diffusion in steels. Optical microscopy confirmed the crack growth values from the DCPD technique and exhibited intergranular crack propagation on the sensitized specimens.

Acknowledgements

Special thanks are given to Dr. Scott Gordon from Colorado School of Mines for providing the SS304 plates, Chris Sanford for preparing the WOL specimens, Dr. Harvey West for the fatigue pre-crack experiments and the optical microscopes. We also appreciate the discussions with Prof. Zaeq Shayer from Colorado School of Mines and Dr. Charles Bryan from Sandia National Laboratory about the experiment. This work is supported by NEUP IRP, "Innovative Approach to SCC Inspection and Evaluation of Canister in Dry Storage."

References

1. G. Oberston, D. Dunn, T. Mintz, X. He, R. Babalan and L. Miller, "US NRC-Sponsored Research on Stress Corrosion Cracking Susceptibility of Dry Storage Canister Materials in Marine Environments," *WM2013 Conference*, Phoenix, AZ, February 24-28, 2013, Paper Number 13344 (2013).
2. National Atmospheric Deposition Program/National Trends Network. <http://nadp.sws.uiuc.edu>
3. A. Sjog, and L. Edelstein, "Marine Atmospheric SCC of Unsensitized Stainless Steel Rock Climbing Protection," *Journal of Failure Analysis and Prevention*, **8**, 410 (2008).
4. Modes and Effects Analysis (FMEA) of Welded Stainless Steel Canisters for Dry Cask Storage Systems. EPRI, Palo Alto, CA: 2013. 3002000815.
5. EPRI 2014. Calvert Cliffs Stainless Steel Dry Storage Canister Inspection. EPRI, Palo Alto, CA. 460.
6. EPRI 2014. EPRI Flaw Growth and Flaw Tolerance Assessment for Dry Cask Storage Canisters, Presentation to the NRC August 5, 2014.
7. C. Bryan and D. Enos, 2014. Analysis of Dust Samples Collected from Spent Nuclear Fuel Interim Storage Containers at Hope Creek, Delaware, and Diablo Canyon, California, SAND2014-16383, Sandia National Laboratories, Albuquerque, NM. 281 p.
8. <http://www.nei.org/issues-policy/nuclear-waste-management/disposal>; last accessed on 09/22/2016.
9. O.M. Alyousif and R. Nishimura, "The Stress Corrosion Cracking Behavior of Austenitic Stainless Steels in Boiling Magnesium Chloride Solution," *Corrosion Science* **49**. 3040-3051. Elsevier (2007).
10. R.K.S. Raman and S. Pal, "A Simple Approach to the Determination of Threshold Stress Intensity for Stress Corrosion Cracking (K_{ISCC}) and Crack Growth of Sensitized Austenitic Stainless Steel," *Metallurgical and Materials Trans. A*. Vol. 42A. (2011).
11. A. J. Russell and D. Tromans, "A Fracture Mechanics Study of Stress Corrosion Cracking of Type-316 Austenitic Steel," *Metallurgical Trans.* **10A**, 1229 (1979).
12. H. Hawkes, F. Beck and M. Fontana, "Effect of Applied Stress and Cold Work On Stress Corrosion Cracking of Austenitic Stainless Steel by Boiling 42 Percent Magnesium Chloride," *Corrosion* **19**. 247 (1963).
13. T. Nakayama and M. Takano, "Application of A Slip Dissolution-Repassivation Model for Stress Corrosion Cracking of AISI 304 Stainless Steel in Boiling 42% MgCl₂ Solution," *Corrosion* **42**, 10 (1986).
14. M.O. Speidel, "Stress Corrosion Cracking of Stainless Steels in NaCl Solutions," *Metallurgical Trans. A*. Vol. 12A. (1981).
15. H.S. Khatak, J.B. Gnanamoorthy, and P. Rodriguez, "Studies on the Influence of Metallurgical Variables on the Stress Corrosion Behavior of AISI 304 Stainless Steel in Sodium Chloride Solution Using the Fracture Mechanics Approach," *Metallurgical and Materials Trans. A*. Vol. 27A. (1996).
16. H. Shaikh, H. Khatak and P. Rodriguez, "Stress Corrosion Crack Growth Behavior of Austenitic Stainless Steels in Hot Concentrated Chloride Solution," *ICF 10* (2001).
17. North American Stainless, "Metallurgical Test Report," Certificate 995147 01.
18. ASTM International, "Standard Test Method for Linear-Elastic Plane-Strain Fracture Toughness K_{IC} of Metallic Materials," E399-12.
19. ASTM International, "Standard Test Method for Measurement of Fracture Toughness," E1820-15.
20. ASTM International, "Standard Test Method for Determining Threshold Stress Intensity Factor for Environment-Assisted Cracking of Metallic Materials," E1681-03.
21. Lake Products Company LLC, "Sea Salt," ASTM D1141-52 Formula a, Table 1, Sec. 4.
22. C. Bryan, "Summary of Available Data for Estimating Chloride-Induced SCC Crack Growth Rates for 304/316 Stainless Steel," Sand 2016-2922R. Sandia National Laboratories.
23. M. R. Louthan, Jr. and R. G. Derrick, *Corros. Sci.* **15**, 565 (1975).